Optimisation and Parametric Study of Heat Transfer in Transpired Solar Collectors Using Computational Fluid Dynamics

---

Seyyed Sadjad Tajdaran

The thesis is submitted in partial fulfilment of the requirements for the award of

Doctor of Philosophy

School of Architecture
Faculty of Technology, Design and Environment
Oxford Brookes University

Oxford
September 2018

To my grandmothers

Madarjoon and Amme Goli

Acknowledgements

I would like to express my special gratitude and appreciation to my Director of Studies, Professor Ray Ogden for he was the best mentor I have had in my entire life. He was a spectacular guide, support, inspiration, and friend to me during my life in Oxford. I am greatly proud for the opportunity I had to be under his supervision.

I also thank my second and third supervisors Dr. Fabrizio Bonatesta and Chirstopher Kendrick (current director of study) for their generous support, technical guidance, and absolute patience in advising me on all aspects of this study.

I am thankful to my dear friends and colleagues at the Architectural Engineering Group for their continuous support and their wonderful companionship: Dimitrios Moutaftis, Bousmaha Baiche, Helen Tanner, Martin Heywood, Martin Dolan, Amy Groeneveld, Mauricio Aguilar, Ray Salter and Nick Whitehouse.

I would like to thank Dr. Shahaboddin Resalati and Shahrzad Amouzad, from the bottom of my heart. They have been supporting me from the first moment I started this adventure in Oxford. I will never forget your generous help and kindness.

Last and most, I am deeply thankful and grateful to my family; my parents, Mehdi and Roza, my sister, Nona, my brother Mohammad, my brother in law, Mostafa and my sister in law, Bahar. I would also like to express my gratitude to my parents-in-law Ali and Roghie.

My heartfelt thanks go to the love of my life, Mehrasa, for her patience and endless support during all the evenings, weekends, and holidays that I spent working on this research and she spent listening to my grumbles of hard times. You are the ground to my adventurous life.

Keywords

Renewable Energy Resources, Transpired Solar Collectors, Building envelope, Cladding, Sustainability, Heat Transfer, Thermal Performance, Heat Exchange Effectiveness, Computational Fluid Dynamics (CFD), Parametric study, Optimisation, Design of Experiments.

Abstract

Transpired Solar Collectors (TSCs) are building-integrated air-heating systems that are able to fully or partially meet the heating demands of buildings. They convert solar radiation into warm air that can either be used for ventilation, or to heat thermal storage media. TSCs are becoming an increasingly viable alternative to conventional fossil fuel-based heating systems or, more commonly, can be used in a way that is complementary to these systems such that reliance on fossil fuels is reduced. As a consequence TSCs have a potentially important role in meeting future carbon reduction goals.

This research has produced a comprehensive numerical model for TSCs based on Computational Fluid Dynamics (CFD) analyses. The model allows parametric studies of key variables and is differentiated from previous models in that it takes full account of factors such as: wind speed and direction, non-uniform flow, turbulent flow, solar radiation intensity, sun position and flow suction rates. It comprises a full size section of cassette-panel TSC that can be easily morphed to reflect a wide range of geometries. A multi-block meshing approach has been employed to reduce grid size and to also resolve jet flows and boundary layers taking place in the plenum and around the absorber plate. Accuracy of the CFD model has been validated against experimental data.

An optimisation study has been carried out based on the CFD model to derive the optimal design of the absorber plate. The study has benefited from Design of Experiments (DoE) which is an efficient and non-biased strategy for such analysis.

Modeling demonstrated that factors such as wind angle have unexpectedly significant adverse effects on system thermal performance. The studies also furthered understanding of key performance attributes including the effects of suction ratio in terms of optimising performance, and the relationship between sun angle and system operating temperature (important for effective operation of heat storage systems). The optimisation analysis of the absorber plate geometry showed that an optimal combination perforations diameter and pitch together with plate thickness can increase the performance of current TSCs up to 48%. Consideration of these factors is essential if the future performance of TSCs is to be optimised and the technology developed to its fullest potential.

This study has provided a basis for optimising the performance of TSCs, developing commercial products, and designing systems based on commercial products in relation to local conditions.

Publications

Parts of this thesis have been published by the author in the papers listed below.

International Refereed Journal Papers

Tajdaran, S., Bonatesta, F., Ogden, R. and Kendrick, C. (2016). CFD modelling of transpired solar collectors and characterisation of multi-scale airflow and heat transfer mechanisms. Solar Energy, 131, pp.149-164.

International Refereed Conference Papers

Tajdaran, S., Bonatesta, F., Ogden, R., Kendrick, C. (2015). Use of CFD modelling for transpired solar collectors and associated characterization of multi-scale airflow and heat transfer mechanisms. In: 6th International Building Physics Conference, Turin, June, Energy Procedia, 78, pp. 2238-2243.

Table of Contents

Optimisation and Parametric Study of Heat Transfer in Transpired Solar Collectors Using Computational Fluid Dynamics 1
Acknowledgements i
Keywords iii
Abstract v
Publications vii
Table of Contents ix
List of Figures xi
List of Tables xv
List of Symbols xvii
Chapter 1 Introduction 1
1.1 Background 1
1.2 Research aim and objectives 4
1.3 Thesis Outline 5
Chapter 2 Literature Review 7
2.1 Introduction 7
2.2 Boundary Layer and Starting Length 7
2.3 Heat Transfer Theory 10
2.4 Heat Exchange Effectiveness and Temperature Rise 13
2.5 Thermal Efficiency 20
2.6 Numerical Modelling Approaches 25
2.7 Airflow around buildings 29
2.8 Turbulence Modelling 30
2.9 Gap in the Knowledge 31
2.10 Concluding Remarks 33
Chapter 3 Research Methodology 34
3.1 Introduction 34
3.2 Problem Definition 34
3.3 Brief Description of the Experimental Work 41
3.4 Grid Design 45
3.5 Numerical Approach 48
3.6 General Model Setup and Boundary Conditions 50
3.6.1 Ambient region 54
3.6.2 Absorber plate region 55
3.6.3 Plenum region 56
3.6.4 Perforations region 56

3.7 Grid Independence Test 57
3.8 Numerical Errors 58
3.9 Model Validation 58
3.10 Absorber Plate Geometry Optimisation 62
3.10.1 Sampling 64
3.10.2 Data analysis 66
3.10.3 Quality of curve fitting 68
3.10.4 Optimisation and validation 69
3.11 Concluding remarks 70
Chapter 4 System sensitivity to geometric and climatic variables 74
4.1 Introduction 74
4.2 Assessment of the general characteristics of airflow and thermal field 74
4.3 Effects of Wind Angle 79
4.4 Effects of Wind Speed 87
4.5 Effect of Solar Radiation 98
4.6 Effect of 'Time of The Day' 99
4.7 Effect of Plenum Depth 102
4.8 Effect of Absorber Plate's Thermal Conductivity 107
4.9 Statistical Analysis and Optimisation 111
4.9.1 Validation 119
Chapter 5 Conclusion and recommendations for further research 124
5.1 Conclusions 124
5.2 Recommendations for Future Study 126
5.2.1 Edge effect evaluation together with 3-D wind flow 127
5.2.2 Optimisation incorporated with climatic and thermal variables 127
5.2.3 Heat transfer enhancement based on the main heat exchanging zones 127
5.2.4 Contribution of each material to the final heat transfer 127
5.2.5 An unsteady state study of temperature built up 128
5.2.6 Enhanced TSCs 128
References 129

List of Figures

Figure 1-1. Schematic diagram of the thermal field in TSCs. 3
Figure 2-1. Velocity and thermal boundary layers for laminar forced convection over a flat plate. 8
Figure 2-2. Velocity and thermal boundary layers of laminar flow over a perforated flat plate with suction. 8
Figure 2-3. Schematic diagram of parameters considered in Gunnewiek et al. (1996). 12
Figure 2-4. Sketch of geometry parameters used in Li et al. (2014) 20
Figure 2-5. Schematic diagram of geometric configuration of the absorber studied in Dymond and Kutscher (1997). 22
Figure 2-6. Schematic diagram of CFD model domain and streamlines - Kutscher's (1992) study. 26
Figure 2-7. Schematic airflow distribution on the façade of building for (a) wind direction of β=45o and (b) normal wind direction β=90o showed in Mu et al., (2016) 29
Figure 2-8. Schematic shape of fluctuation, reverse and parallel flow around a tall building for normal and oblique wind directions (ASHRAE Handbook, 2015, Section 45.3) 30
Figure 3-1.(a) Building façade with the installed cassette-panels (the four panels directly between the windows shown by arrows), (b) Conceptual illustration of a Cassette Panel-TSC solar air-heating system (Hall et al., 2014). 37
Figure 3-2. Schematic thermal and airflow fields in TSCs. 38
Figure 3-3. Flowchart of the steps taken to develop the CFD model. 40
Figure 3-4. Position of the solar pycnometer recording solar radiation intensity. 41
Figure 3-5. Mass flow meter device at the outlet of the TSC system 41
Figure 3-6. Location of the weather station and the sensors across the system. 42
Figure 3-7. The cassette panel: a) whole panel; b) close up of perforations. 43
Figure 3-8. CAD drawing of a) the trialled double cassette panel b) the modelled portion of the cassette panel. 44
Figure 3-9. Section of the modelled TSC in STAR-CCM+. 44
Figure 3-10. Mesh arrangement in 2D. 45
Figure 3-11. Body-fitted mesh around a circular perforation; current study. 46
Figure 3-12. A cut through view of the full domain grid design. 48
Figure 3-13. Hexahedral Mesh created around the plate and in the free-stream region; b) Details of the conical grid scheme to capture the jet flow 48
Figure 3-14. Solar model coordinate system (STAR-CCM+ 9.04. 2014) 49
Figure 3-15. Computational domain and model configuration; (a) Top view, (b) Side view, (c) Sketch of the absorber plate. 53
Figure 3-16. Grid independency tests presented in terms of a) surface temperature and b) outlet temperature. 57
Figure 3-17. Comparison between the CFD results and the experimental data for the ratio of absorber plate temperature and plenum outlet temperature ($Ts/Tout$). 60
Figure 3-18. Comparison between the CFD results and the experimental data for Heat Exchanger Effectiveness (HEE). 60
Figure 3-19. Comparison between the HEE values predicted by the current CFD model and the correlations by Kutscher (1992) and Van Decker et al. (2001) regarding the Experimental tests by Hall et al. (2014) 61
Figure 3-20. Flowchart of statistical analysis and optimisation study. 64
Figure 3-21. An example 2-D snap of space filling design excluding the extreme points. 65
Figure 3-22. A 3-D view of design of experiment excluding the eight extreme points along the boundaries. 66

Figure 3-23. An overview of the regression model generation. 67
Figure 3-24. An example of model setup in MBC interface. 67
Figure 3-25. A screenshot of the optimiser panel showing the initial conditions setup. 70
Figure 4-1.(a) Velocity streamlines of ambient/external airflow together with jet stream inside the plenum (view from above); (b) Airflow within the plenum (side view). 75
Figure. 4-2. Front-view cross section of pressure distribution on centre-line of plenum, Section (1): upper part of plenum, Section (2): lower part of plenum. 76
Figure. 4-3. Side-view cross section of plenum showing velocity distribution, Section (1) upper part of plenum, Section (2) lower part of plenum. 77
Figure 4-4. Front view of: (a) Temperature distribution over the perforated plate, (b) Heat exchange effectiveness distribution over the perforated plate, Section (1) the upper part of the plate, Section (2) the lower part of the plate. 78
Figure 4-5. Side-view cross section of plenum showing, (a) temperature and (b) velocity distributions in upper part of plenum together with stremlines. 78
Figure 4-6. The distribution of wind power by direction recorded at the trial site between 22nd December 2011 to 4th January 2012. 81
Figure. 4-7. Schematic of wind flow with different angles relative to the absorber plate. 81
Figure. 4-8. Impact of wind angle on temperature rise and absorber surface temperature for (a) $VsU\infty = 0.004$, (b) $VsU\infty = 0.006$, (c) $VsU\infty = 0.008$, (d) $VsU\infty = 0.010$, with constant wind speed of $U\infty = 3\ m/s$. 82
Figure 4-9. Impact of wind angle on heat exchange effectiveness performed by (a) the whole system, (b) the front surface, (c) the perforations, and (d) the back surface at different suction ratios. 84
Figure. 4-10. Impact of wind angle on thermal efficiency for the studied suction ratios at constant wind speed of $U\infty = 3\ m/s$. 85
Figure 4-11. Mean values of pressure drop versus the studied wind direction for different suction ratios. 86
Figure 4-12. Pressure drop at the regions of perforations entrance and system outlet due to suction ratio variation from 0.004 to 0.010. 87
Figure. 4-13. Impact of wind speed on temperature rise and absorber surface temperature for: (a) $VsU\infty = 0.004$, (b). $VsU\infty = 0.006$, (c) $VsU\infty = 0.008$, (d) $VsU\infty = 0.010$. 89
Figure 4-14. Impact of wind pseed on pressure drop across the system $(pout - pin)$ and pressure at the entrance of perforations temperature for: (a) $VsU\infty = 0.004$, (b). $VsU\infty = 0.006$, (c) $VsU\infty = 0.008$, (d) $VsU\infty = 0.010$. 90
Figure 4-15. Temperature rise versus pressure drop at different suction ratios 91
Figure 4-16. Pressure drop as a function of suction velocity presented with the recommended values of suction velocity and pressure drop to avoid reverse flow. 93
Figure 4-17. Contribution of each part of the system to the final HEE. 94
Figure 4-18 . Impact of wind speed on heat exchange effectiveness for: $VsU\infty = 0.004$, $VsU\infty = 0.006$, $VsU\infty = 0.008$, and $VsU\infty = 0.010$. 95
Figure. 4-19. HEE drop due to the increasing suction ratio from 0.004 to 0.01 at different wind speeds. .96
Figure. 4-20. Impact of wind speed on thermal efficiency for different suction ratios. 97
Figure. 4-21. Impact of wind speed-averaged suction ratio on thermal efficiency and temperature rise. 98
Figure 4-22. Impact of solar radiation on temperature rise and absorber surface temperature. 98
Figure 4-23.Impact of solar radiation on temperature rise and absorber surface temperature for $\beta = 0°$ 99
Figure 4-24. Impact of day time on temperature rise and absorber surface temperature. 100
Figure 4-25. Deliverable temperature of the TSC predicted for 22nd December based on the modelled temperature rise. 101
Figure 4-26. Impact of day time (sun position) on thermal efficiency and HEE 102
Figure 4-27. Impact of plenum depth on temperature rise and absorber surface temperature for a) $U\infty = 3\ m/s$, b) $U\infty = 5\ m/s$, c) $U\infty = 7\ m/s$. 103

Figure ‍4-28. Pressure drop across the system $(pin - pout)$. 104
Figure. ‍4-29. Impact of plenum depth on Heat Exchange Effectiveness (HEE) for $U\infty = 3\ m/s$, $U\infty = 5\ m/s$, and $U\infty = 7\ m/s$. 105
Figure ‍4-30. Impact of plenum depth on Heat Exchange Effectiveness contributed by front, perforations and back of the plate region against the wind speed of (a) 3 m/s and (b) 7 m/s. 106
Figure. ‍4-31. Impact of plenum depth on the thermal efficiency for: a) $U\infty = 3\ m/s$, b) $U\infty = 5\ m/s$, c) $U\infty = 7\ m/s$. 107
Figure. ‍4-32. Impact of thermal conductivity of absorber plate on temperature rise and absorber surface temperature. 109
Figure ‍4-33. Variation of operating temperatures versus relative variation growth of (a) thermal diffusivity and (b) thermal conductivity in the form of natural logarithm. 110
Figure. ‍4-34. Impact of thermal conductivity of absorber plate on heat exchange effectiveness. 111
Figure ‍4-35. Impact of thermal conductivity of absorber plate on heat exchange effectiveness 111
Figure ‍4-36. 3-D view of the DoE. 112
Figure ‍4-37. Distribution of optimised HEE versus individual design parameters for: (a) Quadratic model, (b) Cubic model, (c) Quartic model, for a sample population size of 36. 113
Figure ‍4-38. Distribution of optimised HEE versus individual design parameters: (a) Quadratic model, (b) Cubic model, (c) Quartic model, for a sample population size of 42. 115
Figure ‍4-39. Plots of predicted (regression) against observed (CFD simulated) values for (a) Quadratic model, (b) Cubic model and, (c) Quartic model. 116
Figure ‍4-40. Plots of residuals versus predicted HEE for (a) Quadratic model, (b) Cubic model and, (c) Quartic model – 42 sample size population. 117
Figure ‍4-41. Variation of pressure drop versus plate thickness at D=0.8 mm and P= 7mm. 118
Figure ‍4-42. Effectiveness comparison of the optimised and conventional TSC geometry 121
Figure ‍4-43.Front view of air temperature and pressure distribution taken place within the plenum 122

List of Tables

Table 3-1. Summary of the CFD model setup. 52
Table 3-2 Details of the cases used for validation. 59
Table 3-3. Held-constant factors for geometrical optimisation 63
Table 4-1. Details of the case studied for wind angle and suction ratio effect. 80
Table 4-2. Details of the case studied for Wind speed and Suction ratio effect 88
Table 4-3. Comparison of pressure drop magnitude across the system for the cases with similar suction velocities. 92
Table 4-4. Details of the case studied for plenum depth effect 103
Table 4-5. Details of the case studied for the effect of absorber plate's thermal conductivity 108
Table 4-6. Details of the added points about the projected optimised region. 113
Table 4-7. Details of sample points for further study on the fluctuations. 114
Table 4-8. Optimal solution for geometrical factors returned by different regression models. 114
Table 4-9. Quality indicators of the regression models 115
Table 4-10. Details of the operating conditions for applied to the optimised geometry 120

List of Symbols

A_C	Surface Area of the Collector	m^2
C_p	Specific Heat Capacity	kJ/(kg °C)
D	Perforations Diameter	mm
G	Solar Radiation Intensity	W/m^2
F_{cs}	View Factor between the Sky and the Collector	-
F_{cg}	View Factor between the Ground and the Collector	-
k	Thermal Conductivity	W/mK
L_s	Starting Length	m
L_e	Convective Heat Loss Length	m
p	Pressure	Pa
P	Pitch Distance	mm
Pr	Prandtl Number	-
Q	Heat Flux	W/m^2
Re_b	Reynolds Number based on Hole Velocity and Pitch	-
Re_h	Reynolds Number based on Hole Velocity and Diameter	-
Re_s	Reynolds Number based on Suction Velocity and Pitch	-
Re_w	Reynolds Number based on Wind Speed and Pitch	-
t	Absorber Plate Thickness	mm
T	Temperature	°C
T_{amb}	Ambient Air Temperature	°C
T_{gnd}	Ground Temperature	°C
T_{out}	Outlet Temperature	°C
T_s	Absorber Surface Temperature	°C
T_{sky}	Sky Temperature	°C
u	Flow Velocity	m/s
U	Heat Transfer Coefficient	W/m^2K
U_∞	Free stream (wind) Speed	m/s

V_h	Hole Velocity	m/s
V_s	Suction Velocity	m/s
Greek Letters		
α	Thermal Diffusivity	m^2/s
β	Radiative Absorptivity	-
ϵ	Radiative Emissivity	-
τ	Radiative Transmissivity	-
ε	Heat Exchange Effectiveness	-
ν	Kinematic Viscosity	m^2/s
η	Thermal efficiency	-
φ	Arbitrary Scalar Quantity	-
σ	Porosity	-
ρ	Density	kg/m^3
Abbreviations		
CFD	Computation Fluid Dynamics	-
NTU	Number of Transfer Units	-
PISO	Pressure Implicit with Splitting of Operator	-
QUICK	Quadratic Upstream Interpolation for Convective Kinematics	-
SIMPLE	Semi-Implicit Method for Pressure Linked Equations	-
TSC	Transpired Solar Collector	-
Subscripts		
$\mathrm{abs-amb}$	Between Absorber and Ambient	-
$\mathrm{abs-bp}$	Between Absorber and Back Plate	-
$\mathrm{air-abs}$	Between Air and Absorber	-
$\mathrm{air-bs}$	Between Air and Back Surface	-
cond	Conduction	-
conv	Convection	-
out	Outlet	-
rad	Radiation	-

Chapter 1 Introduction

1.1 Background

In line with 2050 EU carbon reduction roadmaps, the UK is committed to reduce greenhouse gas emissions by 80% in comparison to 1990 levels (The Stationary Office, 2008). Buildings are responsible for 40% of energy consumption and 37% of greenhouse gas emissions. A large proportion of energy used in buildings is associated with heating (Committee on Climate Change, 2014). As conventional hydrocarbons (oil and gas) are the main energy sources for heating in buildings, reducing reliance on these energy sources has a key role to play in achieving this target. There are viable alternatives for the conventional energy based heating systems amongst which Transpired Solar Collectors (TSCs) are feasible means of heating/preheating large air volumes in buildings. Transpired Solar Collectors are simple façade-integrated solar air-heating systems that can collect heat resulting from solar radiation. TSCs however were originally developed for crop-drying in Northern America. An opportunity exists to optimise and enhance the thermal efficiency of these almost maintenance-free systems in order to be used in both residential and office buildings. The aim of the research is to develop an accurate numerical model of the complex fluid flows and heat transfer mechanisms in TSCs and to use this model to improve critical aspects of the systems' performance and efficiency. The model will rely on Computational Fluid Dynamics (CFD) based approaches.

Greenhouse gases are mostly the product of human activities and have been increased due to modernised and industrialised lifestyle. Whilst it seems difficult to ask people to change their lifestyle and save energy in the favour of decreasing our carbon emission footprint, what we are capable of doing is to replicate conventional sources of energy with renewable sources to approach a more sustainable way of living on the earth.

Along with the international programme towards development of renewable energy generation, the UK is planning to reach Renewable Energy Directive (RED) target which aims for 15% of energy consumption to be from renewables in 2020. Whilst the estimated trajectory of energy from renewables is 9.2% in 2016, the provisional final energy consumption in 2017 is calculated to be 10.2% (DECC, 2018). The latest statistics show that the share of renewables of electricity generation in 2018 increased from

27% in 2015 to 30.1% in the same period in 2017 which demonstrate the urge and investment being made towards replacing conventional fossil fuels with renewables (DECC, 2018).

Technologies have been developed targeting alternatives for conventional heating systems using renewables amongst which Transpired Solar Collectors are feasible means of heating/preheating large air volumes in buildings. Transpired Solar Collectors are simple façade-integrated solar air-heating systems that can collect heat resulting from solar radiation.

Relatively little consideration has thus far been extended to Transpired Solar Collectors (TSCs) which are potentially highly cost effective solutions in relation to heat demand (Arulanandam et al, 2000; Li et al, 2014).

TSCs are a viable means of heating large air volumes which can be used to heat buildings. These systems were originally developed in Canada for summer crop-drying, but as a consequence of design optimisation can now be used to supplement building space heating in temperate climates by providing useful amounts of warm air in the Autumn and Spring (Hollick, 1994). TSCs are typically able to deliver air 10-15°C warmer than ambient external temperature (Hall et al. 2014). This warm air can either be ducted directly into buildings or be used as preheat for 'Heating, Ventilation and Air Conditioning' (HVAC) systems (Athienitis et al., 2011).

TSCs are wall-mounted air heating systems comprising a perforated steel sheet installed on a building façade that acts as a solar absorber (Figure 1-1). The perforated plate absorbs solar radiation from the sun and heats air local to its surfaces that passes through the perforations. A fan sucks air through the perforations into a cavity behind the absorber plate (referred as plenum), and in simple arrangements delivers the warmer air into the interior of the building where there is heating demand. Heat transfer takes place continuously as the air travels through the absorber plate and into the plenum, being concentrated mostly at the air-steel interface and at the perforations. The heated air is used to wholly or partially satisfy ventilation requirements.

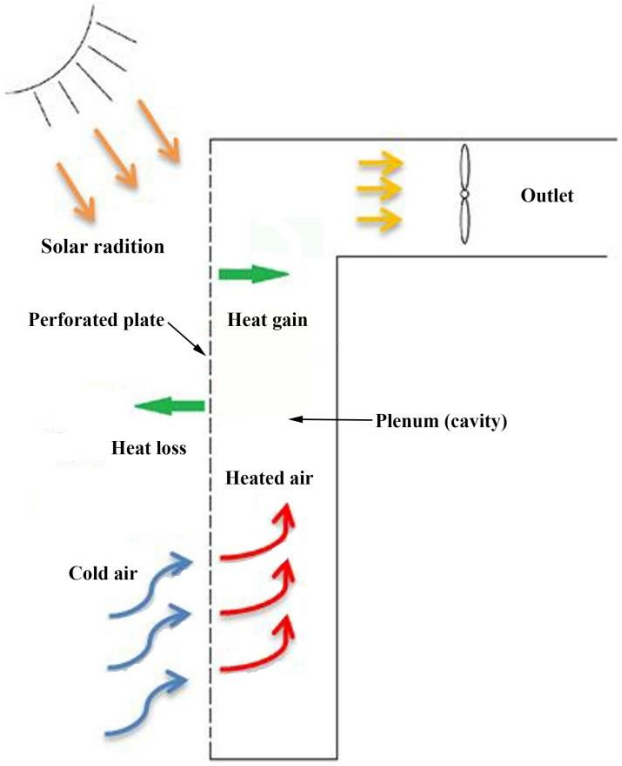

Figure 1-1. Schematic diagram of the thermal field in TSCs.

Whilst these systems are deemed to be relatively cheap, maintenance- free, and able to provide significant amount of heat in the regions with relatively high amount of solar insolation, their lack of efficiency is noticeable in the countries which do not get enough solar energy exposure specially in winter. Although TSCs show an acceptable performance in the industrial section, the combination of infrequent clear sky and cold weather in winters necessitates these systems to be optimised for commercial and residential buildings (Brown et al., 2014). To encourage the use of these novel systems as part of the sustainable energy generation, it is beneficial to optimise and enhance the thermal performance of the systems in order to harness solar radiation to either store or instantly use the captured heat as a main heating resource in buildings. Improved thermal performance may also lead to:

- Flexibility in ventilation rate: More efficient systems able to deliver air at higher temperatures would reduce mass flow rates and avoid over-ventilation, i.e. would provide more heat from less airflow.
- Reduction in physical size of TSC installations (absorber plates): Systems become easier to accommodate on smaller facades.
- Extending the operating period of TSCs: Enhanced thermal efficiency allows systems to operate for an increased number of hours per day and further into winter months.

- Increasing the number of days of TSCs practicality under different climatic conditions.

To do so, it is essential to understand the underlying physics, and test and develop TSCs in such a way to improve and optimise the system's applicability for the UK and any other countries with similar geographical situation which do not receive high levels of direct insolation at ground level.

In spite of the apparent simplicity of the approach, the thermodynamics and fluid-dynamics characterisation of TSCs is complex. A variable turbulent external flow approaches the absorber surface, and a boundary layer forms over the plate, governing heat and airflow transfers. The pressure drop across the perforated plate induces suction of air through perforations with the consequent formation of jet flows within the plenum. All types of sensible heat transfer establish at the same time, including convection on both sides of the perforated plate, conduction through the steel plate and radiation. The multi-scale geometrical nature of the system inherently complicates the way these processes affect system thermal response and efficiency.

Whilst experimental analysis of TSC systems will be an essential element of these systems' development, it is costly and time consuming, and needs to be supported by robust analytical predictions. Numerical techniques however, and in particular three-dimensional Computational Fluid Dynamics (CFD), offer more flexible, faster and less expensive techniques to perform tests. CFD is a branch of fluid mechanics that provides the capability to simulate fluid flows and predict the associated features using numerical algorithms. Due to complexity and the enormity of calculations, computers are employed to solve and analyse fluid flows which has led to specialised commercial packages developed exclusively to replicate fluid motion. STAR-CCM+ is a powerful CFD package which has been used in this study to model the performance of transpired solar collectors. The models are based on the geometry of a prototype system installed on the south-faced façade of an unoccupied residential building at Oxford Brookes University.

1.2 Research aim and objectives

The aim of the present work is to perform an optimisation and parametric study on the basis of an accurate numerical model of the complex fluid flows and heat transfer mechanisms that form the basis of Transpired Solar Collectors (TSCs). This model will be used to improve the current understanding of the underlying physics of TSC systems; and at the same time improve critical aspects of system performance and efficiency. The model will rely on Computational Fluid Dynamics (CFD) based approaches.

The objectives that support this aim were to:

1) Review the current state-of-the-art TSC technology and the methods of simulating and predicting system performance. This involved an international literature review and assimilation of all previous and ongoing work in the area.
2) Develop improved CFD modelling techniques to represent the complex heat transfer and fluid flows that occur in TSCs such that all the effective parameters are included.
3) Use the model to conduct a series of parametric studies to ascertain the sensitivity of TSCs to key design variables including flow rates, absorber plate thermal conductivity, sun position/day time, and related climatic conditions. The results form a basis for performance optimisation of the physical attributes of systems.
4) Use the developed model to optimise physical attributes of the absorber plate including perforation design, size, and the absorber plate thickness.

1.3 Thesis Outline

The structure of the thesis is briefly listed as follows:

- Chapter1: Introduction and background.
- Chapter 2: Literature review

This chapter contains a literature review of the background and current state of study of TSCs and the associated fluid physics describing the performance of TSCs.

- Chapter 3: Research methodology

The methodology of this study is described in this chapter which includes techniques and approaches employed to develop the CFD model. Moreover, the validation process performed to verify the model will be presented in this chapter.

- Chapter 4: Results and discussion

This chapter presents the parametric studies carried out to demonstrate system sensitivity to climatic variables, fan power, and thermal conductivity of the absorber plate. This chapter also presents the optimisation carried out to find geometrical features of the absorber plate delivering the highest possible Heat Exchange Effectiveness in TSCs. A correlation has also been developed for Heat Exchange Effectiveness in terms of geometrical variables of the absorber plate (diameter of perforations, pitch distance and plate thickness) under one climatic condition.

- Chapter 5: Conclusions and recommendation

Chapter 2 Literature Review

2.1 Introduction

Fluid flow and heat transfer mechanisms in Transpired Solar Collectors (TSCs) have been the subject of sustained research interest. Despite this however, and as described in this chapter, comprehensive methodologies for predicting performance are still not available, and hence the intention of this research project is to address key gaps in the knowledge. The following sections describe key aspects of performance and reviews of related theory and previous research. Critically these sections also identify areas of potential inadequacy required to be addressed within the scope of this study.

2.2 Boundary Layer and Starting Length

At the fluid-solid interface, fluid is assumed to have zero velocity relative to the boundary. This generates a considerable velocity gradient from the interface into the main stream. Consequently, the gradient causes a flow resistnace influencing a layer of fluid about the immediate adjacent area of the boundary. This layer is defined as boundary layer. There is a considerable thermal interaction between solid surfaces and incorporated fluid flows across the boundary layer. Thus the boundary layer affects both the thermodynamics and the fluid mechanic mechanisms that, within the case of TSCs, has a major influence on the system performance. Proper evaluation of this solid-fluid heat transfer requires appropriate information regarding flow characteristics.

Due to the consistent effect of the generated gradient, the boundary layer grows as the fluid moves along the sold interface. Different parts of the layer however experience various velocity approching the main stream velocity (Figure 2-1). The point at which the fluid velocity reaches 99% of the main stream velocity defines the thickness of the boundary layer. For a non-perforated flat plate the laminar boundary layer grows in proportion to $x^{1/2}$ where x is the distance from the leading edge of a plate (Figure 2-1). Further downstream the layer becomes turbulent and grows more rapidly, proportional to $x^{4/5}$ (Bejan, 1984).

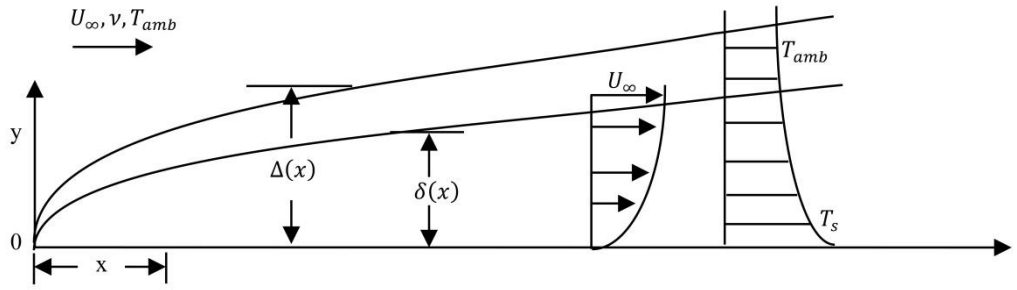

Figure 2-1. Velocity and thermal boundary layers for laminar forced convection over a flat plate.

With the similar concept, thickness of the thermal boundary layer is defined at the point which the influence of the solid on fluid temperature becomes negligible ($\Delta(x)$).

Schlichting (1979) conducted research on the effect of homogenous suction at fluid-solid interfaces over perforated plates. Homogenous suction was found to draw the boundary layer through the perforations maintaining the thickness of the boundary layer after a starting length. The boundary with the constant thickness over the perforated plate is referred as the asymptotic boundary layer. Suction produces considerable stability postponing laminar-turbulent transition considerably compared to the no-suction condition. In other words, homogenous suction stops turbulent flow to occur at further downstream on the perforated flat plate. Figure 2-2 shows the effect of homogenous suction velocity on the boundary layer over a flat plate.

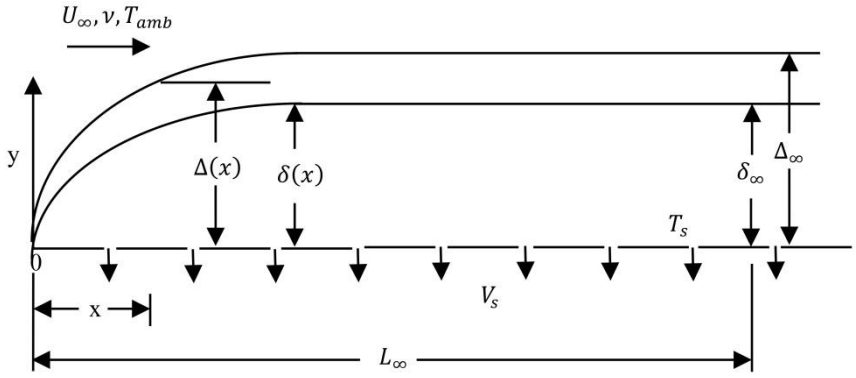

Figure 2-2. Velocity and thermal boundary layers of laminar flow over a perforated flat plate with suction.

By assuming very large x, $\partial u/\partial x$ tends to zero and by continuity $\partial v/\partial y$ equals to zero. Having $v = -V_s$ for sufficiently large x, Schlichting (1979) linearised the x-momentum equation into:

$$-V_s \frac{du}{dy} = \nu \frac{d^2u}{dy^2} \qquad (2\text{-}1)$$

Applying boundary conditions and integrating twice with $u = 0$ at the wall and $u = U_\infty$ at infinity, the velocity profile becomes:

$$u = U_\infty(1 - e^{-\frac{V_s y}{\nu}}) \quad (2\text{-}2)$$

which defines the shape of the velocity boundary layer.

Whilst these calculations assume homogenous and uniform suction through the plate, discrete suction is more likely to exist in plates where the perforations spacing is larger than the thickness of the boundary layer (Arulanandam et al. 2000). Where there is a sufficient spacing between perforations, the existence of suction decreases the velocity boundary layer thickness around perforations. The flow behaviour around perforations is described further in Chapter 4.

In a solution developed for prediction of the asymptotic boundary layer, Kutscher (1992) defined a correlation for the starting length (L_s) taking place before the flow reaches the asymptotic region:

$$L_s = 0.96\frac{U_\infty \nu}{V_s^2} \cong \frac{U_\infty \nu}{V_s^2} \quad (2\text{-}3)$$

This implies that the asymptotic boundary layer never exists where the suction velocity is zero.

Kutscher (1992) comparably assumed that there should be a region along the perforated plate where there is a heat balance between the heat sucked through perforations and the heat transferred to the fluid from the plate.

Following a similar procedure as for momentum equation, the energy equation is linearised :

$$-V_s\frac{dT}{dy} = \alpha\frac{d^2T}{dy^2} \quad (2\text{-}4)$$

which implies the same shape as the velocity boundary layer for the temperature boundary layer. Moreover, the convection heat loss length (L_e) corresponding to the thermal boundary layer was estimated by to be:

$$L_e = \frac{L_s}{Pr + Pr^2} \quad (2\text{-}5)$$

Consequently, the theory indicates that no heat loss would take place in the asymptotic region and all the heat moving away from the plate is equivalent to the heat loss occurring at the starting length.

Experimentally recorded profile of temperature and velocity for a range of suction rates were reported by Verrolet et al. (1972) in Kutscher's study showing the turbulent boundary layer on the wall subjected to heat and suction. The highest suction ratio tested however was 0.003 which was considered to be significantly lower than typical ventilation applications considered in Kutscher's work and could not maintain an asymptotic boundary layer. The profiles were used in the numerical calculations in the same way as had been used for the laminar cases. The resulted convective heat loss was found to be an order of magnitude bigger than that of asymptotic boundary layer profile. Hence it was stated that the difference would be negligible at the typical suction ratios and the hypothesis of laminar boundary layer would be consistently valid.

The assumption of an asymptotic boundary layer has been made by a number of researchers which simplifies the numerical analysis to a repetitive region with similar flow behaviour around the perforations (Arulanandam et al., 2000; Gawlik and Kutscher, 2002; Collins and Abulkhair, 2014). This assumption however is contradictory to the nature of airflow around and across TSCs. Further discussion of this assumption is described in the following sections.

2.3 Heat Transfer Theory

Heat transfer is the main factor that defines the thermal performance of TSCs. Extensive research has been carried out regarding the various mechanisms that exist over the absorber, within the plenum, and generally throughout TSCs. Investigations have also been carried out to identify the influence that climatic and geographical variables have on system performance. This section reviews salient aspects of the relevant literature.

Sparrow and Ortiz (1982) were the first researchers to investigate the heat transfer taking place between a perforated plate and a normal airflow as induced by suction under no-wind conditions. Their experiments were performed for Reynolds numbers ranging between 2,000 and 20,000. Porosities of 14% and 22% were considered these being significantly higher than porosities of interest for transpired solar collectors which are less than 2%. Correlations were developed for front surface heat transfer in terms of Nusselt numbers for two P/D ratios:

$$Nu_p = 1.78Re^{0.476},\ \mathrm{P/D_h}=2.0 \qquad (2\text{-}6)$$

$$Nu_p = 1.62Re^{0.476},\ \mathrm{P/D_h}=2.5 \qquad (2\text{-}7)$$

where $Nu_p = hP/k$ and $Re = VD_h/\nu$. The length scale of Nu_p is pitch distance (P) whilst the length scale used for Reynolds number was the hydraulic diameter of the perforations (D_h). The Nusselt number was defined in terms of heat transfer coefficient (h) based on the difference between plate and inlet temperatures. Although the expressions are not applicable for typically designed transpired solar collectors, the work did identify the significance of pitch distance and hole diameter as being important parameters within overall heat transfer evaluation.

The aim of Kutscher's (1992) research was to evaluate the thermal performance of flat transpired solar collectors through different conditions. Subsequently a heat transfer theory was developed for these systems.

Applying an energy balance on the collector plate yielded:

$$\rho C_p V_s A_c (T_{out} - T_{amb}) = \alpha I_c A_c - Q_{loss-rad} - Q_{loss-conv} \quad (2\text{-}8)$$

where ρ is the air density, C_p is the air heat capacity, $Q_{loss-rad}$ refers to the radiative heat losses and $Q_{loss-conv}$ the convective heat losses. Radiative heat losses were assumed to occur to the sky and to the ground depending on the tilt of the collector. The radiant heat loss to the wall behind the plenum was considered to be negligible. Hence the radiant heat loss was defined as:

$$Q_{loss-rad} = \varepsilon_c \sigma_{sb} A_c (T_s^4 - F_{cs} T_{sky}^4 - F_{cg} T_{gnd}^4) \quad (2\text{-}9)$$

where ε_c is the collector plate emissivity, σ_{sb} is the Stefan-Boltzmann constant, F_{cs} is the view factor between the collector and the sky, and F_{cg} is the view factor between the collector and the ground. Natural convective heat losses were considered to be negligible compared to the forced convective heat losses based on analysis performed in the same study. It is identified that the suction rate increases the heat gain of the collector and reduces convective heat loss.

Gunnewiek et al. (1996) used CFD tools to study heat transfer mechanisms and fluid flow in the plenum for zero-wind conditions over a range of typical parameters. The energy equation was written for the asymptotic boundary layer; and due to the absence of wind, long-wave radiation was considered to be the only heat loss. Three energy terms were defined for the thermal performance assessment: the heat delivered into the system through the external surface of the absorber (Q_{in}), the heat that leaves the plenum into the building (Q_{out}), and the heat transfer at the back of the plate (Q_b), equal to $Q_{out} - Q_{in}$.

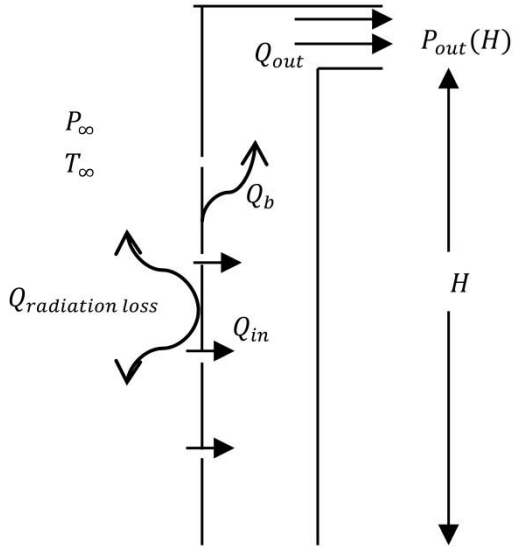

Figure 2-3. Schematic diagram of parameters considered in Gunnewiek et al. (1996).

The results showed that Q_b made a considerable contribution to the overall heat exchange between the system and the air. Depending on the uniformity of flow in the plenum Q_b varied from negative to positive values. Uniformity of the airflow was scaled using the term $\Delta P_{out}/\Delta P_{po}$, where ΔP_{out} is the pressure difference across the collector and ΔP_{po} is the pressure drop across the plate when the flow is uniform. The pressure difference that the fan needs to suck air into the building was given as:

$$\Delta P_{out}(H) = P_\infty - \rho g H - P_{out}(H) \quad (2\text{-}10)$$

where $P_{out}(H)$ is the mass averaged pressure at the plenum exit (Fig. 3). Implicitly, the zero value of Q_b is related to the uniform flow in the plenum where no heat transfer takes place. It was illustrated that the non-uniform flow in the plenum could experience two types of flow, forced and buoyancy dominated, leading to negative and positive values of Q_b, respectively. In other words, depending on whether fan power or buoyancy is the main driving force, the airflow would travel through a cooling process (negative Q_b) or vice versa (positive Q_b) from the bottom to the top of the plenum. Based on the pressure drop study, it was found that the minimum suction velocity that prevents reverse flow over the external surface of the collector is 0.0125 m/s.

2.4 Heat Exchange Effectiveness and Temperature Rise

Heat exchange effectiveness and temperature rise are commonly used to assess the performance of TSCs. Evaluation of these parameters, enables designers to predict outlet temperatures.

Heat Exchange Effectiveness (HEE) represents the actual heat transferred to the air relative to the maximum possible heat transfer that could take place between the system and the flowing air. HEE is generally defined in terms of ambient temperature (T_{amb}), outlet temperature (T_o) and absorber surface temperature(T_s):

$$\varepsilon = \frac{(T_o - T_{amb})}{(T_s - T_{amb})} \quad (2\text{-}11)$$

The ultimate goal of Kutscher (1992) was to determine the thermal performance of TSCs with triangular pitch. Heat exchange effectiveness was defined as:

$$\varepsilon = 1 - exp(-NTU) \quad (2\text{-}12)$$

where

$$NTU = \frac{UA_s}{\dot{m}c_p}$$

In order to determine the overall heat transfer coefficient of the collector an experimental and numerical study was performed on several plates with different geometries (thickness, pitch distance, and perforation diameter) and suction rates. All were based on circular perforations in a triangular layout.

The numerical study was carried out using the CFD software FLUENT with 2-D and an axisymmetric condition in the absence of wind in the model. Heat transfer was considered to occur in three regions (the front surface, within the perforations, and at the back surface). The intention was to determine heat transfer coefficients based on log mean temperature for each region in order to evaluate the overall heat transfer coefficient 'U'. Simulations were run for 5 different plates at various suction velocities.

Wind-existing cases need to be three dimensional and modelling is not physically realistic under axisymmetric conditions (modelling would be expensive and protracted). Thus the cross-flow investigation was left to be carried out by experimental tests. Moreover because of the computational capacity limitation, pitch and diameter variation for Fluent tests were restricted to a high porosity region. Porosity refers to the surface area ratio of the perforations to the perforated sheet. Therefore, the result cannot be representative of low porosity plates.

The heat transfer coefficients for the front surface, hole and back surface of the perforated plate were developed separately in terms of local Nusselt number correlations.

Front surface heat transfer was predicted to be mainly pitch dependent so as the relationship between the *Nu* and *Re* number was fitted based on pitch distance following the work of Sparrow and Ortiz (1982).

Heat transfer in the hole, in contrast, was determined to be influenced by both pitch and diameter. A best fit curve was generated using the Nusselt number correlation for laminar flow from Sieder and Tate (1936). Back surface heat transfer was also best fitted with the pitch-based Reynold number. Back surface heat transfer, however, was expressed in terms of Stanton number implying the effect of thermal heat capacity of the plate.

A single general model was developed based on these results using a log mean temperature difference for the Nusselt numbe:

$$Nu_D = 9.075\left(\frac{P}{D}\right)^{-1.384} Re_D{}^{0.2523} \quad (2\text{-}13)$$

Due to the dominance of heat transfer at the front surface another curve fit was generated to emphasize the importance of pitch distance which yielded to:

$$Nu_P = 8.676\left(\frac{P}{D}\right)^{-0.1146} Re_D{}^{0.2618} \quad (2\text{-}14)$$

It is notable that no statistical assessment factor (e.g. RMSE) could be found for the regression and data fittings.

The experimental study included both no-wind and cross flow conditions. The first tests comprised a16 run experiment of 8 different geometries of absorber plate to evaluate the influence of the three geometry parameters (thickness, pitch distance, and perforation diameter) and suction mass flow rate. Statistical analysis showed that mass flow rate, pitch distance and hole diameter have the most significant impact on heat exchange effectiveness and heat transfer coefficient. The impact of interaction between the parameters was also investigated where cross-interaction between pitch and mass flow rate demonstrated a notable effect. Plate orientation and wind effects were also addressed. Only two cases of wind speed were explored: 0 and 3 m/s. It was interesting that existence of wind decreased the effect of diameter compared to the no-wind conditions and wind effect was found to be the most significant parameter after mass flow rate and pitch. The Nusselt number was correlated based on log mean temperature difference as:

$$Nu_D = 2.74\left(\frac{P}{D}\right)^{-1.2} Re_D{}^{0.43} \quad (2\text{-}15)$$

The coefficient of determination, R^2, of this regression was stated to be 99%. In this equation Re_D is the Reynolds number based on the flow velocity in the holes and the diameter of the holes.

Extended experiments with the existence of parallel streaming wind (1, 2 and 4 m/s) was extrapolated with the regression line and yielded:

$$Nu_D = 2.74\left(\frac{P}{D}\right)^{-1.2} Re_D{}^{0.43} + 0.011\sigma Re_D \left(\frac{U_\infty}{V_s}\right)^{0.48} \quad (2\text{-}16)$$

where σ is the plate porosity. R^2 for this regression was stated to be 92.6%.

These expressions were stated to be valid for plate porosities of 0.1 to 5% and hole Reynolds number of 100 to 2000. As the correlation shows, the important parameters determining the heat transfer coefficient are suction flow rate, wind speed, perforation diameter, and pitch distances.

Cao et al. (1993) also studied heat exchange effectiveness through a two-dimensional numerical analysis. The external flow was considered to be parallel to the plate with rectangular narrow slots. Heat transfer was assumed to take place at the front side of the plate and within the perforations. Accordingly, they found that 20% of the total heat transfer occurs in the perforations. Three non-dimensional parameters were presented to be the main factors affecting the heat exchange effectiveness definition: non-dimensional slot width, *W/L*; non-dimensional thickness, *t/L*; plate Admittance defined as $k_s t/kL$; where *W* is the slot width, *L* is the distance between the slots, t is the plate thickness, and k_s and k are the thermal conductivity of the plate and air, respectively.

Golneshan (1994) studied the same geometry by a two dimensional momentum integral analysis. Experiments were also carried out on four different plates in the asymptotic region with the wind parallel to the plate and transverse to the slots. Based on the numerical and experimental investigation it was found that the heat transfer on exterior side of the plate is dependent on a non-dimensional parameter γ which is equal to Re_V^2/Re_U. Moreover Re_V and Re_U represent the Reynolds numbers based on suction velocity and wind speed respectively. Extended investigations (Golneshan and Hollands, 2000) introduced a correlation for effectiveness as:

$$\varepsilon = (1 + a\gamma^{1/2})^{-1} \quad (2\text{-}17)$$

where *a* is an empirical constant. Importantly, the correlation retains the influence of wind speed and suction velocity on heat exchange effectiveness.

Arulanandam et al. (2000) carried out an investigation to define heat exchange effectiveness of transpired plates with square-layouts of perforations using CFD under no-wind conditions. Along with Cao et al. (1993), heat transfer was considered to occur in two regions: the front surface of the plate and

in the holes. Accordingly, the back of the plate was considered to be adiabatic. As the effects of wind were excluded from the investigation, the assumption of asymptotic boundary layer was straightforward. The study was carried out to extend the range of parameters considered in Kutscher's (1992) research. A non-dimensional group of parameters were used to transform the equations and boundary conditions into non-dimensional equations: the plate porosity $\sigma = \pi D^2/4P^2$, where D is hole diameter and P is pitch distance. Reynolds number $Re_D = \frac{V_h D}{\nu}$, where V_h, the velocity in the hole, was defined in terms of suction velocity (V_s) as: V_s/σ ; non-dimensional perpendicular-distance to the plate $x_\infty^* = x_\infty/D$; non-dimensional plate thickness $t^* = t/D$; the 'plate Admittance' $Ad = k_s t/kD$; and radiative Nusselt number $Nu_r = h_r D/k$ where h_r represents the radiative heat transfer coefficient . Finally, a Nusselt number was defined in terms of the non-dimensional numbers:

$$Nu_D = \frac{5.25 {Re_D}^{0.36} \sigma^{0.78}(1 + 0.15t^*)}{1 + \frac{7.89}{13 + Ad}} \qquad (2\text{-}18)$$

A good agreement was found between the results of the latter expression and Kutscher's (1992) work. Kutscher broke down the total heat transfer into three exchanging zones; this agreement was held whilst the heat transferred by the back surface was excluded from the analysis.

Lower conductivity plate materials resulted in non-uniform temperature across the plate surface. In other words, lower levels of velocity in the regions far from the holes can cause higher levels of temperature, which increase the radiative heat losses to surrounding air. This effect could be negligible with high conductivity materials. The evaluation of TSCs by means of non-dimensional parameters demonstrated that satisfactory heat exchange effectiveness can be achieved even with low conductivity materials for the perforated plate by optimizing other dimensional parameters.

Van Decker et al. (2001) extended Kutscher's (1992) work to a wider range of plate thickness, pitch distance, suction velocities and square pitch layout of perforations. The aim was to develop a predictive model for heat exchange effectiveness. Hence the experiments were performed for both windy and no-wind conditions for nine different plate geometries. Flow suction was considered to be uniform through the perforations and convective heat loss was considered to be not significant (Kutscher, 1992). The plates were subjected to a wind velocity range of 0 to 5m/s and suction velocity was 0.028 to 0.083 m/s. The tests were run for different plates with various geometries and materials.

Similar to Kutscher's study, the new model identified heat transfer to take place in three different parts of the plate and defined three heat exchange effectiveness' for these three parts separately: the

external surface of the plate (ε_f), the hole (ε_h), and the back of the plate(ε_b). Accordingly, HEE was identified to be:

$$\varepsilon = 1 - (1-\varepsilon_f)\,(1-\varepsilon_h)\,(1-\varepsilon_b) \quad (2\text{-}19)$$

$$\varepsilon = 1 - (1-\varepsilon_b)/\,(1-\varepsilon_{fh}) \quad (2\text{-}20)$$

Here, ε_{fh} was defined as combined HEE of ε_f and ε_h. Each HEE correlaition was seperatly derived using Golneshan's (1994) and Arulanandam et al. (2000) studies together with assuming $\varepsilon_{fh} = \varepsilon_f$ for the very thin experimented plates. Laminar flow was assumed to take place in the hole and was treated as a developing flow inside an isothermal circular cylinder.

A predictive model was developed based on ε_h, ε_b, and ε_f. For air with $Pr = 0.71$ the overall effectiveness can be predicted by:

$$\varepsilon = \left[1 - (1 + Re_s \max\left[1.733 {Re_w}^{-0.5}, 0.02136\right])^{-1}\right] \times \left[1 - (1 + 0.2273 Re_b^{0.5})^{-1}\right] \times exp\left(-0.01895\frac{P}{D} - \frac{20.62t}{Re_h D}\right) \quad (2\text{-}21)$$

The Root Mean Squared Error (RMSE) for this overall data fit was 4.3%.Testing the model on triangular-pitch layouts showed that applying a scaling factor of 1.6 to the square pitch distance, P, makes the model suitable for triangular pitch configurations. The correlation not only showed good agreement with Kutscher's measurements for the same conditions and plate geometry, but also addressed a wider range of operating conditions: $0.028 \le V_s \le 0.083\ m/s$, $0 \le U_w \le 5\ m/s$, $7 \le P \le 24\ mm$, $0.8 \le D \le 3.6\ mm$, $0.6 \le t \le 6.5\ mm$, and $0.15 \le k \le 200\ W/mK$.

For typical operating conditions and commercial solar collectors, the contribution of each region was predicted to be: $\varepsilon_f = 0.405$, $\varepsilon_h = 0.306$, $\varepsilon_b = 0.149$, $\varepsilon_{fh} = 0.588$, and $\varepsilon = 0.649$. Accordingly, contribution of each region to the overall temperature rise was estimated to be about 62% on the front surface, 28% within the perforations, and 10% at the back of the plate. It's notable that in contrast with the Kutscher's study, heat transfer in perforations was found to make a considerable contribution to overall heat transfer. Thickness of the plate was also found to be important to be accounted in heat exchange effectiveness predictive model.

Leon and Kumar (2007) carried out a mathematical study based on varying a set of key parameters that affect the thermal performance of TSCs over a wide range of practical design and operating conditions. Convective heat losses were assumed to be negligible according to the asymptotic boundary layer theory (Kutscher, 1992); the airflow through the perforations was assumed to be homogenous; and

the temperature profile of the absorber and the back plate (in the plenum) was assumed to be uniform across their respective surfaces. Kutscher's correlation (2-16) was used to determine the convective heat transfer coefficient of the absorber plate to plenum air. Eq.(2-22 was utilised to estimate the heat transfer from the back plate to the surrounding airflow and plenum air to the back plate:

$$Nu_L = 0.664(Re)^{1/2}(Pr)^{1/3} \quad (2\text{-}22)$$

This is a conventional correlation to calculate convective heat transfer coefficient between a flat plate and laminar parallel flow.

Finally, the radiative heat loss correlation was estimated as per (Eq. (2-9). The research presented the influence of solar radiation, suction velocity, porosity and pitch distance on the heat exchange effectiveness and temperature rise of TSCs. Estimation of heat exchange effectiveness was adopted from Kutscher (1992, Eq. (2-12). The parametric study indicated that for constant values of air flow rates and solar radiation, the smallest combination of pitch and diameter produced the highest levels of temperature rise. It was found that with constant pitch distance, heat exchange effectiveness decreases moderately with the plate porosity. Significant reduction in heat exchange effectiveness was however witnessed with pitch distance enhancement. Moreover, the results showed that an increment of suction velocity from 0.01 to 0.03 m/s leads to a 23% drop in HEE values. Similarly, a dramatic drop (around 52%) was witnessed in temperature rise when changing suction velocity from 0.0125 to 0.0375 m/s. Solar radiation, in contrast, showed a potential growth of 112% in temperature rise for low flow rates.

Chan et al. (2013) performed an analysis of heat transfer mechanism within TSCs by a theoretical-experimental study. Because of the complexity of both the heat transfer mechanisms and the sophisticated airflow, certain assumptions were applied. It was assumed that convective heat losses were negligible and that there was no significant reverse flow over the external surface of the plate. The radiative heat loss profile was also considered to be uniform across the surface of the perforated plate.

As flow suction was not assumed to be completely uniform, heat transfer was assumed to take place as air passes through the perforations (normal flow) and subsequently when air travels behind the plate in the plenum (vertical flow). Heat losses considered in their energy balance equations comprised radiative heat loss to the surroundings ($Q_{rad,p-sur}$)and heat penetrating through the insulated wall ($Q_{wall-room}$) behind the plenum. Heat loss through the wall to the corresponding indoor area included radiation from the back of the plate to the wall ($Q_{rad,bp-wall}$) and convective heat transfer taking place between the wall, and the airflow in the plenum ($Q_{conv,air-wall}$).

$$Q_{Loss} = Q_{rad,p-sur} + Q_{wall-room} \quad (2\text{-}23)$$

$$Q_{wall-room} = Q_{rad,bp-wall} + Q_{conv,air-wall}$$

Subsequently, the analysis showed that whilst heat exchange effectiveness experiences a dramatic drop with an increase in mass flow rate, solar radiation can cause a significant increase in HEE which is in agreement with the results from the earlier studies. The analysis of different plenum depths indicated that there would be an optimum, which can be attributed to the situation of flow uniformity in the plenum (Gunnewiek et al., 1996). The researchers presented temperature rise in terms of normal flow temperature rise ($T_i - T_a$), which is the temperature difference between the temperature of the air passing through the perforations (T_i) and that of the ambient air (T_a), and the vertical flow temperature rise ($T_{out} - T_i$), which refers to the air temperature growth from the bottom to the top of the plenum. Temperature rise showed an increasing trend with increase in solar irradiance. Increasing solar irradiance also increases the share of the vertical temperature rise from 50% to 59% of the total temperature rise. The result implied the significant contribution of heat transfer occurring in the plenum from the back of the plate. Consistent with the effectiveness, the 'temperature rise' experienced a reduction from 13.2 K to 9.3 K with altering mass flow rate from 0.039-0.062 $kgs^{-1}m^{-2}$.

Hall et al. (2014) studied two prototypes of novel, flat cassette-panel TSCs to assess the thermal performance of the systems. These novel TSCs were developed to provide more aesthetically appealing systems by combining cassette cladding panels designed for prestige office and high-rise residential buildings with TSC solar air-heating technology. Measured data showed that second floor system generated a slightly higher temperature rise than that of the first floor, and this was explained as the result of the difference in plenum depth. This could be justified referring to the different airflow uniformity that establishes in the plenum (Gunnewiek et al., 1996). Generally, the systems demonstrated a 10-15℃ temperature rise for a clear day in winter.

Li et al. (2013) focused on both corrugated and flat plates to investigate asymptotic boundary layers over transpired solar collectors. It was specifically pointed out that the nature of flow in TSCs does not comply with the homogenous suction theory of Schlichting (1979), hence the criteria for asymptotic boundary layer assumption cannot be met. The results showed that the asymptotic boundary layer is not maintained unless for high suction rates which may not be practical. Based on this research, Li et al. (2014) extended their work to develop a heat transfer correlation for a corrugated TSC with and without Photo Voltaic (PV) modules. Their CFD model was developed based on assumptions made to simplify the complexity of the analysis. Although the non-uniformity of the airflow was recognised by the

authors according to the literature (Gunnewiek et al., 1996; Dymond and Kutscher, 1997), the airflow rate was assumed to be uniform and the temperature profile was also considered to be constant along the cross section of the cavity. Solar radiation distribution was presumed to possess a uniform profile over the corrugated absorber.

Both external ($h_{c.ext}$) and internal ($h_{c.ext}$) average convective heat transfer coefficients were calculated using the respective surfaces' heat flux, and the surface averaged temperature alongside the relevant air temperature. Subsequently the convective heat transfer coefficients were estimated using Nusslet number correlations that considered wind speed and suction velocity, together with geometrical parameters:

$$Nu_{ext} = \left(\frac{p}{e}\right)^{A1}\left(\frac{e}{L}\right)^{A2}\left(\frac{w}{p}\right)^{A3}[B1.Re_U^{C1} + B2.Re_V^{C2}] \quad (2\text{-}24)$$

$$Nu_{int} = (\frac{p}{e})^{A1}(\frac{e}{L})^{A2}(\frac{w}{p})^{A3}(\frac{e}{D})^{A4}[B1.Re_U^{C1} + B2.Re_V^{C2}] \quad (2\text{-}25)$$

In these correlations Re_U is based on wind speed and Re_V is based on suction velocity. Geometrical parameters used in the correlation are shown in Figure 2-4. A1, A2, A3, A4, B1, B2, C1, and C2 are the correlations coefficients.

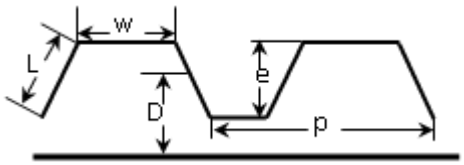

Figure 2-4. Sketch of geometry parameters used in Li et al. (2014)

2.5 Thermal Efficiency

The other crucial factor used to evaluate the performance of TSCs is the overall thermal efficiency. This provides an insight into the portion of collected energy that is actually delivered into buildings. The thermal efficiency of TSCs is calculated as the ratio of the heat transferred to the air through the system to the total solar energy that falls on the TSC surface:

$$\eta = \frac{\dot{m}c_p(T_{out} - T_{amb})}{IA_s} \quad (2\text{-}26)$$

where I is solar heat flux and A_s is collector surface area. Having T_s and heat exchange effectiveness determined, the thermal efficiency can also be defined as (Kutscher, 1992):

$$\eta = \frac{\rho c_p \varepsilon V_s (T_{coll} - T_{amb})}{I} \quad (2\text{-}27)$$

Kutscher (1992) indicated that at the constant suction mass flow rate, maximum efficiency takes place at the zero wind condition due to increasing heat loss with the growth in wind speed. However, it was found that a higher level of suction rate decreases the magnitude of heat loss as this captures more of the available heated air adjacent to the absorber plate.

Gunnewiek et al. (1996) also studied the impact of the flow uniformity in the plenum on the thermal efficiency of TSCs. The thermal efficiency, referred to the fraction of incident solar energy transferred into the airflow, and was defined as $\eta = q_{out}/(IA) = \alpha q_{out}/(\alpha IA)$. Respectively η/η_{uni} was defined as the ratio of the actual efficiency to the value assumed in uniform flow conditions. The results showed that for different ranges of variables, the main driving force in the plenum can be either buoyancy or fan power (forced flow). The buoyancy dominated flow refers to the flow caused by temperature difference that induces air to travel from the bottom of the cavity to the top, whereas the forced flow draws air mainly from the top region of the cavity. For typical operating conditions, the η/η_{uni} ratio showed to range from 0.8 to 1.09. As discussed in Section 2.3, non-uniform buoyant flow causes positive heat transfer in the plenum region between the plate and the airflow. Correspondingly, for buoyancy-dominated flow in the plenum region and no reverse flow over the plate, non-uniform flow demonstrated high potential levels of thermal efficiency.

Dymond and Kutscher (1997) developed a computer model for TSC design which could easily accommodate geometric parameters to reach maximum efficiency. The aim was to allow designers to achieve reasonable flow uniformity and to determine efficiency of the system. Running the computer model for a 5 m × 10 m collector, profiles were produced for flow distribution (face velocity), temperature distribution and thermal efficiency for design analysis.

The results demonstrated that the face velocity peak takes place at a region close to the outlet hole (Figure 2-5). Lower values of velocity far from the top center of the collector could be a consequence of three different pressure drops that flow experiences through the collector: the acceleration pressure drop in the plenum, the frictional pressure drop, and the buoyancy pressure drop of the heated air. As expected, the top left and top right corners of the collector were witnessed to have the lowest velocity (called the starving points), where reverse flow could take place. Compared to velocity, the temperature profile showed an opposing trend reflecting the proportionality between convective heat transfer and airflow

velocity. The efficiency profile demonstrated a similar shape to the velocity profile. Higher amount of flow through the collector was perceived to transfer more heat from the absorber plate.

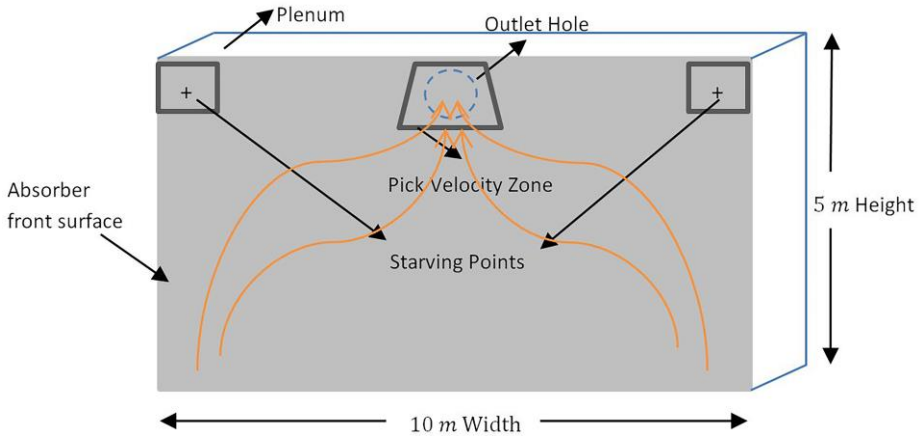

Figure 2-5. Schematic diagram of geometric configuration of the absorber studied in Dymond and Kutscher (1997).

An experimental study carried out by Fleck et al. (2002) investigated the thermal performance of TSC as a function of local meteorology. The recorded fluctuations of velocity close to the wall illustrated high levels of turbulence that would affect heat transfer. Subsequently, the theory of laminar boundary layer was considered to be non-realistic.

According to the measurements, solar radiation had the highest impact on thermal efficiency. Specifically, the measured data showed a decreasing trend of collector efficiency with increasing solar radiation. It was explained that higher solar radiation causes higher collector surface temperature, which consistently results in more radiative and convective heat losses to the surroundings. Low irradiance may cause higher levels of uncertainty concerning thermal performance estimation. Solar radiation less than 200 W/m^2 was excluded from the study. Thermal efficiency was estimated against mean wind speed. The collector maximum efficiency occurred when the wind speed was between 1-2 m/s, but no explanation was given concerning this surprising result except that this behaviour could be relevant to the influence of other variables such as wind direction and solar intensity. Importantly, the latter result was in agreement with experimental investigation later carried out by Cordeau and Barrington (2011), who reported that the highest thermal efficiency (over 65%) occurred for a wind speed of 2 m/s. Also coherent among each other, these findings are in contrast with the work of Kutscher (1992), which predicted maximum thermal efficiency at zero wind conditions with a decreasing trend as wind speed increases.

Fleck et al. (2002) reported a decreasing trend for efficiency with increase in turbulent kinetic energy which supports the hypothesis that turbulent fluctuations carry the heat away from the collector surface by very small-scale motions. They also measured thermal efficiency against wind direction, however no specific trend was found.

Biona et al. (2005) developed a repetitive computing model to generate practical performance curves for TSCs, studying different hole diameters and pitch distances with suction velocities between 0.2 and 0.6 m/s. The fan power required to generate negative pressure was taken into account for collector efficiency assessment. The results confirmed Kutscher's (1992) theory that the collector efficiency rises with increases in suction velocity. However, an increase in flow rate leads to larger fan power and this would be considerably augmented for low porosity plates causing a fall in efficiency. The results imply that there would be optimised perforation geometry for any particular application. The performance curves showed that collector efficiency decreases with increasing hole diameter for plates with small pitch distances whereas this impact was shown to be very small for moderate pitch distances. In other words, pitch distances could demonstrate a positive effect for perforations with larger diameters. This could be justified by the fact that smaller perforations contribute to larger net area for solar radiation collection.

Focusing on the role of conductivity in highlighted by the work of Golneshan (1994), Arulanandam et al. (2000), and Van Decker et al. (2001); Gawlik et al. (2005) studied the influence of plate conductivity on the thermal performance of TSCs. A low-conductivity plate (styrene) and a high conductivity one (aluminium) were investigated through numerical and experimental tests. Experiments were performed for three different mass flow rate and two different plate geometries. Conductivity was shown not to be a major factor affecting thermal efficiency, except for very unrealistic low-conductivity materials beyond the range of interest. A gradient of temperature was reported to take place between the holes in low conductance plates that created hotter regions between holes. However, due to the small pitch the temperature gradient could not grow significantly between holes. Higher convective heat transfer is expected to take place in the hotter regions while lower convective heat transfer should occur in regions with lower surface temperatures. Conceivably, the mean radiant surface temperature of low conductance plates was stated to be close to the uniform temperature of high conductivity materials. Hence, it was concluded that the total radiant heat loss was independent of plate conductivity.

Mathematical model of Leon et al. (2007) revealed a considerably smaller effect of pitch distance on collector efficiency than HEE. The study also showed that the effect of porosity on thermal efficiency is

not substantial. Higher pitch distances provide potential for hot spots to occur over the collector surface which could result in higher radiation heat loss and lower thermal efficiency (Arulanandam et al., 2000). This study was in agreement with previous studies where suction velocity was seen to enhance the thermal efficiency particularly at low suction velocities.

Cordeau and Barrington (2011) investigated the thermal efficiency of a transpired solar collector working as an air-preheater system for broiler barns. Atmospheric parameters were measured by an on-site weather station. It was shown that thermal efficiency fell from 65% to 25% as wind velocity increases from 2m/s to 7 m/s. The highest level of thermal efficiency was again recorded to occur at 2 m/s.

The study of Chan et al. (2013) supported earlier studies that solar radiation and mass flow rate have high impacts on thermal efficiency. Changing solar radiation intensity from 307 to 820 W/m^2, resulted in an increase of approximately 28% in thermal efficiency. The role of plenum depth in terms of thermal performance was also investigated with three different depths being reviewed: 0.20 m, 0.25 m, and 0.30 m. Under similar operating conditions, a plenum depth of 0.25 m generated the best performance. It was explained that this depth provides buoyancy-dominated flow as opposed to forced flow caused by fan power, and the finding is in agreement with the work of Gunnewiek et al. (1996) concerning the influence of flow uniformity in the plenum.

The impact of turbulence intensity and suction velocity on the thermal efficiency of TSCs were investigated by Li et al. (2013). A CFD model was used and validated against experimental data as a flexible tool for the investigation. An investigation was performed on corrugated and flat perforated plates, assuming a constant ambient air temperature of 300 K and heat flux on the plate of 1029 W/m^2. The CFD results revealed that alteration of suction velocity from 0.01 to 0.06 m/s increased thermal efficiency by approximately 40 %. This was stated to be as a consequence of a reduction in the thickness of the thermal boundary layer over both the corrugated and the flat plates (50% and 33%, respectively). Based on homogenous suction theory, higher suction velocity leads to lower convective heat loss along the perforated plate, with the thermal efficiency reaching circa 90% for the flat TSC. However, convective heat loss was still stated to be a large contributor to the overall thermal efficiency, particularly for lower suction rates. Turbulence intensity had only a minor impact on thermal efficiency compared to suction rate. Increasing turbulence intensity from 0.1% to 20% caused a decline in thermal efficiency of 2% and 6% for flat and corrugated plates respectively.

Badache et al. (2013) studied the impact of plenum depth, mass flow rate, and solar radiation on thermal efficiency. The study was carried out both with experimental tests and numerical modelling.

Consistent with previous studies (Kutscher, 1992; Leon and Kumar, 2007), the work demonstrated that increase in mass flow rate improved thermal efficiency. In contrast with effectiveness that is independent of solar radiation intensity, thermal efficiency was slightly decreased by about 3.5-5% with increasing solar radiation from 300 to 600 W/m^2. The low efficiency values were more significant at lower suction rates. Thereby it was explained that more heat loss takes place at higher levels of irradiance as moderate suction rates are not able to capture all available thermal energy. This inverse relationship between the efficiency and the solar radiation is in contrast with the results of Chan et al., (2013) whilst operating with larger plenum depths.

The efficiency variation resulted from two different plenum depth wasn't found to be significant. Efficiency decreased not more than 3.25% with plenum thickness for the two plenum depth of 50 and 150 mm.

2.6 Numerical Modelling Approaches

Several numerical models have been developed to explore the mechanism of heat transfer and fluid flow characterisation in transpired solar collectors. Different approaches have also been used to achieve 'best fit' with measured data.

Kutscher (1992) used FLUENT CFD software, to model heat transfer mechanisms in TSCs. Navier-Stokes equations were solved over the numerical domain using a finite volume approach. The flow in the perforation was approximated to behave as a flow through an orifice within a tube when the flow is perpendicular to the plate (Figure 2-6). The flow region was assumed to be hexagonal and the outlet boundary was set sufficiently far downstream so as not to be affected by flow recirculation. The flow was modelled as laminar, an approach believed to more accurately capture the boundary layer than a $k-\varepsilon$ turbulence model. It was however stated that the model assumptions could not be realistic because of jet flow and recirculation zones occurring downstream of the considered computational domain (in the plenum).

Figure 2-6. Schematic diagram of CFD model domain and streamlines - Kutscher's (1992) study.

Gunnewiek et al. (1996) employed CFD to study the performance of TSCs. A finite volume method was used to simulate the 2-D problem for no wind conditions. A two-dimensional domain and other simplifying assumptions were made to render the model computationally. The investigation focused on plenum region modelling, defining plate, and ambient regions as a pair of boundary conditions modelled by means of momentum and energy conservation equations.

A parametric form of pressure drop across the perforated plate was used for momentum balance at the front surface:

$$\Delta p_p = \rho K_H V_s^n \qquad (2\text{-}28)$$

where K_H is the plate's hydraulic impedance, and for typical values of porosity, thickness and hole diameter, n was considered to be equal to 1.5. Moreover, to decrease the complexity of the problem, the suction process was presumed to take place in a continuous state rather than through discrete holes.

According to the expected Reynolds number and classical smooth pipe internal flow, the flow in the plenum was assumed to be turbulent. Jet flow was assumed and a $k-\varepsilon$ turbulence closure model was utilised for turbulent flow modelling. The problem was solved using the basic CFD code TASCflow Version 2.2.

Dymond and Kutscher (1997) developed a computer model to be of practical use for TSC design. This was claimed to be computationally more suitable than the CFD models in existence at that time. The model took account of all four pressure drops including: friction across the collector, friction in the plenum, buoyancy in the plenum and acceleration of the fluid in the plenum. Except for the radiative heat transfer taking place between the absorber plate and the back wall in the plenum (considered to be negligible), all the other major heat transfer types were taken into account. Based on earlier experimental studies, ambient pressure changes associated with wind effects were considered modest, as long as the

pressure drop across the absorber was at least 25 Pa. It was also assumed that the back side of the absorber plate was adiabatic and no heat transfer takes place from the plate to the air in the plenum. Governing equations were applied to the problem and solved by pipe network methods. Subsequently flow distribution through the collector and temperature distribution through the collector were iteratively predicted. The model also accounted for flow non-uniformity in the plenum through buoyancy effects. Kutscher's (1992, 1994) pressure drop model through the collector, total heat transfer coefficient, and forced convective heat loss coefficient were used in the calculations.

Arulanandam et al. (2000) analysed heat transfer through TSCs under no-wind conditions. TASCflow, CFD code was again utilised to solve the governing equations over the computational domain. In addition to no-wind conditions, heat transfer from the back of the plate was neglected. Because of these limitations, the results were combined with experimental data to validate a correlation developed for thermal performance in terms of non-dimensional important parameters. A single hole geometry was studied, based on the repetition of the hole pattern over the plate. Moreover, it was assumed that the zero-wind condition provided the opportunity to consider geometrical symmetry, and to reduce the domain to a quarter of the real element. Assuming uniform flow behind the plate facilitated omission of the plenum from the modelling. No temperature gradient was therefore taken into account. Other key assumptions included steady state, no external forces, no viscous heat dissipation and laminar flow were other assumptions taken for the airflow simulations.

Gawlik and Kutscher (2002) conducted numerical and experimental modelling to study heat transfer from a perforated, sinusoidal plate with the airflow perpendicular to the corrugations. The CFD commercial software, FLUENT was used for the 2-D numerical modelling. The case was modelled as a region where both thermal and velocity boundary layers were assumed to be asymptotic and the flow field over the corrugations had a repeating pattern. Accordingly, wind heat loss was assumed to occur at the starting length. Based on the experimental data delivered in the same study, discrete holes didn't show significant effect on the 2-D boundary layer. Similar to the study carried out by Kutscher (1992) the flow was assumed to be laminar that was also verified by smoke tests for low turbulence intensities and low speed flows.

Li et al. (2013) investigated flow structure and convective heat transfer mechanism in TSCs on both flat and corrugated panel profiles using 3-D, steady state, Reynolds-Averaged Navier-Stokes (RANS), CFD simulations. According to the author no study had already covered the entire perforated plate, investigating convective heat transfer under turbulent flow conditions. A flat Transpired Solar Collector

(UTC) with uniform approaching flow and a corrugated TSC subjected to a plane wall jet were considered in the study. The PRESTO discretization scheme was used for pressure, whereas the second order upwind scheme was used to discretize all other variables (momentum, turbulent kinetic energy, etc.); the SIMPLE algorithm was used for pressure-velocity coupling. One directional uniform approaching flow was set by utilizing 'velocity inlet'- 'pressure outlet' boundary conditions, with a specified approaching flow velocity and zero-gauge pressure, respectively. Solar radiation on the plate was simulated by specification of a heat flux on the perforated plate. 'Velocity inlet' with reverse flow direction was set to the plenum exit with a specified suction velocity. Other input data were 298 K ambient air temperature and a uniform upcoming flow with 0.8% turbulence intensity. Five different turbulence closure models were assessed to identify which model delivered more consistent results with experimental data. For the surface temperature of the flat plate, the standard $k-\varepsilon$ and the RNG $k-\varepsilon$ models showed more accurate results and were more stable in terms of convergence. For the cavity outlet temperature, the generated results by all models were similar except for the Realizable $k-\varepsilon$ model. Eventually, it was stated that both the standard $k-\varepsilon$ and RNG $k-\varepsilon$ are suitable turbulence models for thermal modelling. Flow field validation was also carried out to find the most suitable turbulence model for flat plate simulations. The comparison of numerical results and experimental data acquired from the jet flow over a wood plate, showed that the $k-\varepsilon$ was the most reliable model for both thermal and flow field simulations.

Badache et al. (2013) also performed a numerical investigation on the thermal efficiency of TSCs using commercial CFD software, Fluent. A CFD model was developed under steady, turbulent, and, 2-D assumptions. Apart from convective and conductive heat transfer types, radiation was also considered to take part in the heat exchange between the absorber plate and the surroundings. RNG $k-\varepsilon$ model was used for turbulence modelling. Heat generation source was defined on the absorber plate to represent the solar radiation on the collector. Therefore, a user defined function was introduced to the software to replicate the radiative heat exchange between the absorber and the surroundings.

Collins and Abulkhair (2014) developed a 3-D CFD model to analyse a corrugated TSC system. Referring to the studies performed by Schlichting (1979) and Gawlik and Kutscher (2002), airflow was assumed to be laminar. Gravity was assumed to be negligible and wind was one directional parallel to the plate. Absorbed solar heat was applied on the perforated plate and solar heating was excluded from the model. The other assumptions were constant air properties within the operating temperature of 15-25°C together with negligible viscous dissipation terms. The laminar asymptotic boundary layer assumption

facilitated an opportunity to generate a simplified periodic model with few perforations around a corrugation. It was assumed that the profiled panel didn't have significant effect under no-wind condition. Thus a flat plate with only two perforations was modelled for this situation. Symmetric planes were applied instead of periodic boundary conditions for the latter model. Two separated regions divided by perforated plate were modelled in both cases representing ambient and plenum regions. A homogenous velocity outlet was applied to the back surface in the plenum duplicating airflow suction through perforations for both models. The model was validated against Van Decker (2001) and Kutscher (1992) results.

2.7 Airflow around buildings

Airflow distribution around buildings against different wind directions have been demonstrated in various studies. Airflow behaviour around a 6 storey building was studied by Mu et al., (2016) with the wind flow of 45° and normal direction against the building. Except for the top edge, airflow was shown to stream dominantly parallel to the building for the 45° wind direction (Figure 2-7). It was demonstrated that a stagnation zone takes place at the 5th floor wall on the windward side of the building under which the flow stream towards the ground. Above this zone the airstream recirculates over the top of the building.

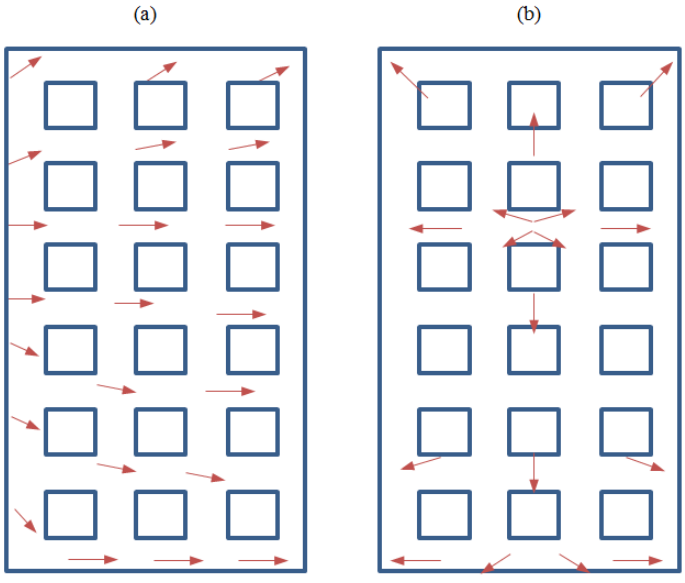

Figure 2-7. Schematic airflow distribution on the façade of building for (a) wind direction of β=45o and (b) normal wind direction β=90o showed in Mu et al., (2016)

The result is in agreement with the airflow structure provided by ASHRAE (2015) where an outflowing is demonstrated from the stagnation zone at about 1/3 to 2/3 of the building height (Figure 2-8). The experimental measurements of Fleck et al., (2002) also demonstrated a 3-D airflow at

the zone adjacent to the wall mounted also showed a similar behaviour. It was stated that the airflow around a bluff building is turbulent together with recirculation patterns. Depending on where TSCs are mounted, proper airflow behaviour should be captured consequently.

Figure 2-8. Schematic shape of fluctuation, reverse and parallel flow around a tall building for normal and oblique wind directions (ASHRAE Handbook, 2015, Section 45.3)

2.8 Turbulence Modelling

A great deal of the CFD study on transpired solar collectors has benefitted from Reynolds-Averaged Navier-Stokes (RANS) turbulence models which are more focused on the turbulence influence on the mean flow rather than the micro-properties and small fluctuations of the fluid flow (Versteeg and Malalasekera, 2007; Li et al., 2013; Tajdaran et al., 2016). RANS approach adopts Reynolds decomposition which categorises flow properties into mean values and fluctuating components e.g. $\varphi = \bar{\varphi} + \acute{\phi}$. Accordingly the Reynolds (time) averaged conservation of mass (2-27, momentum (2-30) , and scalar (Temperature) transport equations (2-31) for incompressible, steady-state flow used in the numerical simulation are as follows:

$$\frac{\partial u}{\partial x_j} = 0 \qquad (2\text{-}29)$$

$$\frac{\partial(\rho u_i u_j)}{\partial x_j} = \frac{\partial \bar{p}}{\partial x_i} + \frac{\partial}{\partial x_j}\left(\mu \frac{\partial \bar{u}_i}{\partial x_j} - \rho\overline{\acute{u}_i \acute{u}_j}\right) \qquad (2\text{-}30)$$

$$\bar{u}_j \frac{\partial T}{\partial x_j} = \alpha \frac{\partial^2 \bar{T}}{\partial x_i \partial x_j} + \frac{\partial}{\partial x_j}\left(-\overline{\acute{T}\acute{u}_j}\right) \qquad (2\text{-}31)$$

where $\alpha = \frac{k}{\rho c_p}$ is the thermal diffusivity and time-averaged values are denoted by upper head bars e.g. ($\bar{u}_i$). In the above equations *P* is the mean pressure, $\bar{u}_i$ is the mean velocity component in x_i direction, and T is the mean temperature. $T'$and $\acute{u}_i$ represent the fluctuating components of temperature and velocity respectively. $\rho\overline{u'_i u'_j}$ and $\rho\overline{T'_i u'_j}$ are the Reynolds (turbulent) fluxes arise in the momentum and scalar equations due to turbulent fluctuations. These terms are known as Reynolds stresses (τ'_{ij}) and turbulent heat flux (q_i):

$$\tau'_{ij} = -\rho\overline{\acute{u}_i \acute{u}_j} \quad (2\text{-}32)$$

$$q_i = -\rho\overline{T'_i u'_j} \quad (2\text{-}33)$$

These additional fluxes have been generated but no new equations were obtained to account for these new unknowns. The Boussinesq (1877) hypothesis is widely used to correlate the Reynolds stresses to mean rates of deformation:

$$\tau'_{ij} = \mu_t \left(\frac{\partial U_i}{\partial x_j} + \frac{\partial U_j}{\partial x_i} \right) - \frac{3}{2} \rho K \delta_{ij} \quad (2\text{-}34)$$

where K is the turbulence kinetic energy and μ_t is the turbulent viscosity and $\delta_{ij}$is the Kronecker delta function ($\delta_{ij} = 1 \; if \; i = j \; and \; \delta_{ij} = 0 \; if \; i \neq j$). Then for turbulent heat flux:

$$q_i = -\alpha_t \frac{\partial T}{\partial x_i} \quad (2\text{-}35)$$

where α_t is turbulent thermal diffusivity. Since both transport equations are developed under same mechanism it is routinely assumed that $\alpha_t = \mu_t$ which is also addressed by turbulent Schmidt number i.e. $\sigma_t = \mu_t / \alpha_t = 1$ (Versteeg and Malalasekera, 2007, STAR-CCM+ user guide, 2014). Turbulence models provide extra transport equations to quantify μ_t. The $k - \varepsilon$ turbulence models are amongst the most common CFD approaches (Wang et al. 2017, Shih et al. 1995, Launder et al., 1974).

2.9 Gap in the Knowledge

There is an appealing interest for researchers to provide a real and practical insight into thermal performance and fluid flow characteristics of transpired solar collectors. A number of geometrical characteristics and climatic variables affect thermal efficiency; hence knowledge of their influence is essential for system optimisation. A considerable amount of research has been carried out regarding different aspects of TSCs. Whilst experimental research tends to be inherently expensive and not

sufficiently versatile to various sets of parametric studies, numerical study can be cost effective and flexible to accommodate different climatic and geometric conditions. In particular, Computational Fluid Dynamics (CFD) modelling potentially offers a realistic insight into the details of heat transfer and fluid flow within TSC systems. However numerical approaches to model TSCs are challenging because of the fluid flow and heat transfer mechanisms complexities and the respective computational requirements. The complexities that a practical TSC modelling faces can be summarised as:

- Various factors need to be taken into account including variable flow regimes and flow non-uniformities, jets through perforations, the development of complex boundary layer along the absorber plate, and various forms of heat transfer occur within TSCs. Models must also take into account variable atmospheric conditions existing at the external boundaries, and specific flow conditions at the interface between free stream air flow and solid surfaces. Interaction of both internal flow and external open-stream flow in a single control volume; boundary conditions and computational mesh should be designed and optimised in a way which supports the nature of these flows and satisfy the requirements of flow interaction taking place between the two regions.

- Existence of small-scale perforations over a relatively large-scale plate; the porosity of absorber plates widely range between 0.004 and 0.02, which indicates a high level of multi-scale geometry configuration. This configuration compels to create a grid with various mesh densities which facilitates fine mesh to capture the boundary layer and jet flow resulting in an extensive grid size and high computational capacity.

- As a consequence of the aforementioned complexities, a range of assumptions concerning the underlying physics, system sizes and geometries and boundary conditions have been established in the developed models in order to simplify the problem. Since these simplifications compromise the accuracy of numerical modelling, there is still an evident lack of comprehensive insight into the prediction of significant performance parameters by using a realistic generic method.

The present research attempts to adopt a more realistic, generic and cost-effective approach to develop a model that not only fills the methodological gaps in the literature, but also proposes a solution to the problem of huge computational gird size for multi-scale geometries. The proposed method is novel and significant also because it takes variable parameters into account that have not been considered due to

computational cost i.e. wind direction and solar load. In particular, solar load is taken into consideration in terms of radiation intensity and sun position in a very specific geographical location and time.

2.10 Concluding Remarks

The current state-of-the-art TSC has been reviewed and carefully examined in order to both use the helpful contents and address the existing gaps within the current knowledge. This has helped this study to provide an improved understanding of CFD simulation of TSCs and predicting methods of the systems' performance.

The main findings of this chapter include:

- The assumption of an asymptotic boundary layer (boundary layer with a fixed thickness) has been made by a number of researchers which simplifies the numerical analysis to a repetitive region with similar flow behaviour around the perforations (Gawlik and Kutscher, 2002; Collins and Abulkhair, 2014). This assumption however is assumed to be valid if uniform approaching flow together with a homogenous suction are in existence which is in reality in contradictory to airflows around and across TSCs.

- The relative effect of heat transfer on the back of the perforated plate (Q_b) has been treated differently within the literature. Q_b has been simply neglected in the studies by Cao et al (1993), Dymond and Kutscher (1997) and Arulanadam et al. (2000). Whereas it has been considered to contribute significantly to the overall heat transfer in the research by Gunnewiek et al. (1996), Van decker et al. (2001), and Chan et al. (2013).

- No-wind conditions, exclusion of the radiative heat transfer from the calculations, 2-D simulations, and fixed wind directions have been amongst other shortcomings found in the previous numerical modelling studies.

- Kutscher (1992) and Leon and Kumar (2007) did not find plate thickness to play an important role in determining the thermal performance of the collectors. Cao et al.(1993) and Van Decker et al (2001) however showed the heat transfer taking place within the perforations comprises a high percentage of the total heat transfer.

Chapter 3 Research Methodology

3.1 Introduction

This chapter presents the detailed methodology behind the construction of three-dimensional full-scale CFD models, developed to investigate flow and thermal behaviour of Cassette-Panel Transpired Solar Collectors (CP-TSC) (Figure 3-1). The CFD models are based on the geometry of a prototype system installed on the south-faced façade of a disused residential building at Oxford Brookes University (latitude 51.75°, longitude -1.13°). This trial site is one of the few large scale experimental facilities where TSCs have been studied at the necessary level of details.

This chapter includes:

- Description of the problem
- A presentation of the model TSC geometry
- Detailed explanation of the grid design and numerical approach
- Validation of the CFD result using the available experimental results
- Approaches used for geometrical optimisation

3.2 Problem Definition

TSCs are solar heating systems comprised of a micro-perforated steel sheet mounted on a building façade together with a ventilation fan drawing ambient outside air through the perforations (Figure 3-1). A cavity is created between the mounted steel sheet and the building wall. The micro-perforated steel sheet acts as a solar absorber plate which then transfers heat to the ambient air layer next to its surface. The heated air gains more heat as it passes through the perforations and streams along the back surface of the absorber plate within the cavity traveling towards the ventilation fan. The heated air is then ducted into a building as warm air supply.

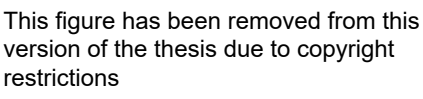
This figure has been removed from this
version of the thesis due to copyright
restrictions

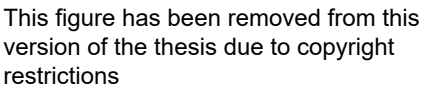

Figure 3-1.(a) Building façade with the installed cassette-panels (the four panels directly between the windows shown by arrows), (b) Conceptual illustration of a Cassette Panel-TSC solar air-heating system (Hall et al., 2014).

Whilst the system operation seems to be relatively simple, interaction of different types of flow and heat transfer taking place around, a cross, and inside TSC, together with relatively small perforations on the absorber plate, inherently create a complex problem of fluid mechanics to be modelled (Figure 3-2).

Heat exchange between the system and the air takes place in three stages at the front surface of the plate, through the perforations and at the back surface of the perforated plate. The absorber collects the solar radiation and heats up a thin adjacent layer of the air flowing over the plate through convective heat transfer ($Q_{conv,air-abs}$). The flowing air is a free stream flow (wind flow), referred to as external flow in fluid mechanics. Buildings act like bluff bodies immersed within this external flow which is categorised as Atmospheric Boundary Layer (ABL). The atmospheric boundary layer is the lowest layer of the atmosphere that is affected by the earth surface. Due to the blowing wind, together with thermal layers associated with solar radiation, re-circulations and re-attachments take place at the lowest level of the atmosphere which causes the ABL to be turbulent. Long-wave radiation emitting back from the surface of

the absorber to the surrounding ambient is taken as radiative heat loss ($Q_{\text{loss r,abs-amb}}$). Moreover wind takes away a portion of the heated layer of air alongside the perforated plate which is counted as the system's convective heat loss ($Q_{\text{loss c,air-abs}}$) .

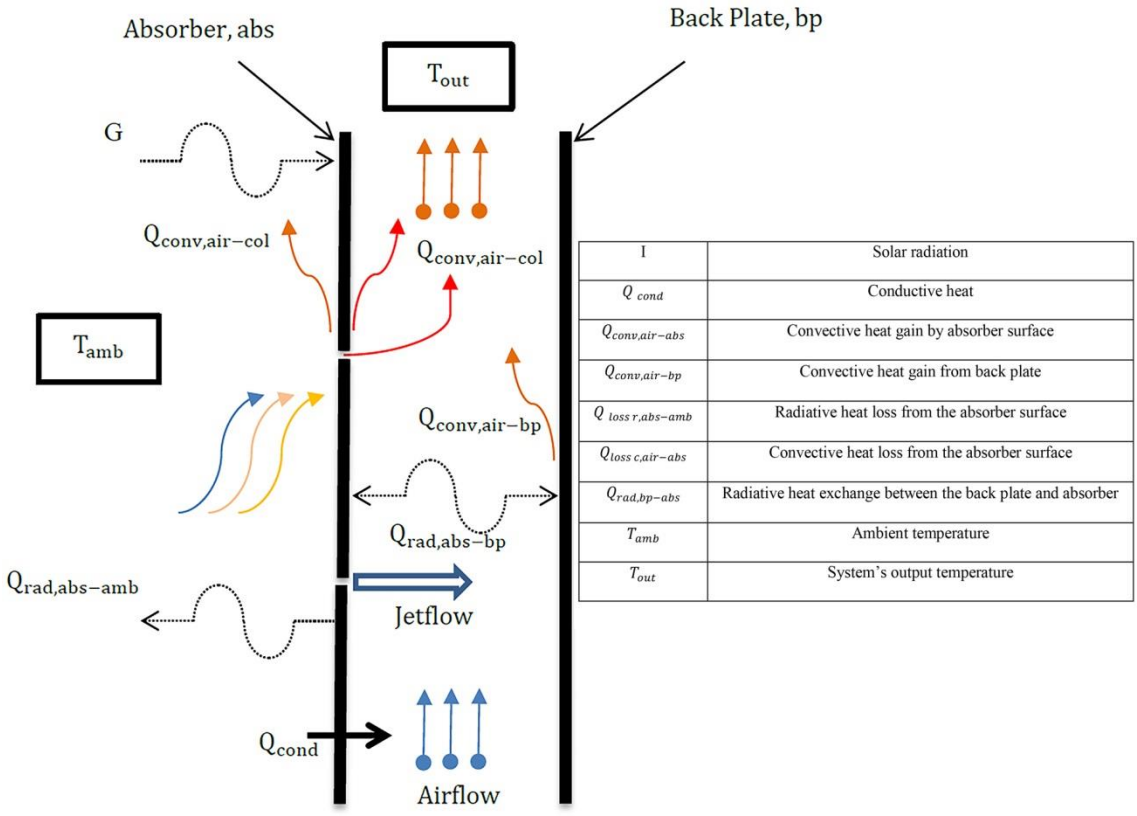

I	Solar radiation
Q_{cond}	Conductive heat
$Q_{conv,air-abs}$	Convective heat gain by absorber surface
$Q_{conv,air-bp}$	Convective heat gain from back plate
$Q_{loss\ r,abs-amb}$	Radiative heat loss from the absorber surface
$Q_{loss\ c,air-abs}$	Convective heat loss from the absorber surface
$Q_{rad,bp-abs}$	Radiative heat exchange between the back plate and absorber
T_{amb}	Ambient temperature
T_{out}	System's output temperature

Figure 3-2. Schematic thermal and airflow fields in TSCs.

Heat exchange continues to second stage within the perforations as the air is being sucked into the cavity between the plate and the building façade (plenum). Due to relatively small size of the perforations, the heated air is sucked into the plenum with relatively high velocity (jet flow) through the perforations compared to the velocity of airflow in the plenum which creates recirculation and is assumed to be turbulent (Lie et al., 2013; Badache et al., 2013). It is expected that as the temperature of the air rises less heat exchange will take place between the absorber and the air due to a decreasing temperature gradient between the two media. The collected solar energy however is conducted through the metal absorber (Q_{cond}) to the other side facing the plenum so the heat exchange between the air and the absorber reaches to the third stage occurring within the plenum. Radiative and convective heat transfer will also take place within the plenum, between a) the back surface of the plenum and the absorber ($Q_{\text{rad,abs-bp}}$) ; b) the back surface of the plenum and the airflow travelling towards the outlet

hole ($Q_{conv,air-bp}$), respectively. The jet flow which impinges into the laminar internal flow causes recirculation and develops turbulent flow streaming in the cavity towards the outlet hole. The existence of very small circular perforations (diameter 1.5×10^{-3} m) over a relatively large surface area (2.73 m ×1.74 m) resulted in a multi-scale geometry. Multi-scale geometries necessitate an appropriate multi-scale computational grid which can prove costly with the increased number of cells. An initial estimation showed a grid size with 100M cells for the current prototype. The bigger the difference between the scales, the larger the cell count of the grid size will be; thus high computational capability is essential in order to solve the governing equations over a high number of cells in the grid. Moreover, the presence of external, internal and jet flows, together with the transition between laminar and turbulent flow demands high computational capability to capture the inherent dynamic behaviour.

The methods employed in order to develop a suitable and accurate model to replicate the actual fluid flow and thermal behaviour of the system is explained in this section.

The governing equations were solved numerically with the specified boundary conditions using the STAR-CCM+ software package (STAR-CCM+ 9.04. 2014). The numerical model was generated through the steps summarised in Figure 3-3.

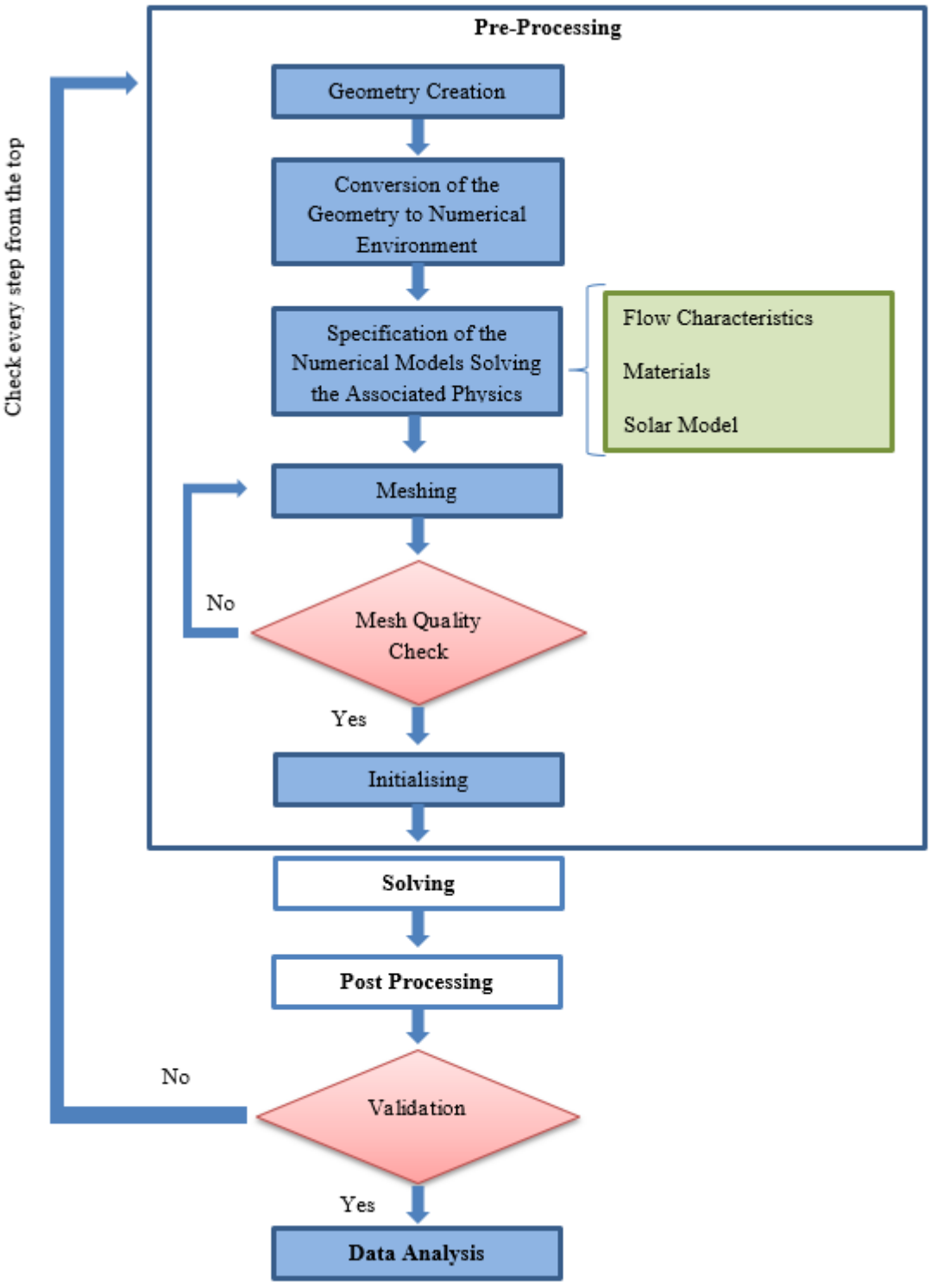

Figure β-3. Flowchart of the steps taken to develop the CFD model.

3.3 Brief Description of the Experimental Work

The experimental work was part of the ROBUST[1] project which is published in Hall et al. (2014). For the purpose of the current study, it is important to identify how the data were collected during the experimental work. A brief description of the data measurement is presented in this section.

Solar radiation intensity was measured using a Kipp and Sonnen solar pycnometer mounted on the panels in the vertical plane recording the vertical solar radiation intensity (Figure 3-4)

Figure ß-4. Position of the solar pycnometer recording solar radiation intensity.

The air mass flow rate streaming into the building was measured inside the ducting that delivers the heated air into the building by a device using a pitot tube mounted in the air stream (Figure 3-5).

Figure ß-5. Mass flow meter device at the outlet of the TSC system

A DeltaT Devices WS-GP1 weather station was installed adjacent to the TSC systems recording the weather condition i.e. the ambient air temperature and humidity, wind speed and wind direction

[1] See http://www.steel-renovation.org/ for more information about the ROBUST project and in particular work packages 1.6 and 1.7

(Figure 3-6). The configuration of the sensors used to record the temperature of the streaming air though the system and the absorber plate can also be seen in Figure 3-6. For the purpose of the model validation in this study (described in 3.9–3.9), the absorber surface temperature is taken as the average temperature recorded at A1 and A2 whilst the outlet air temperature are taken from the C point.

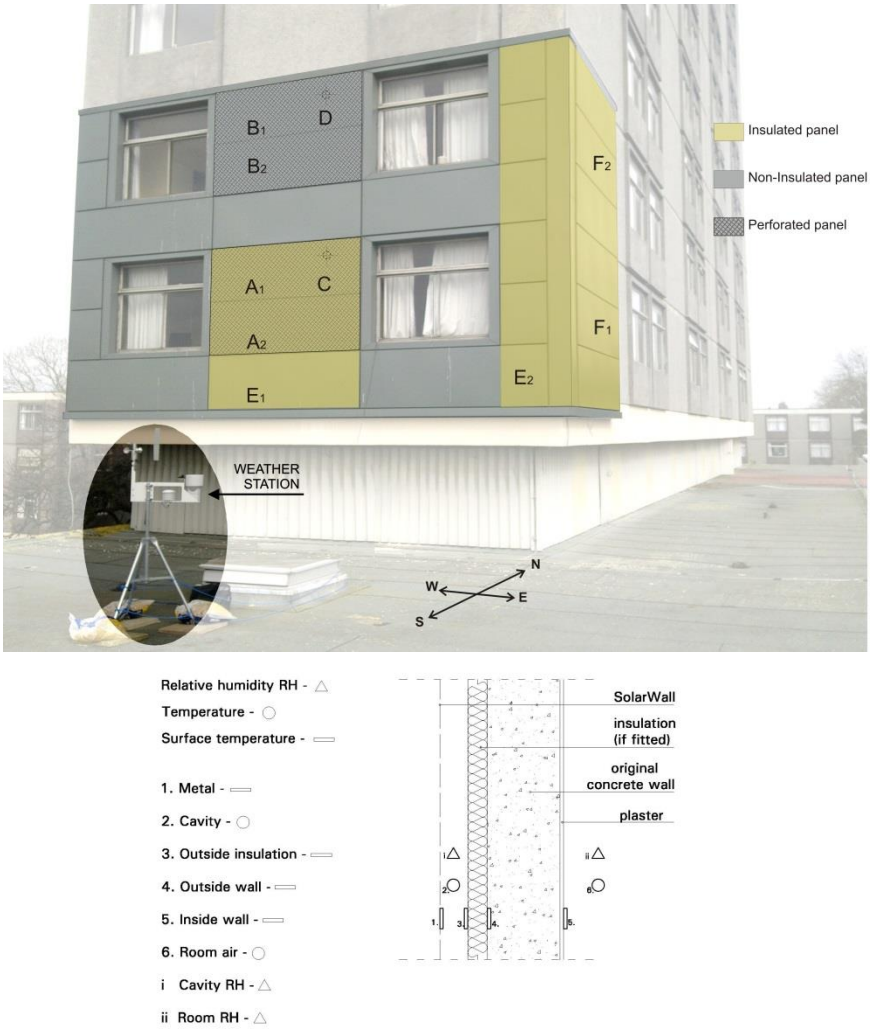

Figure 3-6. Location of the weather station and the sensors across the system.

It is important to note that the wind flow measurement around the building may be slightly different from the mainstream wind flow in the further field from the building.

Figure 3-7 shows one of the TSC cassette installed and tested at Oxford Brookes University (Hall et al. 2014). The panels are coated with Corus Colorcoat Celestia® which is a type of PVC based coating and Merlin Grey in colour. The absorptivity of the coating is 0.86 which could be classified as 'High' in the SBEM TSC colour classification (iSBEM user guide, 2013). The tested TSC comprised two cassette-panels with the dimensions of 2730 mm×870 mm; however the developed CFD model comprises a full-size vertical section of the system with the square layout of circular perforations (1.5 mm diameter and

20 mm pitch distance) on the absorber plate (Figure 3-8, Figure 3-9). Due to the existence of very small perforations on the relatively large plate, full size TSC modelling would require prohibitive computational costs. The developed model configuration, together with the employed numerical approaches, is capable of capturing the most important phenomena taking place in TSCs, such as the local pressure gradient in the vertical direction, arising from the fan.

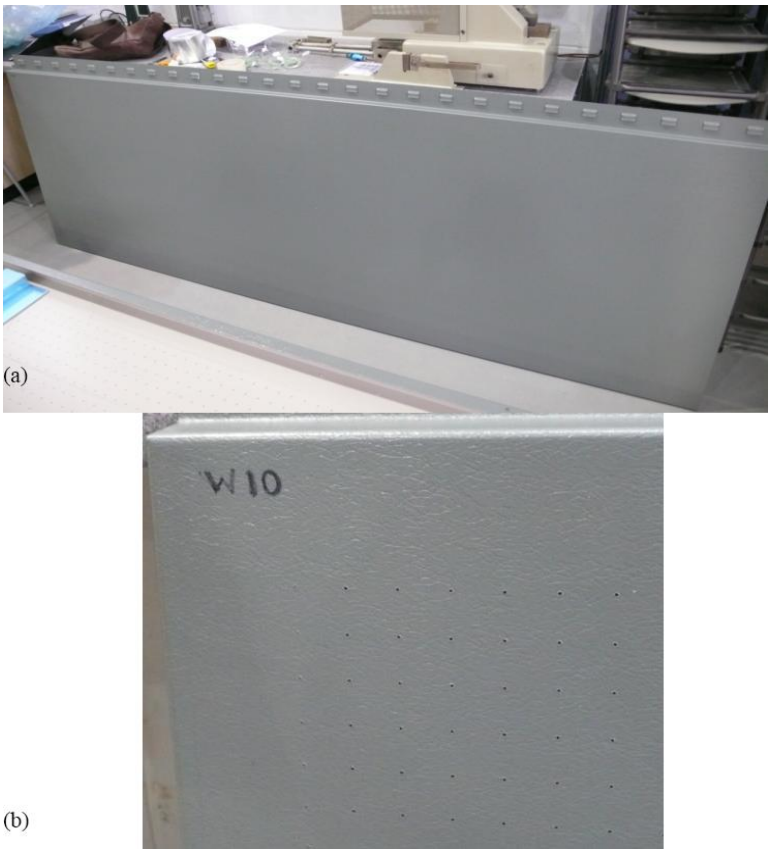

Figure 3-7. The cassette panel: a) whole panel; b) close up of perforations.

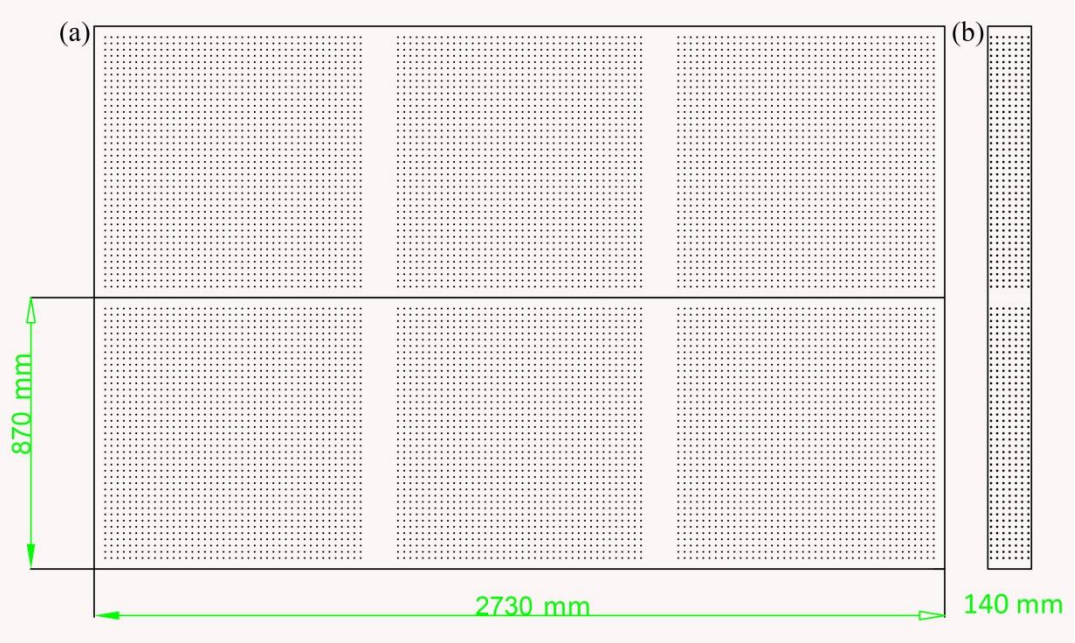

Figure 3-8. CAD drawing of a) the trialled double cassette panel b) the modelled portion of the cassette panel.

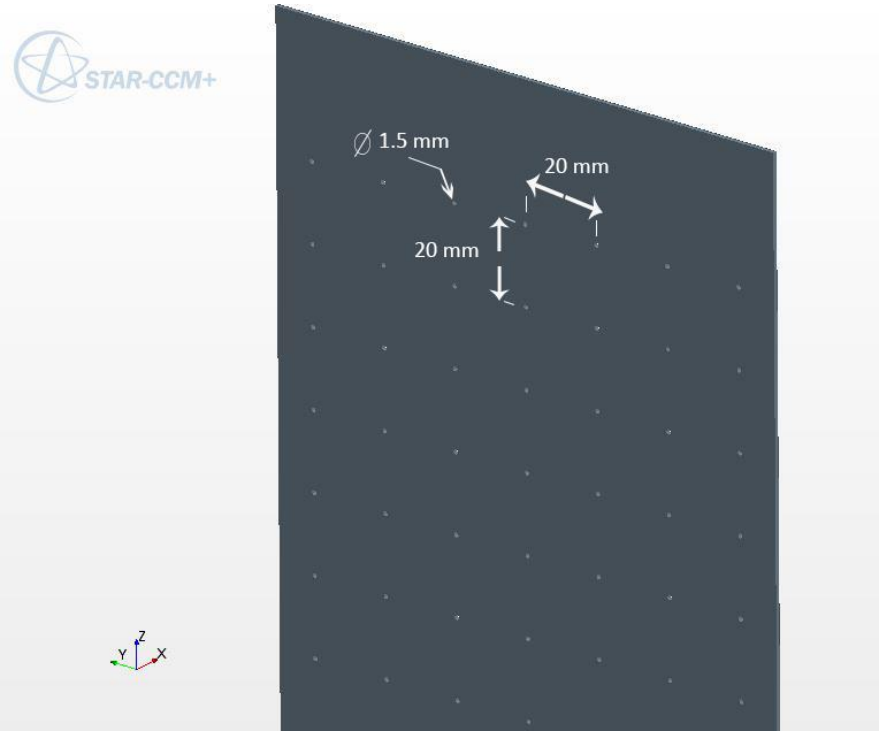

Figure 3-9. Section of the modelled TSC in STAR-CCM+.

Further details about the computational domain, grid design, simulation of external airflow (ambient air) and internal/jet flows are presented in the following sections.

3.4 Grid Design

The approach of CFD is to divide the flow domain into a number of smaller discrete subdomains. These subdomains are known as grid cells and a collection of them that lie next to each other covering the whole domain is referred as 'mesh'. Thus, mesh is the discretised representation of the computational domain, over which the associated physics governing equations are solved for each cell. The size of the cells should suit the changes taking place across the flow within the local context. STAR-CCM+ provides a mesh generator that can be used to produce high quality mesh for various geometries and applications. There are two universal forms of mesh design categorised as structured and unstructured (Figure 3-10).

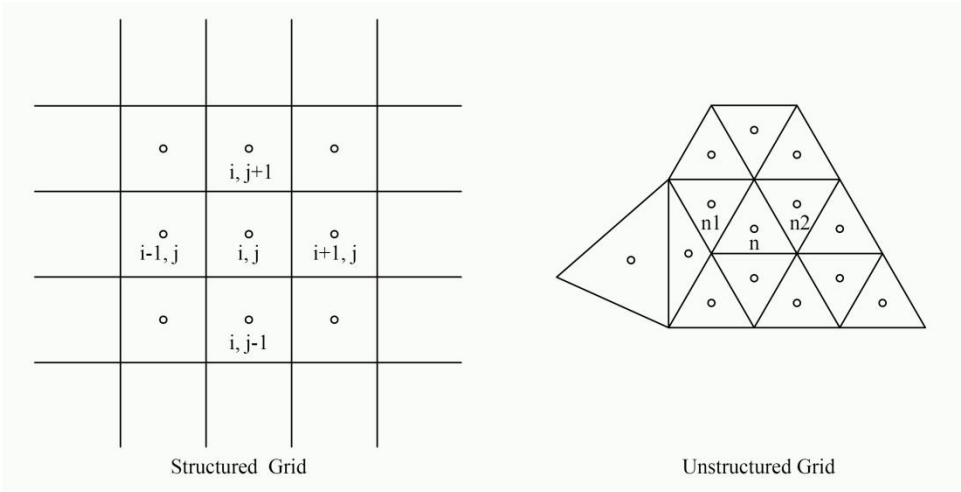

Figure 3-10. Mesh arrangement in 2D.

Advantages of structured grid over unstructured can be summarised as follows (Pointwise software, 2013; Mavriplis, D.J., 1996):

- Time and memory: A desired geometry can be covered with fewer hexahedrals than tetrahedrals, thereby reducing the amount of cells, computation time and memory usage.
- Resolution: Fluid Flow often doesn't behave in an isotropic way. Flows are expected to feature dominant variable gradients in a specific direction with milder gradients in other directions (e.g. boundary layers, shear layers, wakes). Hexahedral cells with high aspect ratio can be used in these cases to lower the cell count. Inversely, highly stretched tetrahedral grid doesn't produce accurate CFD results. Moreover, uniformly stretched tetrahedral cells are difficult to generate.

- Alignment: CFD solutions show better convergence and more accurate results when the grid is refined along with the predominant flow direction. Since the grid lines follow the boundaries of the geometry, alignment can simply be attained for structured mesh whereas there is no such alignment in an unstructured mesh.

The existence of very small circular perforations (diameter 1.5 mm) over a relatively large surface area (2730 mm×1740 mm) results in a multi-scale geometry. Although structured grids have clear advantages over unstructured ones, other issues must be considered in the context of complex geometries. Structured grids are difficult and time consuming to generate; they may also feature an unnecessarily high grid resolution and undesirable aspect ratios. Therefore a multi-block and structured grid is a convenient alternative that subdivides the domain into regions of interest facilitating more control over grid refinement at necessary zones (e.g. near wall zones) and appropriate mesh aspect ratios. Moreover, the STAR-CCM+ mesh generator offers a body-fitted grid function, which is considered as a method of dealing with complex geometries. Fundamentally, a body-fitted mesh is based on a structured curvilinear grid that fits into and/or around the physical domain (Figure 3-11). This grid is then mapped onto the computational domain with a simple Cartesian grid for computational purposes.

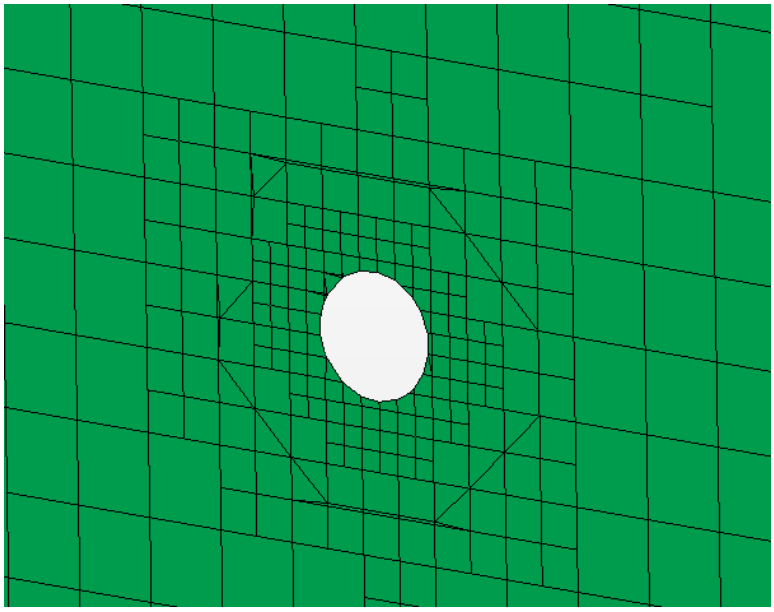

Figure 3-11. Body-fitted mesh around a circular perforation; current study.

In order to capture the relevant airflow behaviour, including the boundary layers and the jets emerging from the perforations into the plenum, a multi-scale, locally-refined, block-structured, body-fitted, hexahedral grid was generated using the 'Conformal Trimmer' meshing approach (STAR-CCM+

user guide, 2014). The Conformal Trimmer is a method to generate a structured grid in STAR-CCM+. Figure 3-12 shows the generated grid within the physical domain.

The typical cell size was of the order of 0.2 mm around and within the perforations and 10 mm away from the absorber plate (Figure 3-13). As can be seen, multi-block mesh generation has been also employed to gradually fill in the gaps between the very fine regions and the course ones. This method helps the model with both reducing the cell count and creating a transition between the very extreme sized regions rather than imposing a sudden huge change to the grid. Sudden changes in the grid mesh cause the solution to be unstable. The characteristics of the jet flows were captured by creating refined conical grid regions adjacent to each single perforation, as shown in Figure 3-13. Conical shapes of mesh refinement have been implemented in order to capture the jet impingement originating from the perforations. The flow in the region adjacent to the walls was resolved using 'Two-Layer All y+ Wall Treatment' wall function (STAR-CCM+ user guide, 2014). y+ is a non-dimensional distance from a solid interface implying where a cell is located within the boundary layer which subsequently dictates how fine a mesh should be for a particular fluid flow around a solid surface. This method helps the model to avoid extremely fine mesh near the wall whilst being flexible to resolve both high and low Reynolds flow types. This Wall Treatment is developed to capture both low and high y+ treatments while maintaining results accuracy in cases with 5 < wall y+ < 30 indicating the first cell layer is located within the buffer layer (Versteeg and Malalasekera, 2007; STAR-CCM+ user guide, 2014).

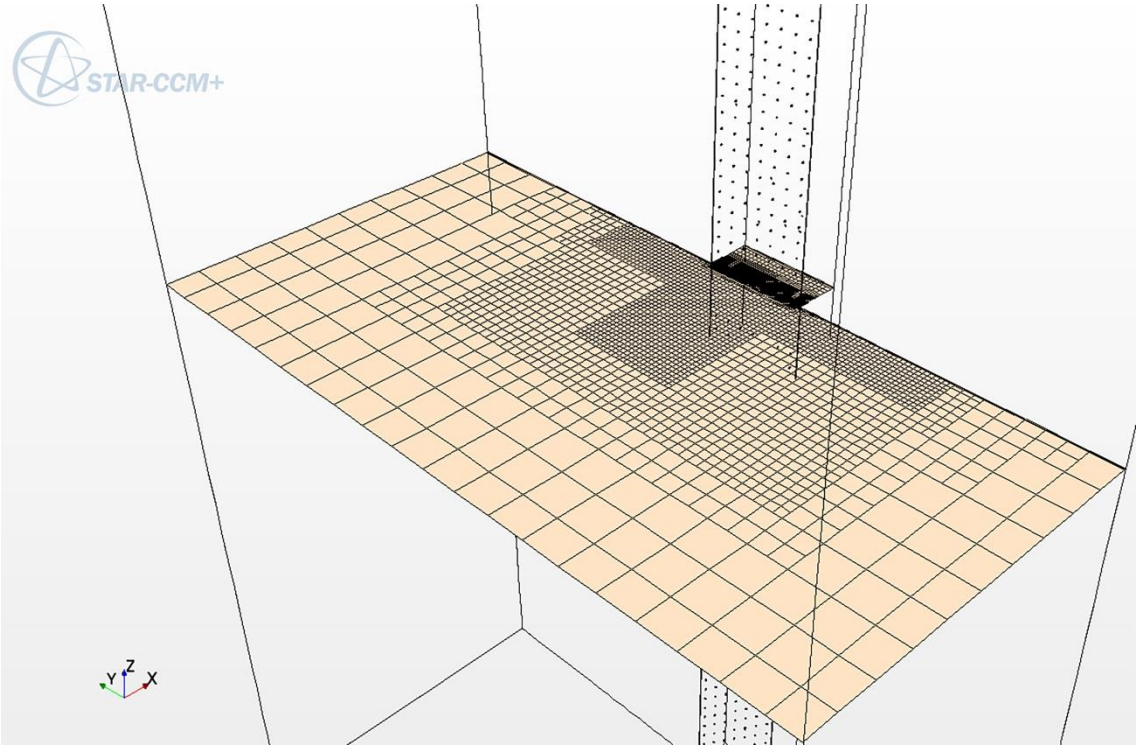

Figure ꞵ-12. A cut through view of the full domain grid design.

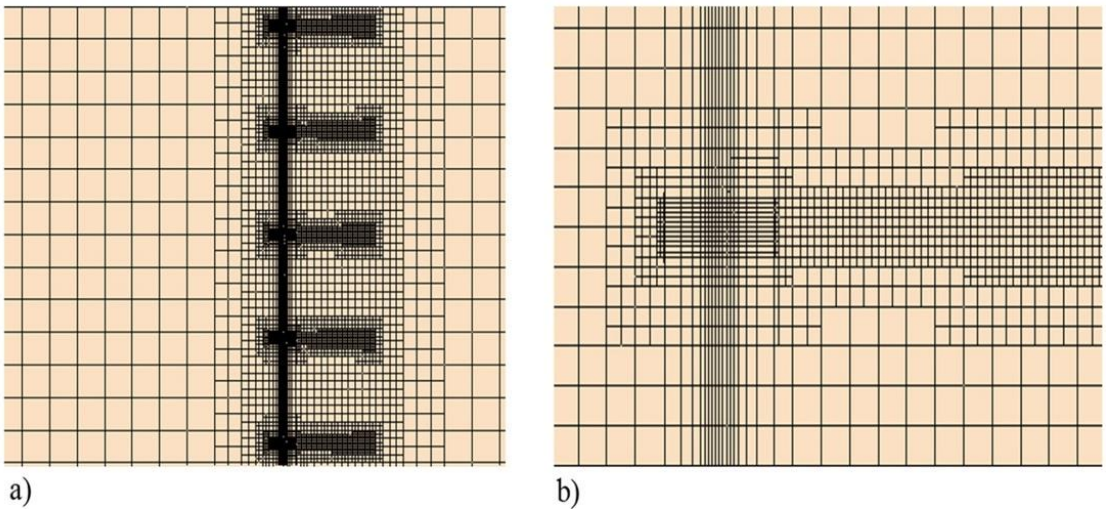

Figure ꞵ-13. Hexahedral Mesh created around the plate and in the free-stream region; b) Details of the conical grid scheme to capture the jet flow

3.5 Numerical Approach

The commercial CFD software, STAR-CCM+ has been used to solve steady-state, three-dimensional Reynolds Averaged Navier-Stokes (RANS) equations with the Realizable $k-\varepsilon$ turbulence closure model over the computational domain. A segregated flow solver has been adopted to solve flow and energy equations using a second order upwind discretization scheme, along with SIMPLE algorithm for pressure-velocity coupling.

Amongst the various numerical methods to calculate turbulent flow problems, the RANS approach has been demonstrated to deliver less detailed but widely-acceptable results for most engineering applications (Versteeg and Malalasekera, 2007). They are comparatively less expensive and require less computational resources. RANS models are based on time averaged equations and use auxiliary closure equations to calculate turbulent properties. These models are categorised into Zero, One, Two and Seven equation models. Realizable k − ε is one of the two-equation RANS models, which provides the closure equations in terms of transported scalars k, the turbulent kinetic energy, and epsilon (ε) the rate of kinetic energy dissipation. This turbulence model is widely used to predict flows containing planar and round jet flows, rotation and recirculation, as well as boundary layers under strong adverse pressure gradients or separation. Davis et al. (2012) carried out a comparative analysis of three different RANS-based turbulence models using STAR-CCM+. The results indicate that Realizable k − ε is more suited to

resolve recirculation region, stream wise wakes, and counter-rotating regions. The segregated solver is ideally suited for incompressible and weakly compressible flows, with the Mach number below 0.3. The SIMPLE algorithm is adopted in this study for pressure-velocity coupling, as it is generally recommended to provide accurate results and robust convergence with fewer computational operations for steady state problems (Versteeg and Malalasekera, 2007; STAR CCM+ user guide, 2014, Fan et al., 2007), when compared to its extension PISO.

Finally, a second-order upwind scheme has been used as the most reliable, robust and stable discretisation scheme amongst the ones broadly used in CFD for complex fluid dynamics problems including TSC modelling (Versteeg and Malalasekera, 2007, Lie et al, 2013; Fan et al., 2007; Khaboshan et al., 2018; Warmin et al., 1976).

The simulations included all modes of sensible heat transfer with specified values of emissivity, absorptivity and thermal conductivity on all relevant surfaces. Sun position was set as a function of the local time zone using the Solar Load sub-model; the vertical solar radiation data recorded by the façade mounted pyrometer (Hall et al., 2014) was applied to the model. The location and orientation of the sun are defined by the Azimuth and Altitude angles which are the function of time and geographical location.

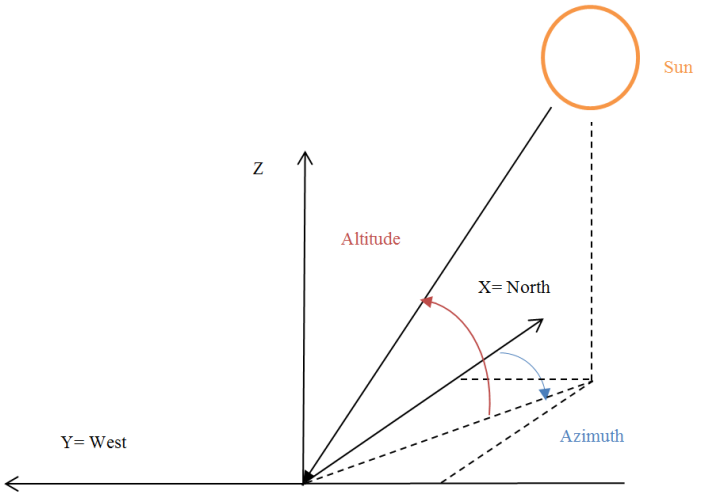

Figure 3-14. Solar model coordinate system (STAR-CCM+ 9.04. 2014)

The Azimuth and Altitude angles of the sun have been calculated by the software database on the basis of the given location of the trial TSC ((latitude 51.75°, longitude -1.13°) and the time (site between 22nd December 2011 to 4th January 2012). The solar model is based on the surface to surface radiation model which employs ray tracing method in order to replicate the radiation between the sun and the TSC. The solar load model uses the surface to surface radiation that allows for radiative heat transfer between surfaces of arbitrary complexities. The spectral distribution of the solar emissions is assumed to be

represented with a blackbody at the average surface temperature of the sun and radiative absorptivity equal to unity (STAR-CCM+ 9.04. 2014). The amount of radiative heat transfer between the sun and the boundary condition is defined uniquely according to the radiative properties of each boundary condition i.e. transmissivity, reflectivity and absorptivity.

Solution residuals together with temperature and velocity at critical zones of the system were monitored to ensure convergence. Solution is deemed to be converged if:

1) Surface integrated velocity at the perforations exit is constant, or changes less than 1.0e-4, in 50 consecutive iterations.
2) Surface integrated temperature of the absorber plate is constant, or changes less than 1.0e-4, in 50 consecutive iterations.
3) The system imbalance for mass flow rate across the volume control is less than 1%.
4) The RMS residuals are less than 10^{-3}.

3.6 General Model Setup and Boundary Conditions

The CFD model is based on a prototype cassette-panel TSC and comprises a full-size vertical section (*z* direction Figure 3-15) of the system with circular perforations (pitch 20 mm) in the absorber plate. This configuration of the computational domain captures the local pressure gradient in the vertical (z direction) and normal direction (x direction), arising from the fan (Tajdaran et al., 2016).

As shown in Figure 3-15, the computational domain comprises of four main regions, each with specific boundary conditions. The regions are named as Ambient (fluid), Absorber Plate (solid), Perforations (fluid), and Plenum (fluid) region. Two physics continua regions have been created comprising a fluid and a solid material. The air continuum has been applied to the Ambient, Perforations and Plenum regions, whereas the perforated plate has been set as carbon steel continuum. Each physics continuum contains the solutions models, material properties, reference values, and initial conditions summarised in Table 3-1.

The airflow travels the fluid regions in the following way:

a) Main stream is in x and z direction within the Plenum.
b) Main stream along the perforations' axis in the Perforations region.
c) Main stream mainly in the x-y plane in the Ambient region.

Although an ideal model would account for the full geometry together with the associated physics, a range of assumptions have been taken in the present work to minimise the size of the modelled domain, and hence the computational cost.

Fan power is the main drive force in the plenum which makes the streamflow in the plenum dominantly to fit in $x - z$ plane as: a) vertical flow towards the top side of the plenum where the fan produces negative pressure and b) normal flow through the perforations and jet impingement into the plenum main stream. The normal flow strikes the main stream traveling upwards with a relatively high velocity into which it then dissipates.

According to Bernoulli equation, the pressure drop is the result of buoyancy and the acceleration pressure loss:

$$\Delta p = (\rho_2 h_2 - \rho_1 h_1) g + \frac{1}{2}(V_2^2 - V_1^2) \quad (3\text{-}1)$$

where h is the height level and V is the velocity of the flow at the associated height level. This suggests that suction velocity across the perforations at the same level of h is almost similar, but different at various h levels. Thus the flow has been modelled in full scale in the z direction (h) to capture all the flow variable gradients.

Table ꞵ-1. Summary of the CFD model setup.

Properties		**Ambient**		**Perforations**	**Plenum**			**Absorber Plate**	
		Extended wall	Other surfaces	perimeter	Bottom	Rear	Other surfaces	Front	Back
Absorptivity		0.86	0	0.86	0.66	0.2	0	0.86	0.8
Emissivity		0.89	0	0.89	0.66	0.2	0	0.89	0.8
Reflectivity		0.14	0	0.14	0.34	0.8	0	0.14	0.2
Dimension ($\boldsymbol{mm \times mm \times mm}$)		980x490x1740		1.5	140x60x1740			140x1.2x1740	
Material		Air						Carbon Steel	
Thermal conductivity ($\boldsymbol{W/mK}$)		0.026						57	
Specific heat capacity ($\boldsymbol{J/kgK}$)		1006.2						434	
Initial condition	Temperature (^{o}C)	19						23	
	Velocity components (m/s)	(1e-5, -0.5, 1e-5)						N/A	
Reference Pressure ($\boldsymbol{Pa}$)		101325						N/A	
Flow type		Steady							
Turbulence model		RANS ; Realizable $k-\varepsilon$							
Discretisation scheme		2nd order upwind							
Velocity-Pressure coupling scheme		SIMPLE							
Energy model		Segregated							

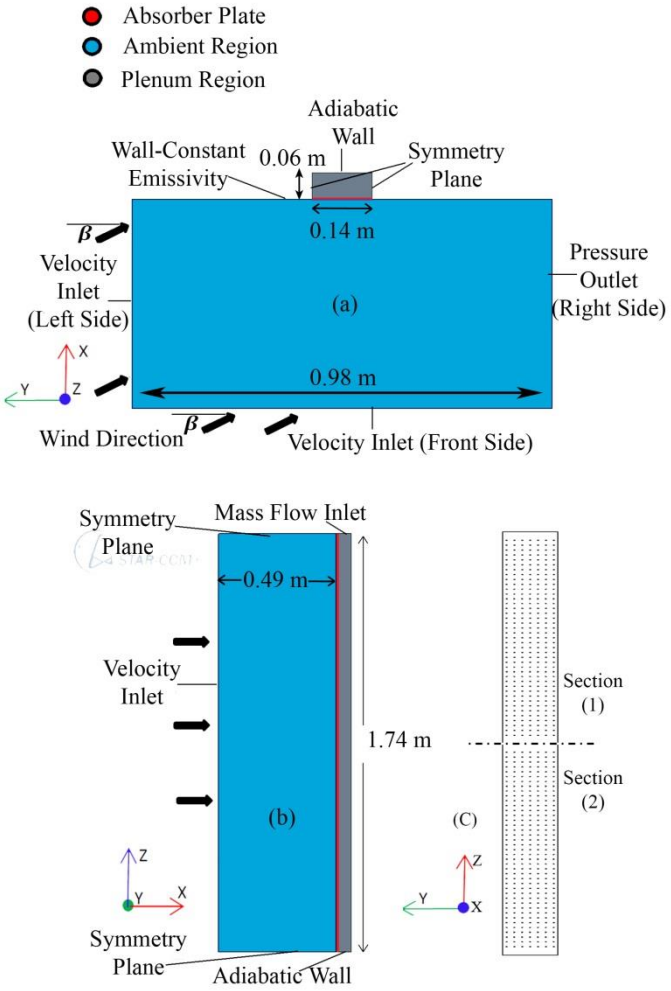

Figure 3-15. Computational domain and model configuration; (a) Top view, (b) Side view, (c) Sketch of the absorber plate.

The airflow within the perforations is approximately one dimensional (normal flow) connecting ambient and plenum region. Since the plate thickness is relatively small, the airflow parameters around the ambient-perforations interface are directly dependent on the suction velocity originating from the fan power in the plenum. Suction velocity calculation at the associated height level of a perforation is simulated in the plenum region considering all the corresponding complexities and flow features. As discussed before, the interaction between the internal flow and external flow through the perforations demands a high computational capacity. Here, an assumption has been implemented to reduce the computational cost. Since the practical levels of suction ratio (V_s/U_∞) are very low (less than 0.01), the layer of air around the perforations being dragged into the plenum is assumed to be significantly thinner than the entire length of the collector in y direction, i.e. $dx/dy \rightarrow 0$. Therefore, following Kutscher's assumption (1992), the gradients of flow parameters in the y direction are assumed to be less intense than those in the x direction:

$$lim \frac{dM/dy}{dM/dx} \to 0 \qquad (3\text{-}2)$$

This approach is employed to reduce the size of the computational domain in the y direction which is found to have less impact on the accuracy of the results. The above theory has also been supported by creating extended surfaces either side of the perforated plate to ensure $\to \infty$. The model geometry and associated boundary conditions are given in Figure 3-15. The illustrated geometry is a two-panel collector with an area of 140 mm ×870 mm per panel. Each panel has a pitch distance of 20 mm and the diameter of each perforation is 1.5 mm.

The experimental TSC system is installed on the south façade of the building. Due to a directionality requirement in terms of sun orientation within the Star-CCM+ software package, the model is positioned in a way to face south direction; the X-axis is aligned with the local magnetic north direction and the Y-axis is aligned with the local west direction.

The following sections outline the specifics of the setup, boundary conditions, and assumptions taken in the definition of each region.

3.6.1 Ambient region

The approaching external flow (wind) has been simulated using a 'velocity inlet' boundary condition at the left side of the ambient region, with a specified wind angle (β), wind speed (U_∞), and static temperature. These boundaries have been described to be 100% transparent (neither absorbed nor reflected), together with a typical value of 1% for turbulence intensity (Versteeg and Malalasekera, 2007). Static temperature of the blowing airflow is the constant value that has been considered as ambient temperature.

The same condition has been set for the front side of the ambient region. This boundary is located far enough from the surface of the perforated plate to not influence the boundary layer development. Nevertheless, an iterative process has been used to shorten this distance, minimising the grid size but maintaining the flow characteristics unchanged.

The right side of the domain was set as 'pressure outlet' using a zero gauge pressure condition. Surface transmissivity has been set to be 1.0 along with the desired level of ambient temperature. Turbulence viscosity ratio field function together with turbulence intensity of 1% has been considered to

model the turbulence properties of the outlet boundary. Since there is no data available of the turbulent viscosity ratio, the associated field function calculates turbulence viscosity rather than having it fixed at the boundary.

The top and bottom sides of the ambient were defined as symmetry planes, enforcing planar wind simulation. Although it would be more realistic to account for a three dimensional turbulent airflow as was demonstrated in Fleck et al. (2002), the assumption of 2-D wind has been imposed which is consistent with the available experimental data on the wind properties in the z-direction. Moreover as the system is mounted at the first floor of a high rise building, it has been shown in the literature that the air flow mostly stream in a 2-D manner parallel to the façade (Mu et al., 2016; ASHRAE, 2015) which is considered to be a reasonable compromise to decrease the size of the CFD model. TSCs modelling at different part of high rise buildings together with the airflow complexity can be the subject of further investigation.

3.6.2 Absorber plate region

The absorber plate was defined as a solid region with specified values of absorptivity and emissivity, comprising four side walls, two interfaces with the ambient and plenum region, and an interface with the perforations region. In STAR-CCM+, contact interfaces join solid and fluid regions, permitting conjugate heat transfer between the two entities. The side walls have been set using a temperature field function, which calculates the temperature based on thermal conductivity of the material, radiation properties and the interaction with the surrounding regions.

Based on conservation of energy on radiative heat transfer by real surfaces, the incident radiation on an arbitrary surface may be reflected, absorbed, or transmitted. This can be expressed as:

$$\rho + \beta + \tau = 1 \qquad (3\text{-}3)$$

where, ρ, β and τ are reflectivity, absorptivity and transmissivity of the surface, respectively.

According to Kirchhoff's law (Incropera, 2011), the directional spectral emissivity is equal to the spectral directional absorptivity. This means that if an object is able to radiate and receive radiation at similar wavelength and angularity, then the amount of radiative energy absorbed is equal to the amount of that radiated.

On the basis of the real geometry and the coating of the absorber plate, the radiation properties of the front surface that is exposed to ambient are set as: $\varepsilon = 0.89$, $\beta = 0.86$, $\rho = 0.14$, and $\tau = 0$. For the Plastisol, medium grey-coated back surface of the plate, the properties are set as: $\varepsilon = \beta = 0.8$, $\rho = 0.2$,

and $\tau = 0$. Different emissivity and absorptivity values are believed to be due to the reaction of coating within infrared wavelength range. General information by the manufacturer does not specifically explain how these two values can be different. Whilst the plate is able to absorb energy at full wavelength range with $\beta = 0.86$, it however irradiates the long electromagnetic waves with $\varepsilon = 0.89$. Whilst there is an opportunity to develop coatings with lower emissivity values for solar heating systems, the ability to produce a model to replicate different emissivity-absorptivity within different electromagnetic bands is crucial for TSCs. Subsequently, two different wavelength ranges have been defined to accommodate two different values for absorptivity and emissivity for the solid part of our model. This technique would be helpful for design and development of ongoing research topics on low-emissivity TSCs (Hall et al., 2016).

3.6.3 Plenum region

The plenum region has been modelled in its full size, facilitating the simulation of a realistic bulk flow streaming towards the outlet. The top side of the plenum is defined as 'mass flow inlet' with a negative value of mass flow rate (flow going out) to represent the fan drawing air through the perforations and into the building. The rear side of the plenum was covered with a reflective-coated insulation material. This boundary was set as an adiabatic wall, with the radiative properties of $\varepsilon = \beta = 0.2$, $\rho = 0.8$, and $\tau = 0$. The bottom side of the plenum domain is made of aged galvanised steel on which the plate is installed. This boundary is also insulated, thus was also defined as an adiabatic wall, with radiative properties of $\varepsilon = \beta = 0.66$, $\rho = 0.34$, and $\tau = 0$. Right and left side of the plenum were set as symmetry planes to secure a zero flux of all quantities across these two sides.

3.6.4 Perforations region

The perforations region is basically filling the gap between three other regions. Subsequently, all the boundaries are forced to be either contact or internal interfaces. An internal interface joins two regions within the same continuum, which in this case correspond to the plenum and the ambient regions. The heat exchange between this fluid region and the absorber is modelled by a contact interface permitting conjugate heat transfer between the two entities. The non-slip shear stress condition, radiation properties of $\varepsilon = 0.89$, $\beta = 0.86$, $\rho = 0.14$, and $\tau = 0$, and smooth wall surface condition have been used for the contact interface boundary of this region.

3.7 Grid Independence Test

Accuracy, computational time, and cost are three main factors that need to be considered in CFD modelling. The best CFD model will satisfy all three parameters depending on the available computational power and accuracy demand of the specific application. A grid independence test was carried out to investigate the impact of grid resolution on the results, with a view to maximising the speed of solution convergence.

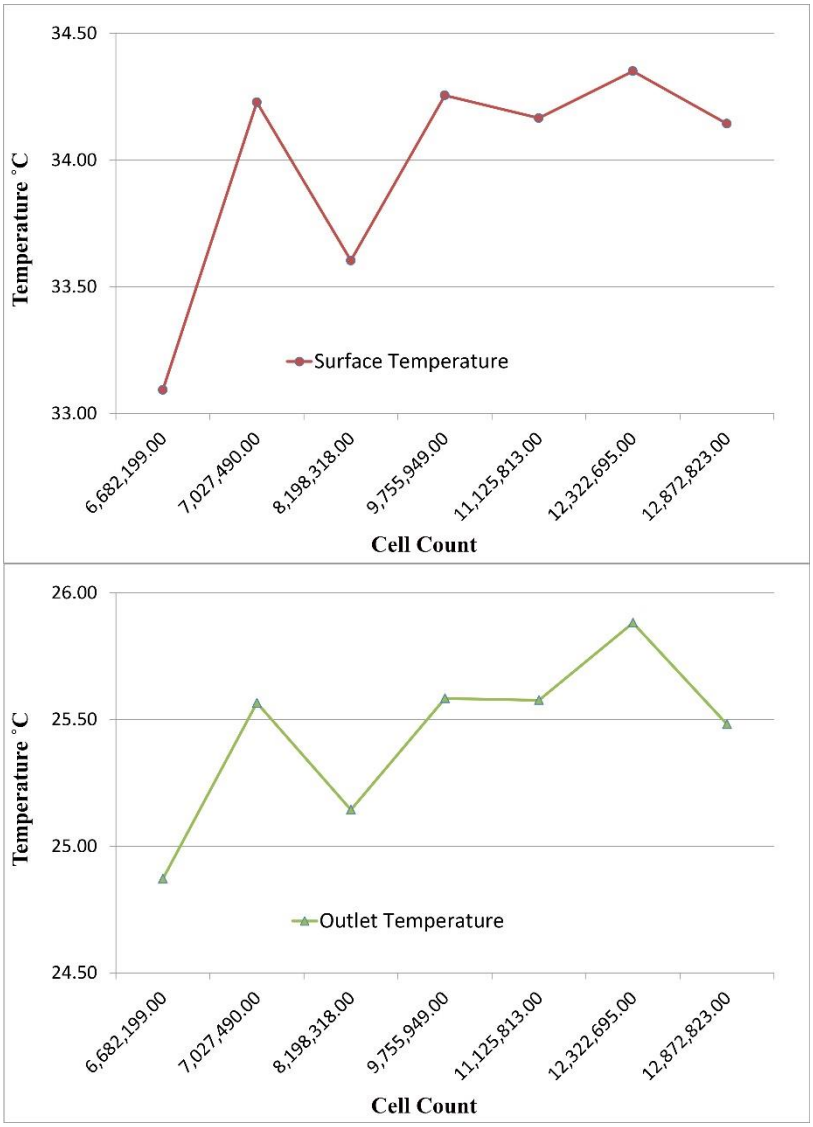

Figure 3-16. Grid independency tests presented in terms of a) surface temperature and b) outlet temperature.

For this purpose, seven different grids were generated. The general rule was to increase the cell base-size and the subsequent finer zones by 10% across the model to generate a new grid, carry out the simulations and monitor selected convergence parameters, specifically for surface and outlet temperatures, see Figure 3-16. The best grid ensuring acceptable accuracy and minimum cell count was

identified as the first grid size at which the convergence criteria would change within 1% of the following larger grid size. This approach was satisfied with a grid size of 9.7 M cells and base-size of 5cm referencing to the coarse zone. Using this optimized grid, each steady-state simulation reached convergence in approximately 11 hours of CPU time, running on a full 16-core node, within the local High Performance Computing Cluster (HPC) available at Oxford Brookes University. The specifics of the HPC are as follows:

- Intel Xeon processor E5-2600 core
- clock speed of 2.6GHz
- 8 GB RAM per core

3.8 Numerical Errors

By their very nature, the discretisation schemes operated within the CFD solver are prone to errors. The main sources of numerical errors are round-off, discretisation and iterative convergence errors. Respectively, these are due to computational representation of real numbers, Taylor Series Truncation Error (TSTE), and truncated iteration sequence as the solution is close enough to the final solution. The exact contribution or weight of each error source is not clearly defined. In this study, a second order discretisation scheme has been adopted to minimise numerical errors. A thorough process of validation against both existing practises and available experimental data has been carried out, as detailed in the following sections, to ensure accuracy and reliability of the modelled results.

3.9 Model Validation

Model validation has been carried out based on available experimental data concocted at Oxford Brookes University (Hall et al., 2014) and correlations available in the literature.

An initial comparison was drawn between modelled and measured values of the ratio of absorber plate temperature to plenum outlet temperature (T_s/T_{out}). This term is a measure of the system thermal output, and is thought to be a good indication of the ability of the CFD model to predict the realistic TSC's behaviour. The plate temperature was calculated as the average of several locations on the back side of the plate and it is taken as representative of the interaction between internal and external flows in steady-

state conditions. The plenum outlet temperature was taken at the top of the cavity behind the absorber plate installed at the insulated building façade (Hall et al., 2014).

The second validation criterion was Heat Exchange Effectiveness (HEE). HEE is important because it indicates the portion of heat transferred from the absorber plate, acting as a heat exchanger, into the plenum outlet.

The third step of model accuracy verification was to compare the correlations available in the relevant literature for HEE, with both the experimental data from Hall et al. (2014) and modelled data. This step was also perceived to be essential to evaluate the present work in the context of the worldwide frame of study.

A set of 15 operating conditions covering a wide range of climate variables has been used to assess the CFD model accuracy and reliability. These are summarised in Table 3-2.

Table 3-2 Details of the cases used for validation.

Case Number	Ambient Air Temperature (℃)	Wind Speed (m/s) U_∞	Wind Angle (°) β	Suction Ratio V_s/U_∞	Vertical Solar Radiation (w/m^2)
1	4.33	2.77	24.67	0.0087	425.09
2	5.13	2.83	37.67	0.0086	585.99
3	6.27	5.60	12.33	0.0044	646.90
4	7.33	2.80	12.33	0.0089	277.80
5	8.40	4.97	-1.33	0.0049	570.08
6	9.27	6.90	4.67	0.0034	101.04
7	10.57	3.63	14.33	0.0067	621.92
8	10.70	4.50	2.33	0.0036	629.64
9	11.00	5.47	7.67	0.0030	767.11
10	11.53	3.60	-0.33	0.0069	735.64
11	11.80	3.70	8.33	0.0067	724.31
12	12.00	3.00	6.67	0.0083	705.82
13	12.07	3.43	13.00	0.0073	577.79
14	12.10	3.23	1.33	0.0076	546.72
15	12.13	2.90	1.67	0.0086	615.50

Figure 3-17 shows the comparison of temperature ratio between modelled and experimental data, together with 10% and 5% error lines. It can be seen that 80% of the cases are predicted with 5% accuracy, which proves the ability of the model to duplicate the realistic situations. Due to the arithmetic operations, the errors in predicted HEE are expected to be more significant. Figure 3-18 shows that 100% of the modelled HEE values are predicted to within 10%, whilst 23% of these are predicted to within 5%.

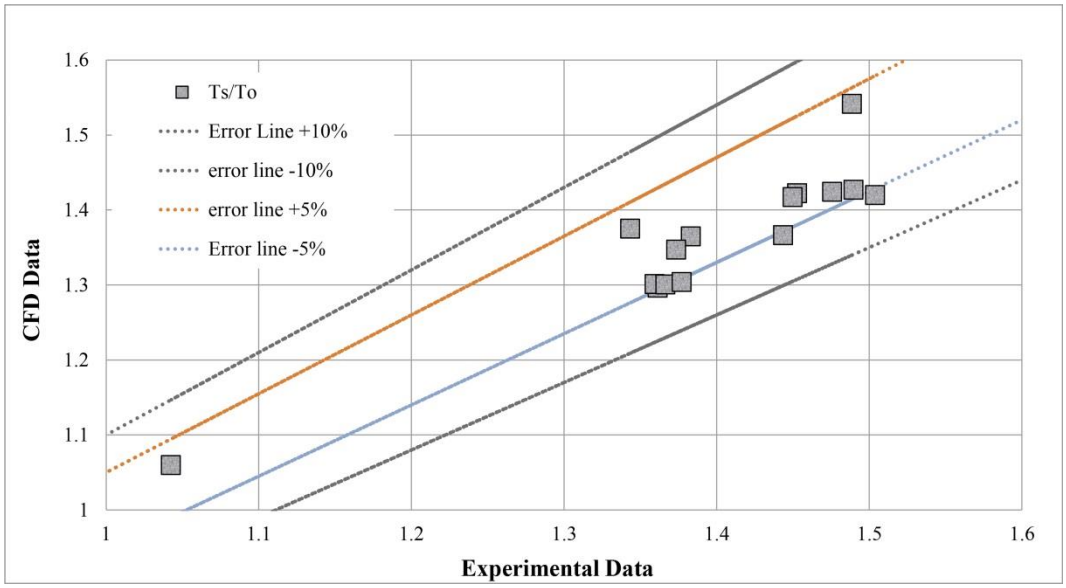

Figure ß-17. Comparison between the CFD results and the experimental data for the ratio of absorber plate temperature and plenum outlet temperature (T_s/T_{out}).

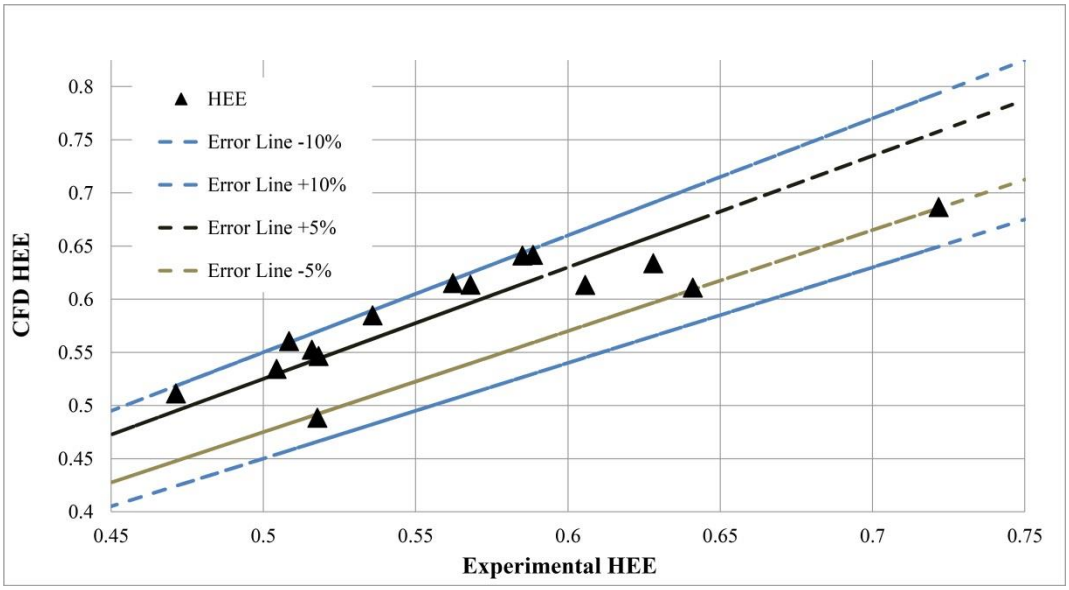

Figure ß-18. Comparison between the CFD results and the experimental data for Heat Exchanger Effectiveness (HEE).

At this stage, it was also important to verify if the CFD model developed in this work, intended as a more holistic and comprehensive physical representation of TSCs than previous available models and correlations, delivered comparable results. Thus a comparison was carried out between the correlations developed by Kutscher (1992) and Van Decker et al. (2001), and the levels of HEE produced by using the present CFD model Values of HEE from experimental data were also included in the comparison. In Figure 3-19, HEE is plotted against the ratio between the Reynolds number based on the suction velocity

and that based on the wind speed. Re_s/Re_w is a non-dimensional term that accommodates comparison of effectiveness values regardless of the different system's operating conditions such as mass flow rate and wind speed, or system geometry/size. Moreover, it has been assured that the chosen experimental data are within the ranges at which the correlations are deemed to be valid. Although the present study and the two previous works differ in their approach to modelling Heat Exchange Effectiveness, however sufficiently similar patterns are expected.

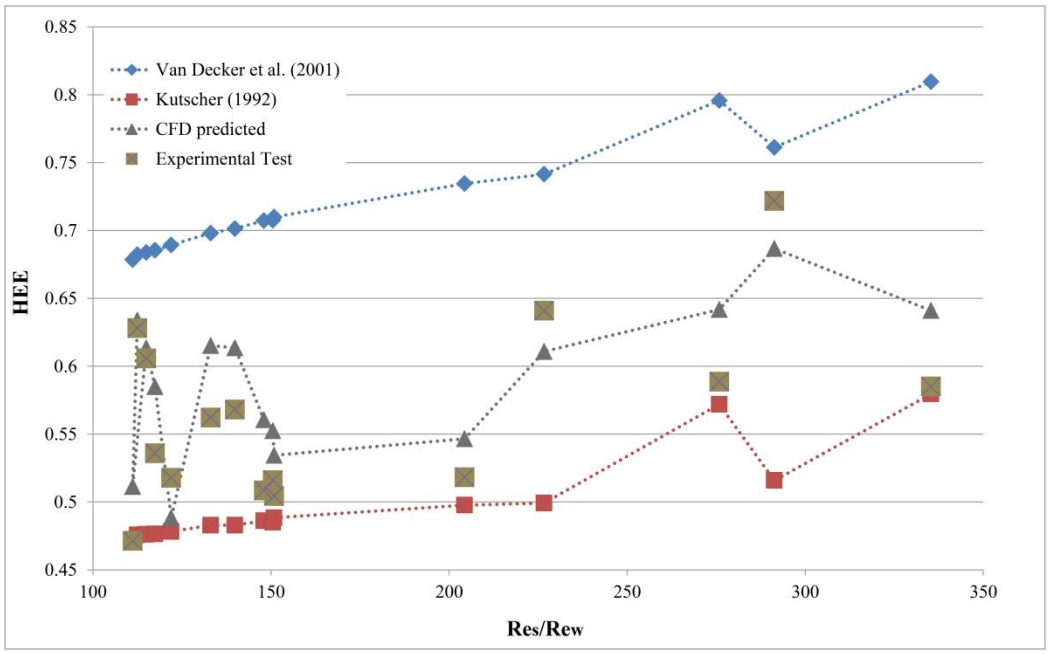

Figure 3-19. Comparison between the HEE values predicted by the current CFD model and the correlations by Kutscher (1992) and Van Decker et al. (2001) regarding the Experimental tests by Hall et al. (2014)

As can be seen in Figure 3-19, the predicted effectiveness values by both Kutscher (1992) and Van Decker et al (2001) correlations demonstrate a similar pattern to the CFD data and the experimental data (Hall et al., 2014) across the wide range of climatic conditions used as input data. Specifically, it is seen that in all cases, HEE tends to increase as Re_s/Re_w increases, and that both CFD predicted and experimental levels of HEE appear to be bound by the Kutscher and Van Decker correlations, which tend to return lower and higher values of effectiveness, respectively. In contrast to the current study, parameters like wind direction, sun orientation, absorber plate properties (i.e. emissivity, absorptivity, and thermal conductivity) are not included in Kutscher's and Van Decker's correlations. Whilst the difference between the CFD predicted data and the experimental ones is less than 10% in all cases, the deviation between experimental HEE and the two correlations reaches up to 28% and 24% for Van Decker et al. (2001) and Kutscher (1992), respectively.

Considering that the experimental measurements inherently include a degree of uncertainty due to life-like test conditions, the results of validation exercise suggest that the sophisticated CFD model developed in this work is able to deliver an accurate and realistic representation of the performance of a TSC system. Importantly, the variety chosen for the validation cases indicates that the CFD model is flexible in nature and well suited to capture the influence of different climatic conditions, which is essential for design optimisation.

3.10 Absorber Plate Geometry Optimisation

Assuming that the computer simulations are adequately representative, a model-based optimisation study is eligible to determine optimum conditions to drive the design of real systems (Montgomery, 2012). Within the large range of variables that affect the performance of TSCs, the so-called Factor Variables (e.g. geometry of the absorber plate) can be adjusted or optimised by designers and/or manufacturers. The present section outlines an optimisation study carried out to introduce a viable methodology capable of delivering an improved combination of absorber plate geometrical variables, which achieves the highest possible heat exchange effectiveness. The method can of course be extended to determine other optimal sets of factors variables, using single or multi-objective optimisation approaches.

The factors of interest in this study are pitch (P), diameter (D), and thickness (t). The single objective of the model-based optimisation is HEE. The ranges of variability for the three factors are:

- $0.8 \text{ mm} \leq D \leq 3.2 \text{ mm}$
- $0.7 \text{ mm} \leq t \leq 1.2 \text{ mm}$
- $7 \text{ mm} \leq P \leq 23.33 \text{ mm}$

Other factors that may exert an impact on the ‘responses’ of the optimisation study are held as constant. ‘Held-constant factors’ are shown in Table 3-3, and they were given values representative of average TSCs operation in the research literature and industries.

Table ß-3. Held-constant factors for geometrical optimisation

Ambient Air Temperature (°C)	Wind Speed (m/s)	Wind Direction	Suction Ratio	Solar Radiation (w/m^2)	Mass Flow Rate (Kg/s)
10	5	0	0.008	600	0.0123749

In order to reach an optimised configuration of the aforementioned factors, a series of different combinations within the specified range are investigated. However, since the number of combinations can be infinite, it is important to choose a representative and statistically relevant sample of factors (Garud et al., 2017). Design of Experiments (DoE) has been employed for this purpose. DoE is a statistical approach to plan experiments (or, in the present case, simulation runs) in a way to capture the interaction of multiple factor variables. The use of DoE would facilitate an appropriate data collection, as well as data analysis to determine the impact of each variable on the output response. The steps to produce a meaningful and scientific outcome can be summarised as:

a) Definition of sampling-DoE

b) Performing the simulations

c) Curve-fitting and optimisation

d) Model-based regression and optimisation.

The analysis has been performed using the Model-Based Calibration (MBC) toolbox of MATLAB, which offers a wide range of DoE and regression models. The toolbox provides the ability to prepare the DoE, and carry out the final optimisation within the same package. The designed experiments (or runs) were simulated using the validated methodology described above including the meshing method, definition of the model's physics, boundary conditions and convergence criteria. Various geometries were created based on the factor variables defined by DoE. A fixed set of climatic and operating condition was used to all runs, see Table 3-3. Figure 3-20 outlines a flowchart of the statistical analysis and optimisation work.

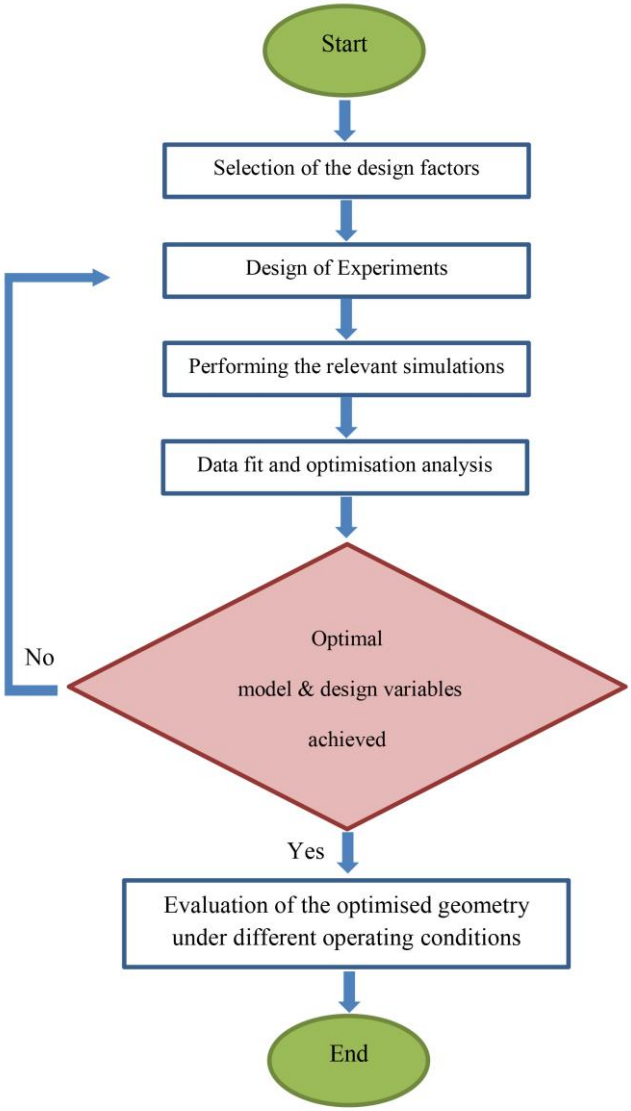

Figure 3-20. Flowchart of statistical analysis and optimisation study.

3.10.1 Sampling

Systematic and random sampling are the two general approaches of designing an experiment within an area of interest. Systematic sampling refers to the selection of the design points on the basis of a fixed periodic interval. Random sampling, however, employs sampling algorithms which cover the whole region of interest whilst each possible sample point holds an equal probability of being selected. Although systematic sampling may seem a more straightforward method, its main drawback is the fact that a larger number of points is required in order to, 1. reduce the sampling bias, and 2. provide a representative response against the input data. Random sampling is more statistically robust as it eliminates the

systematic bias as all the points within the specified range are equally treated to be part of the experiment (Montgomery, 2012).

Whilst there are different choices of design of experiments, space filling design is perceived to be suitable for computer models in which the response variables are mathematically calculated and free from signal noise. Unlike physical experiments, replicate runs are not essential for computer experiments as the response variable is thought to be identical for a specific set of data input. Most of the space-filling designs are replication-free which makes them more suitable for computer simulation experiments. Furthermore, space filling designs spread the design points in a way that no prior knowledge to the form of the model response is required. Implicitly, each probable design point is expected to deliver an interesting phenomenon (Santner, 2013).

Halton sequence space-filling design has been employed for design of experiment in this study (Montgomery, 2012). Halton is a low discrepancy quasi-random sequence. Quasi-random sequences benefit from both the feature of randomised sampling and a lattice that ensures design points do not clump together and will cover the whole region of interest evenly (Figure 3-21). A total of 30 combinations of the factor variables, including the eight points along the region boundaries have been generated through the space-filling DoE for the simulation runs. Figure 3-22 shows the 3-D display of the design of experiment.

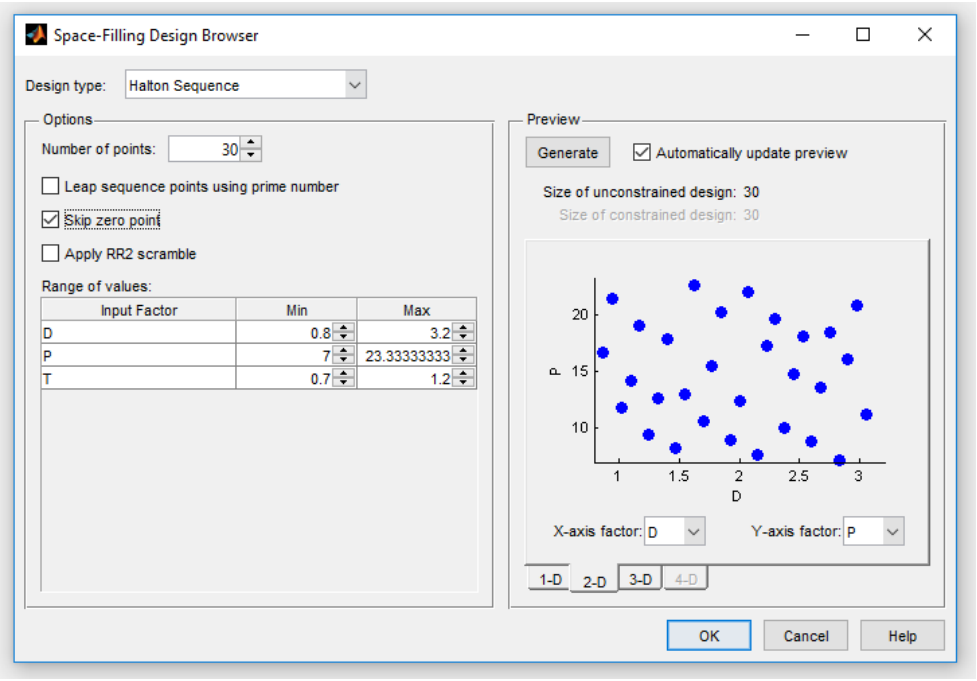

Figure 3-21. An example 2-D snap of space filling design excluding the extreme points.

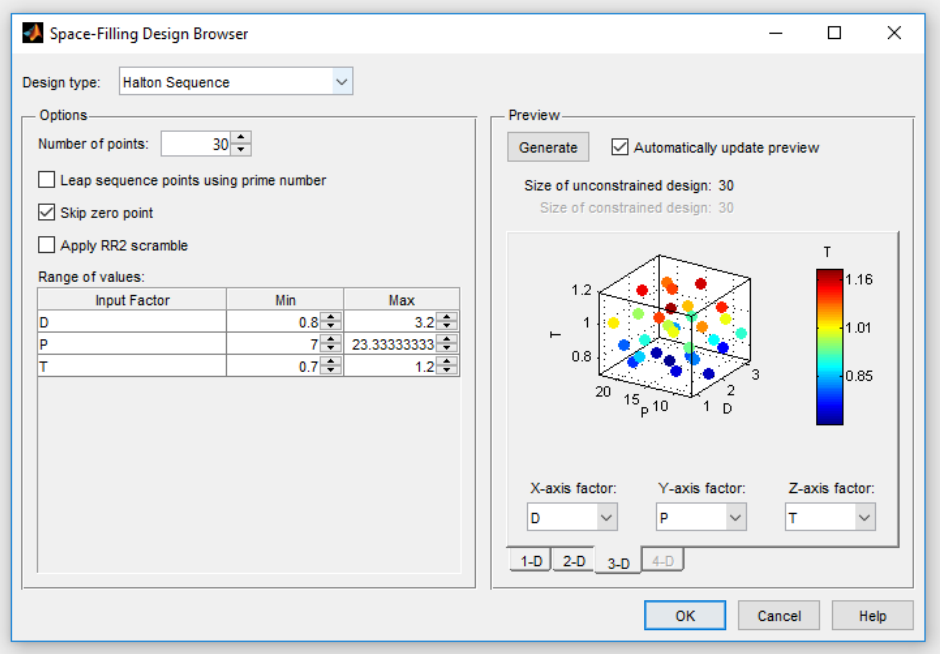

Figure 3-22. A 3-D view of design of experiment excluding the eight extreme points along the boundaries.

3.10.2 Data analysis

Once all the simulations are completed, the output data are used to perform the analysis. Generally, the primary aim is to use the predicted HEE values to generate correlations between HEE and the geometrical variables using different regression models. These correlations are normally referred to as meta-models, as they are effectively used to model the outcome of a model. An important step at this stage is to determine the validity and predictive ability of the generated meta-models. Once this is completed, the optimisation exercise calculates the best combination of factors variables delivering the highest value of HEE.

Curve fitting

The output data generated from the simulations are taken into the MBC Toolbox to create a statistical model for the response variable (HEE) as a function of the three geometrical factor variables (Figure 3-23). Curve fitting is used to identify these relationships, which are in turn able to predict the response variable by interpolation in points at which no data is available.

The response variables can be projected in a series of 3D plots called the surface responses. Optimised geometrical conditions delivering the highest values of HEE can be located on the response surfaces. For a given independent factor variable, the other two geometrical variables can be determined from the projected response surface to reach an optimised situation.

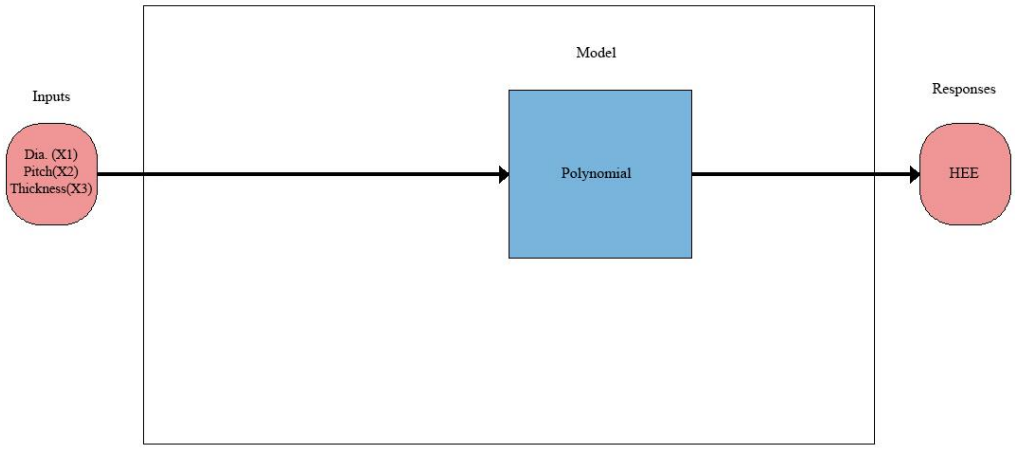

Figure ꞵ-23. An overview of the regression model generation.

Beside accuracy and ability to predict, model simplicity has been considered in choosing the data fitting model. Polynomial models of second, third and fourth order have been chosen for data regression analysis (Figure 3.20).

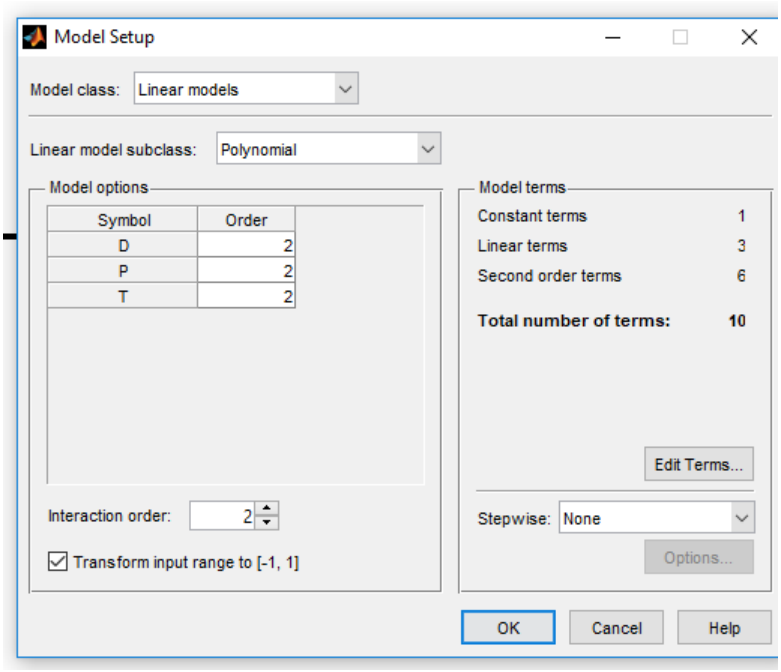

Figure ꞵ-24. An example of model setup in MBC interface.

3.10.3 Quality of curve fitting

It is crucial to demonstrate that the fitting models are accurate, predictive, and free of non-effective variables. The four measures considered to assess model quality are:

- RMSE

The Root Mean Squared Error (RMSE) calculates the distance (i.e. the error) between the actual points to the regression line at the fixed x values. Practically, RMSE quantifies the quality of the distribution of points around the regression line.

$$RMSE = \sqrt{\frac{\sum_{i=1}^{n}(y_i - \hat{y}_i)^2}{n}} \quad (3\text{-}4)$$

where y is the observed dependent variable, $\hat{y}$ is the dependent variable predicted by the regression, and n is the sample size.

- PRESS

Predicted Residual Error Sum of Squares (PRESS) is a measure of predictive power of statistical models.

$$\text{PRESS} = \sum_{i=1}^{n}(y_i - \hat{f}_i)^2 \quad (3\text{-}5)$$

where $\hat{f}_i$ is the prediction for y_i while the ith point is out-ruled. This estimates how accurate the model is able to predict the points at which no data is available.

It's important to compare it with RMSE as it may indicate overfitting issues of the regression line. Whilst RMSE is minimised as the regression line chases the data set, this may lead to strong oscillation and does not necessarily deliver good predictions where no data is available. PRESS and RMSE values being about equal ensures the predictive ability of the generated model. RMSE and PRESS values for the regression line are automatically calculated by the software.

- R-squared

It is expressed in percentage and defines the proportion of variability in the dependent variable that can be explained by the regression model. In other words, it states what percentage of the response variation is predicted by the independent variables.

R-squared is calculated as:

$$R^2 = 1 - \frac{SS_{error}}{SS_{total}} \quad (3\text{-}6)$$

SS_{error} is error sum of squares and SS_{total} is total sum of squares:

$$SS_{error} = \sum_{i=1}^{n} (y_i - \hat{y}_i)^2 \quad (3\text{-}7)$$

$$SS_{total} = \sum_{i=1}^{n} (y_i - \bar{y})^2 \quad (3\text{-}8)$$

where $\bar{y}$ is the mean value of the observed dependent variable.

- Adjusted R-squared

This is the second coefficient of determination. This coefficient is adjusted on the basis of the number of parameters. R-squared always increases regardless of the relevance of the parameters (independent variables) added into the model. Adjusted R-squared though gives the percentages of variation explained by the parameters that actually matter.

$$R^2_{adj} = 1 - \left[\frac{(1 - R^2)(n - 1)}{n - k - 1}\right] \quad (3\text{-}9)$$

where *k* is the number of independent variables.

Ultimately, it is important to assess if the behaviour of the predictive model is consistent to the realistic behaviour of the system. The significant characteristics of the produced regression lines have been compared to the CFD simulated output to identify the most realistic predictive model. The results concerning the quality of the regression models are presented below in the Results and Discussion Chapter.

3.10.4 Optimisation and validation

The *foptcon* algorithm, available within a proprietary version of the optimisation toolbox in MATLAB, has been used for this single objective multi-variable optimisation study. *foptcon* algorithm in is a modified version of *fmincon* from the MATLAB Optimisation Toolbox™, which is suitable to find minimum and maximum of constrained nonlinear multi-variation function (CAGE User's Guide, MATLAB & SIMULINK R2017a).

The target value for HEE is 1, which means the system is able to conduct all the absorbed heat into the building. Therefore, the optimiser is asked to find the best combination of factor variables at which the system will be able to deliver HEE closest to 1. In order to secure the accuracy of the process, five

different initial conditions were set in the optimisation tool to approach the highest value of HEE (Figure 3-25). The algorithm starts from each initial point to find the closest relative optimal point. Having five or more initial conditions at different locations ensures the solution is as close as possible to the absolute optimum.

The absorber plate geometrical optimisation methodology presented in this section has been carried out using fixed values of climate variables. Of course, different climatic conditions influence the thermal performance of TSCs. A validation exercise has ultimately been performed to assess robustness and generality of the optimal geometry identified with this methodology, against a range of relevant climatic conditions. The results of this validation are presented in the Results and Discussion Chapter.

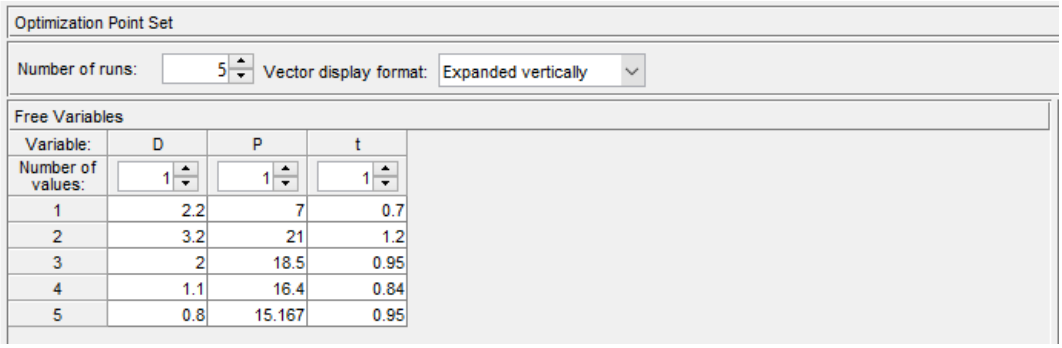

Variable:	D	P	t
Number of values:	1	1	1
1	2.2	7	0.7
2	3.2	21	1.2
3	2	18.5	0.95
4	1.1	16.4	0.84
5	0.8	15.167	0.95

Figure 3-25. A screenshot of the optimiser panel showing the initial conditions setup.

3.11 Concluding remarks

This study involved the development of a high-resolution, 3-dimensional, steady-state, Reynolds-Averaged Navier-Stokes (RANS) CFD approach to model cassette-panel TSC systems. Angle of wind and the actual position of the sun have been taken into account in the simulations.

Experimental data from tests conducted at Oxford Brookes University have been used to validate the accuracy of the CFD model. Further remarks of the methods which have been employed to reach the objectives of the research are as follow:

- Due to the inherent complexities of the airflow taking place across TSCs, very careful methods should be deployed to capture the underlying physics. These complexities include the turbulent flow around the perforations and inside the plenum, the multi-scale geometry of the system, non-uniform suction through the perforations and the jet

flows emerging from the perforations into the plenum. Grid generation, geometry of the model, boundary conditions and numerical models are the most important factors which should address the associated complexities.

- A multi-block and structured grid is a convenient method for grid generation sub-dividing the computational domain into regions which need more control over grid refinement and appropriate mesh aspect ratios. These regions are mainly the solid-fluid interfaces, perforations, the absorber plate and the zones at which jet flows occur.

- The commercial CFD software, STAR-CCM+ has been used to solve steady-state, three-dimensional RANS equations with the Realizable $k-\varepsilon$ turbulence closure model over the computational domain. A segregated flow solver has been adopted to solve flow and energy equations using a second order upwind discretization scheme along with the SIMPLE algorithm for pressure-velocity coupling.

- The gradients of the airflow are assumed to be less significant in y direction compared to the other two directions. Hence in order to reduce the size of the computational domain a full section of the system has been modelled and developed in a way to replicate the realistic condition.

- Validation study has been carried out using 15 points amongst the available experimental data. The CFD results have shown a good agreement with the experimentally measured temperatures and HEE values. The CFD predicted values of HEE have also been compared with the existing well-known correlations (Kutscher, 1992; Van Decker et al., 2001) assessing its predictability. The comparison has indicated that the CFD model predicts the TSC performance more accurate than the literature correlations.

- An optimisation methodology has been designed in order to address a practical optimised design of TSCs using CFD models. Perforations diameter (d), pitch distance (p), and the plate thickness (t) have been taken into account as variables factors.

- A range of practical values have been considered for the variable factors. Design of Experiments (DoE) is the method which has been employed to provide a sample population of the all possible combination of D, P, and t. An initial set of 30

experimental points were designed to be simulated by the CFD model. The designed experiments (simulation runs) have been performed using the validated methodology comprising the meshing method, definition of the model's physics, boundary conditions and convergence criteria. Various geometries have been created based on the factor variables defined by DoE. A fixed set of the climatic and operating condition has been applied to all the simulations. The results will be analysed in order to reach an optimised geometry design and the correlation between the response factor and the associated variables.

Chapter 4 System sensitivity to geometric and climatic variables

4.1 Introduction

The main aim of this research work has been to develop, validate, and then apply a large-scale, comprehensive CFD model of a typical cassette-panel TSC system, to assess its flow and thermal behaviour under a large range of operating conditions. Such assessment is intended to support design improvement and further investigation aimed at the enhancement of TSCs' thermal performance. After an initial review of general airflow and thermal field characteristics of the modelled TSC system, this chapter presents the results concerning a range of parametric studies, where relevant climatic and other operating variables are varied in isolation. The last section presents the results concerning the optimisation of absorber plate geometrical features.

4.2 Assessment of the general characteristics of airflow and thermal field

Figure 4-1(a) shows the velocity streamlines and vectors in the computational domain for one representative TSC operating point (wind speed of 6m/s and wind angle of 22.5˚). It can be seen that the angled wind approaches the absorber from the left and exits the domain on the right-hand side. Whilst the airflow enters the domain at a certain angle in the far field regions, it rather quickly takes a more parallel direction to the plate as it streams closer to the external surface of the TSC. The result can inform experimental work, especially in terms of where to best place weather stations in order to record the actual wind characterisitics without being affected by the building. Figure 4-1(b) displays the formation of jets in the plenum due to the suction through perforations and the airflow in the far field from the building' facade. It is notable that from a very high speed of 8 to 10 m/s, the jets energy is quickly dissipated into the core flow travelling up at relatively low velocity (0.5 to 1.5 m/s).

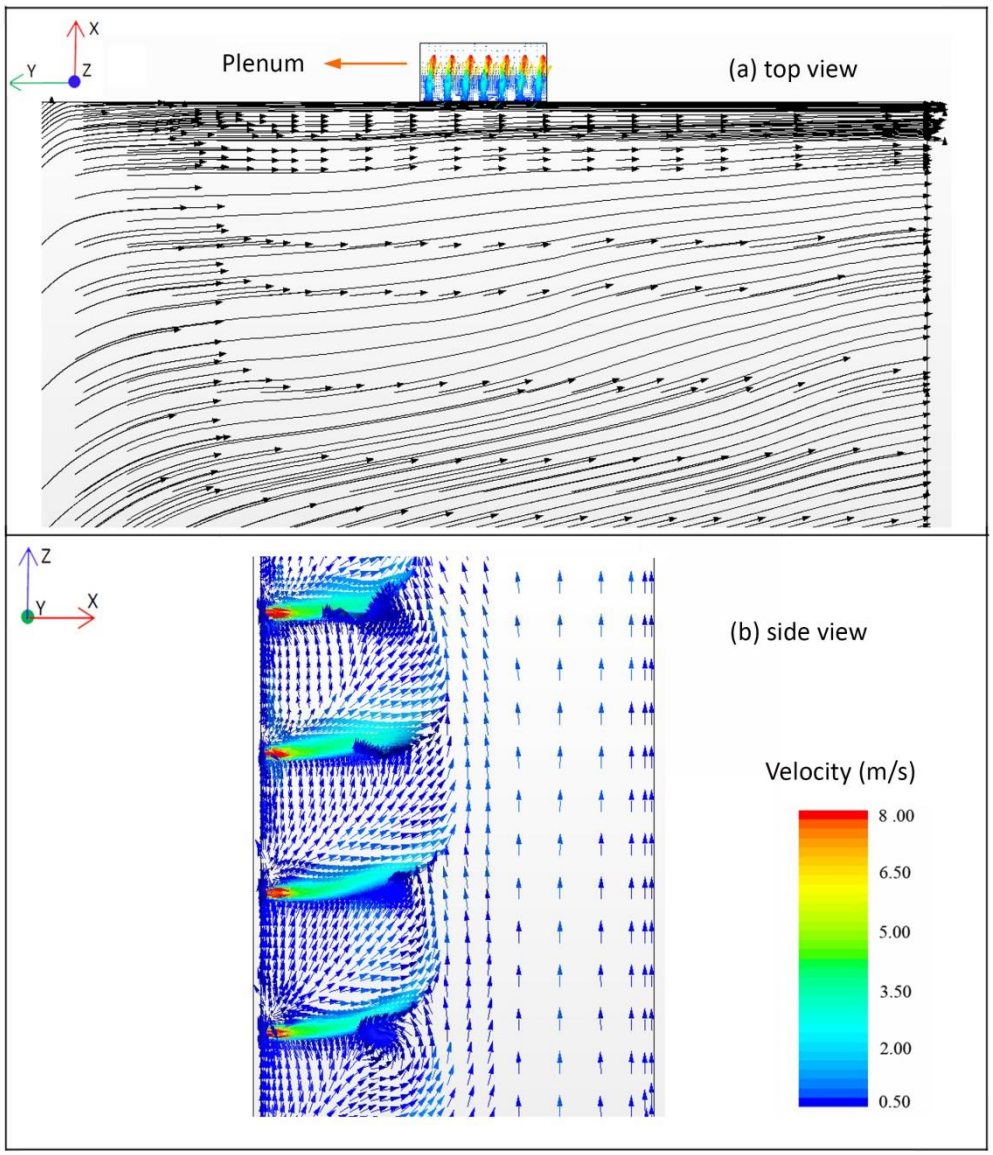

Figure 4-1.(a) Velocity streamlines of ambient/external airflow together with jet stream inside the plenum (view from above); (b) Airflow within the plenum (side view).

Due to the suction generated by the fan at the top side of the plenum, the airflow experiences different velocity and pressure as it moves along the system. As shown in Figure. 4-2, the pressure grows negatively moving upwards and, correspondingly, the bulk velocity within the plenum increases (Figure. 4-3). Figure 4-4(a) shows the temperature distribution over the absorber plate. For increased clarity of visualisation, the regions with temperatures above 23°C are displayed in red and a similar approach is used in other figures throughout this section. A higher level of negative pressure and airflow velocity in the upper part of the plenum causes this part to be relatively cooler especially at the very top, where the highest negative pressure is generated (Figure. 4-2, Section (1)).

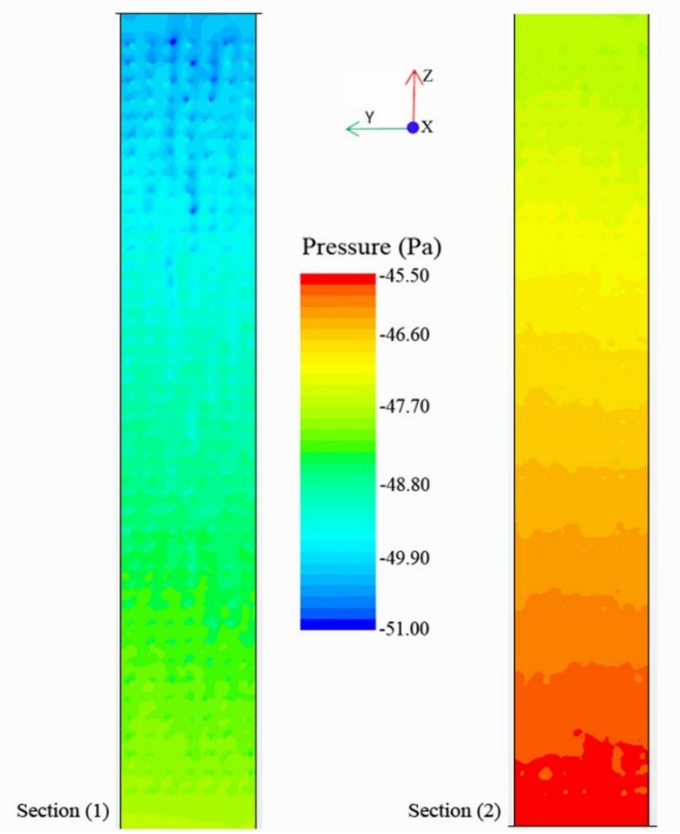

Figure. 4-2. Front-view cross section of pressure distribution on centre-line of plenum, Section (1): upper part of plenum, Section (2): lower part of plenum.

Interestingly, a slightly greater temperature is seen all around the edge of the modelled TSC element, indicating the establishment of an 'edge effect' influencing the thermal performance of the system. This is due the fact that the boundary conditions of the absorber plate at the all sides are set as walls at which the temperature is calculated based on the solution. Having set a constant boundary temperature creates a gradient of temperature all around the absorber. In particular, whilst a relatively colder region was expected to take place at the very top edge due to the outlet mass flow boundary in the plenum, the presence of a fixed temperature wall together with the non-perforated area has pushed the colder region slightly further down on the plate. It can also be seen in the middle and the bottom areas of the absorber plate that the absence of perforations, hence consequently high velocity airflow, has led to relatively hotter regions. This limitation however is considered to have more of a local effect rather than affecting the average temperature of the absorber plate as was ensured with the validation study in section 3.9.

Whilst the importance of the edge effect reduces with increasing front surface (i.e. in full-scale applications), the CFD environment enables exploring the details of how different parts of the absorber plate contribute to the overall outlet temperature (T_{out}) and the corresponding Heat Exchange

Effectiveness. This specific investigation falls outside of the main scope of the present research study and may be object of future work.

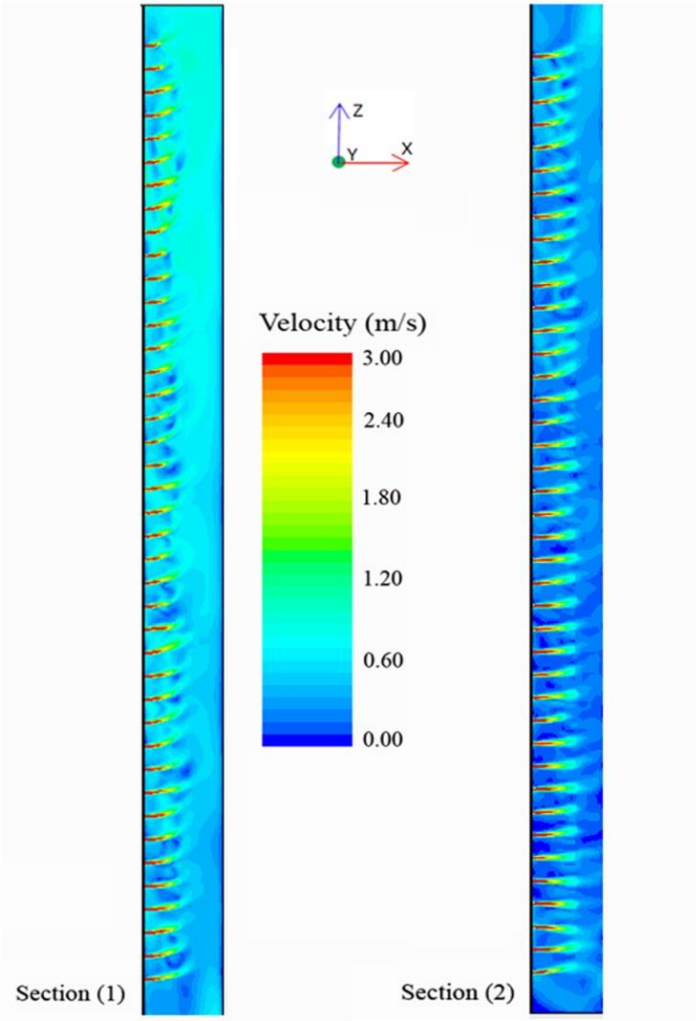

Figure. 4-3. Side-view cross section of plenum showing velocity distribution, Section (1) upper part of plenum, Section (2) lower part of plenum.

Heat Exchange Effectiveness (ε) is defined as the actual heat transferred to the air, relative to the maximum theoretical heat transfer. Its definition is typically given in terms of ambient temperature (T_{amb}), outlet temperature (T_o) and absorber surface temperature (T_s) (Eq. 1-1)[2]. For a given outlet temperature, increasing surface temperature leads to a smaller effectiveness. In other words, the regions on the absorber plate that operate at higher temperature, contribute less to the final air temperature delivered by the system. Figure 4-4 shows the distribution of local HEE, calculated using local value of temperature, over the absorber plate.

[2] $\varepsilon = \frac{(T_o - T_{amb})}{(T_s - T_{amb})}$

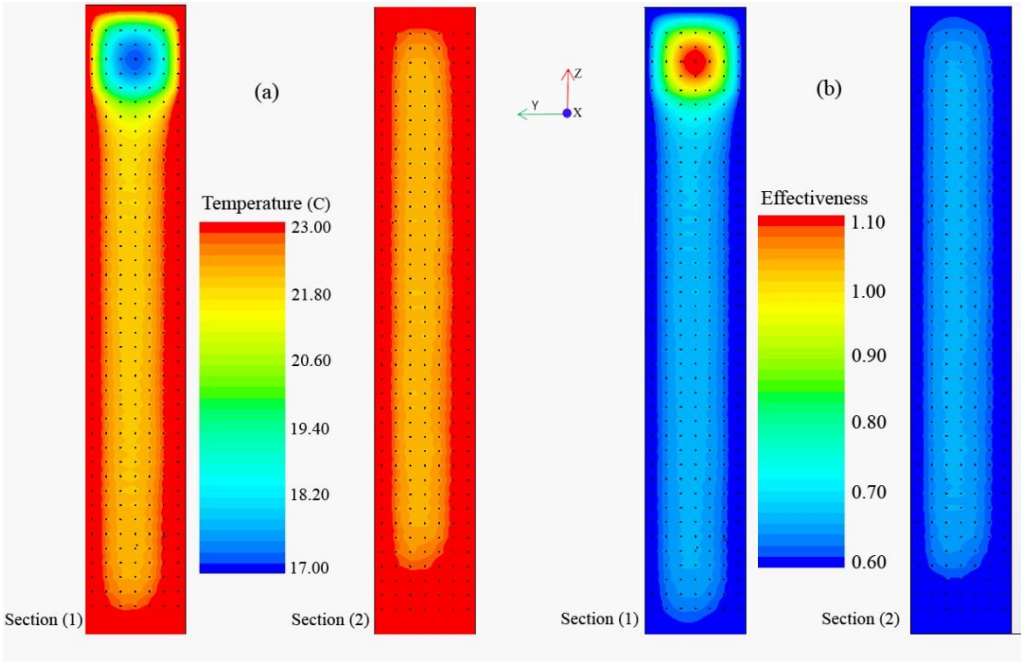

Figure 4-4. Front view of: (a) Temperature distribution over the perforated plate, (b) Heat exchange effectiveness distribution over the perforated plate, Section (1) the upper part of the plate, Section (2) the lower part of the plate.

Heat exchange from the plate to the streaming air in the plenum is clearly maximised around the top-centre region with the levels of HEE around 1, indicating that the surface temperature is either equal or less than the outlet temperature. This phenomenon can be described as the result of high suction streaming in a confined region where more heat is taken away from the plate than received at the same time.

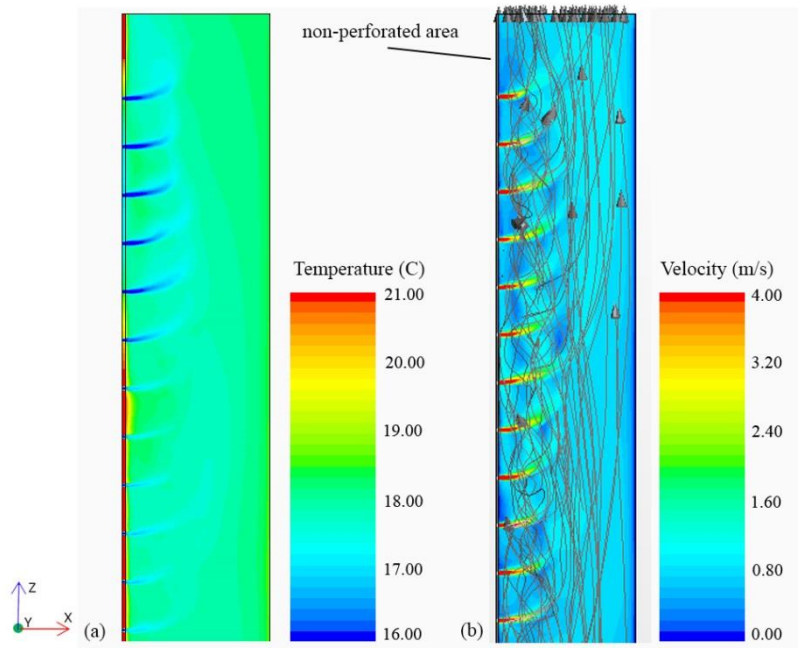

Figure 4-5. Side-view cross section of plenum showing, (a) temperature and (b) velocity distributions in upper part of plenum together with stremlines.

Magnified side views of temperature and velocity distribution in the upper part of plenum are presented in Figure 4-5. Whilst the absence of perforations in the uppermost region leads to higher surface temperature and lower HEE, the increased heat transfer across the first few rows of perforations leads to a localised area of lower temperature and greater HEE.

4.3 Effects of Wind Angle

Whilst all characteristics of the airflow approaching TSCs are believed to be important, the existing literature does not routinely consider the influence of wind angle on the thermal performance of TSC systems. Wind angle can affect the airflow distribution near the perforated plate, which in turn modifies the heat gain of the system and consequently the air 'temperature rise'. Temperature rise refers to the ability of the system to raise the ambient temperature to a higher level at the outlet, and it is defined simply as the difference between the outlet temperature (T_o) and ambient temperature (T_{amb}). Heat gain of the system is represented in terms of thermal efficiency. Thermal efficiency of transpired solar collectors is defined as the ratio of the heat gained by the system to the total solar energy falling on the collector's external surface (Eq. 2-44)[3] . The equation also indicates the amount of heat which cannot be captured by the collector due to the presence of various heat sinks around the system. Heat sinks drag the absorbed energy away from TSCs through convective and radiative heat transfer. A proportion of the solar radiation that falls on the metal surface of the collector emits back to the surrounding area ($Q_{rad.out}$). Likewise, the streaming flow over the absorber surface takes part of the heated air away from the collector through convection ($Q_{conv.out}$).

Sixteen steady-state simulations have been performed to illustrate the parametric influence of wind angle, at different levels of suction ratio, on temperature rise, absorber surface temperature, heat exchange effectiveness, and thermal efficiency of the collector. The summary of the studied conditions is given in Table 4-1. The fixed values of ambient air temperature, wind speed and solar radiation are the mean data of the daytime of 22nd December 2011 . 22nd of December is chosen as the representative day amongst the days that the weather data was monitored and also were available from the tests conducted at Oxford Brookes University (Hall et al., 2014).

[3] $\eta = \frac{\dot{m}c_p(T_{out}-T_{amb})}{IA_S}$

The data gathered from the weather station at the experimental site (Hall et al., 2014) suggest that the wind blows mostly from the west and the south-west (Figure 4-6), as might be expected in the south of England. The simulations have been carried out covering the range of wind angle as detected empirically on the trial site. Noting that the building is south-facing, the equivalent wind angle in the model would span mainly from 0° to 67.5°. Figure. 4-7 provides a schematic view of wind flows approaching the TSC at different angles.

Table 4-1. Details of the case studied for wind angle and suction ratio effect.

Case number	Wind angle (°) $\boldsymbol{\beta}$	Suction ratio $(\boldsymbol{V_s/U_\infty})$	Ambient Air Temperature (°C)	Wind speed (m/s) $\boldsymbol{U_\infty}$	Solar Radiation (w/m2)
1	0	0.004	10	3	600
2	22.5				
3	45				
4	67.5				
5	0	0.006			
6	22.5				
7	45				
8	67.5				
9	0	0.008			
10	22.5				
11	45				
12	67.5				
13	0	0.010			
14	22.5				
15	45				
16	67.5				

Figure. 4-8 shows temperature rise and absorber surface temperature as a function of wind angle, for four different suction ratios. The graphs are based on discrete points and shown in connected lines for increased clarity. It can be seen that both ‘temperature rise’ and ‘absorber surface temperature’ reduce with increasing wind angle. The trend is similar for all cases, with increasing suction ratio leading consistently to lower surface and outlet temperatures. Surface temperature demonstrates an average decrease of 0.21°C per 10° increase in wind angle. This suggests that increasing the angle of the approaching flow enhances the level of turbulence around the plate, leading to increased heat transfer from the plate to the external air flow. Similarly, the air ‘temperature rise’ drops on average by 0.14 °C for every 10° variation in wind angle, with temperature reductions occurring mostly in the range 0-20° of wind angle, indicating that the flow pattern does not change significantly above that range. It is also found that the level of temperature drop per degree of wind direction is more profound at lower suction velocities. This reveals that higher suction rate damps the impact of wind direction on the surface temperature of the absorber plate and the corresponding air temperature rise.

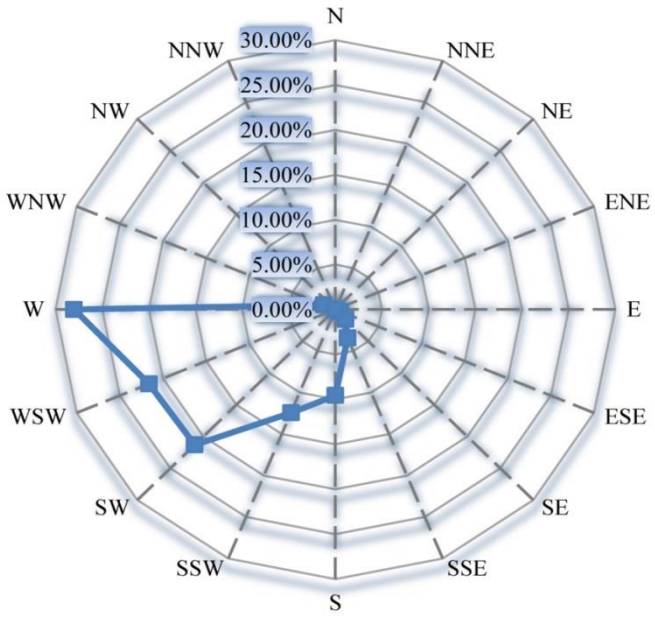

Figure 4-6. The distribution of wind power by direction recorded at the trial site between 22nd December 2011 to 4th January 2012.

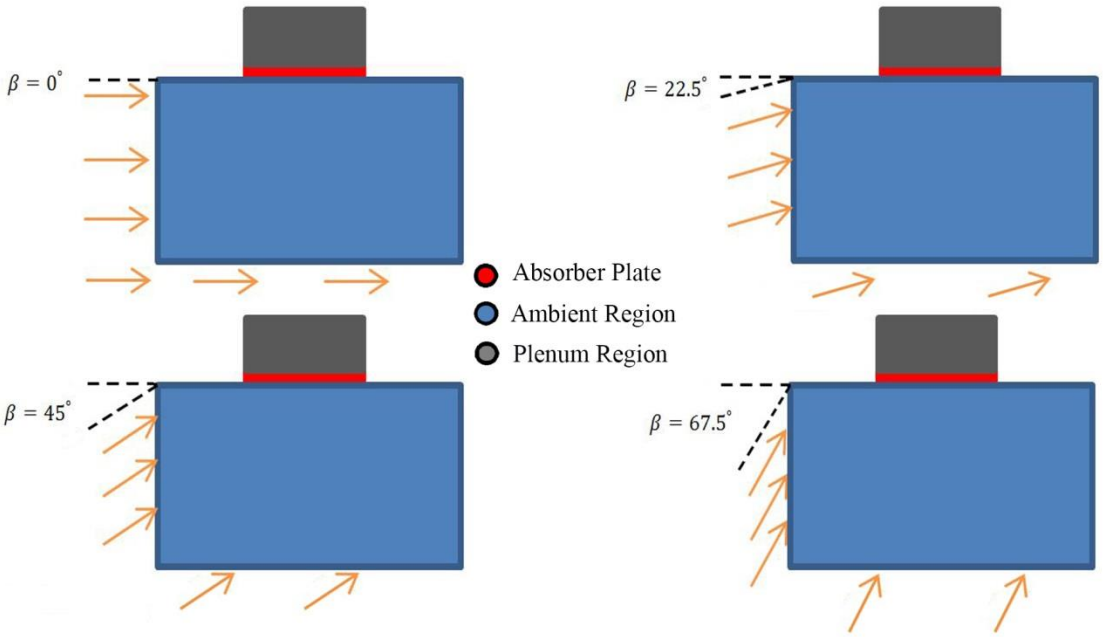

Figure. 4-7. Schematic of wind flow with different angles relative to the absorber plate.

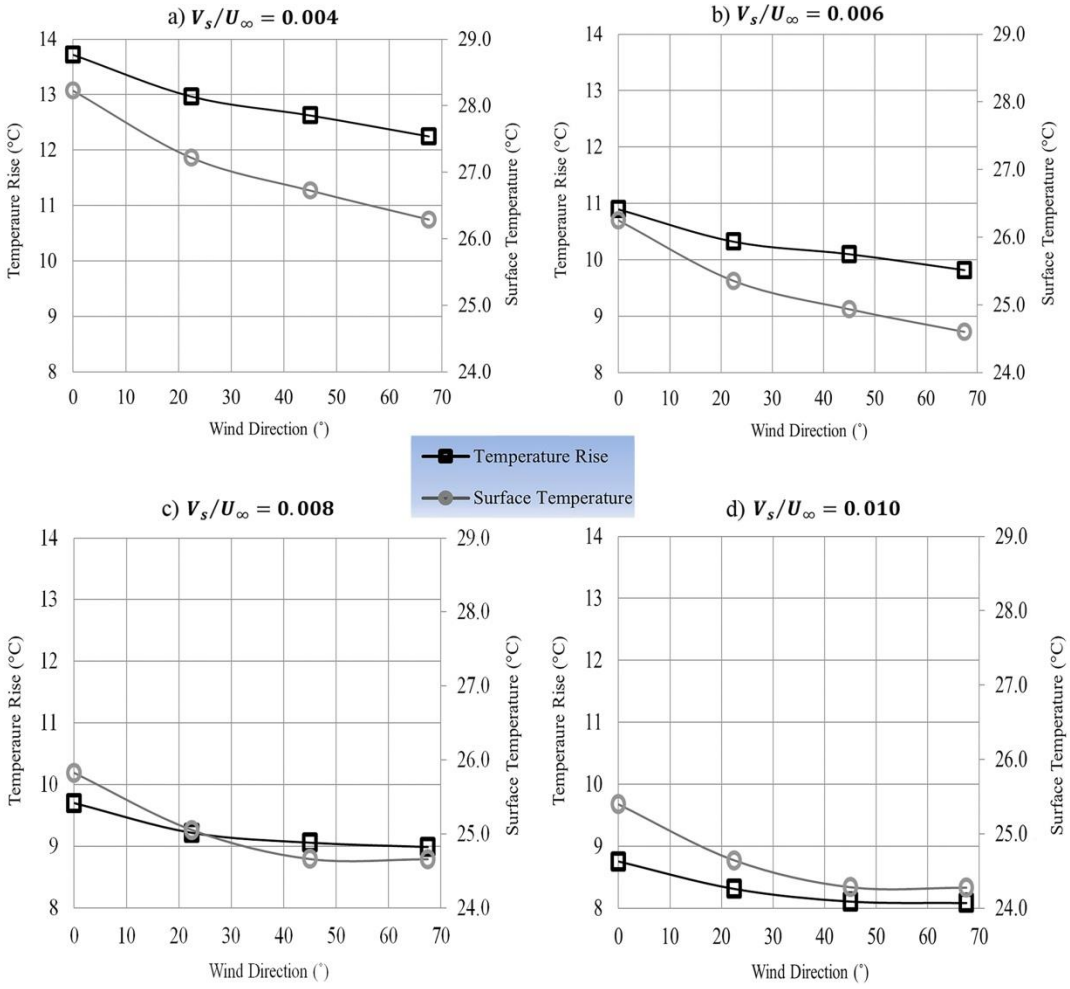

Figure. 4-8. Impact of wind angle on temperature rise and absorber surface temperature for (a) $V_s/U_\infty = 0.004$, (b) $V_s/U_\infty = 0.006$, (c) $V_s/U_\infty = 0.008$, (d) $V_s/U_\infty = 0.010$, with constant wind speed of $U_\infty = 3\ m/s$.

The greatest effect of suction ratio variation occurs at 67.5° wind angle, where 'temperature rise' and 'surface temperature' drop significantly by about 58% and 28%, respectively. The effect is less pronounced but still considerable at a wind angle of 0°, where a change in suction ratios from 0.004 to 0.01 causes 'temperature rise' and 'surface temperature' to drop by 36% and 10%, respectively. A similar pattern has been noted in the relevant literature (Biona et al., 2005; Leon and Kumar, 2007). As the simulations have been performed at constant wind speed of 3 m/s, higher suction ratio implies higher airflow velocity in the vicinity of the perforations, leading to lower temperature gradients on the surface of the absorber. Moreover, higher suction ratios increase the turbulent effect originating from a higher level of interaction between the suction and the approaching flow, which in turn tends to increase the heat transfer from the plate to the ambient air.

The variation of the TSC's operating temperatures helps explaining the corresponding effects on heat exchange effectiveness which, as shown in Figure 4-9, appears to be virtually independent of wind angle. For a given constant suction ratio, wind angle affects surface temperature and outlet temperature almost

equally (Figure. 4-8); in turn, no significant changes in HEE are detected. This implies that different wind angles would not have a major impact on the heat transfer taking place within the perforations and the plenum, which allegedly contribute significantly to the overall heat transfer (Gunnewiek et al., 1996; Van Decker et al., 2001). Therefore the effect of wind direction on temperature rise would be mainly due to temperature variation in surface absorber plate region.

When the suction ratio is varied between 0.004 and 0.01, the average value of HEE drops from 0.75 to 0.57, a drop of 24%. This result is not unexpected as the average drop in temperature rise due to stronger suction ratio is notably higher than that of surface temperature (Figure. 4-8).

Effectiveness can be demonstrated for the main three zones; a) front surface, perforations, and back surface of the plate. This breakdown helps to understand how wind direction and suction ratio affect heat transfer in different parts of TSC and why overall heat exchange effectiveness stays constant against wind direction. Accordingly overall HEE can be calculated from Eq. 2-30.

Figure 4-9 shows that no significant changes in HEE take place in any of the aforementioned regions. However, it is interesting to note how wind direction affects heat transfer in each region. Whilst effectiveness stays almost constant at the front surface of the absorber when wind angle increases, it shows opposite trend in the perforations and back surface regions. The results indicate that wind blowing at an angled direction would enhance and reduce heat transfer in the perforations and back surface, respectively. This confirms the theory advanced by Kutscher (1992) that heat exchange in TSCs occurs mainly at the front surface of the absorber.

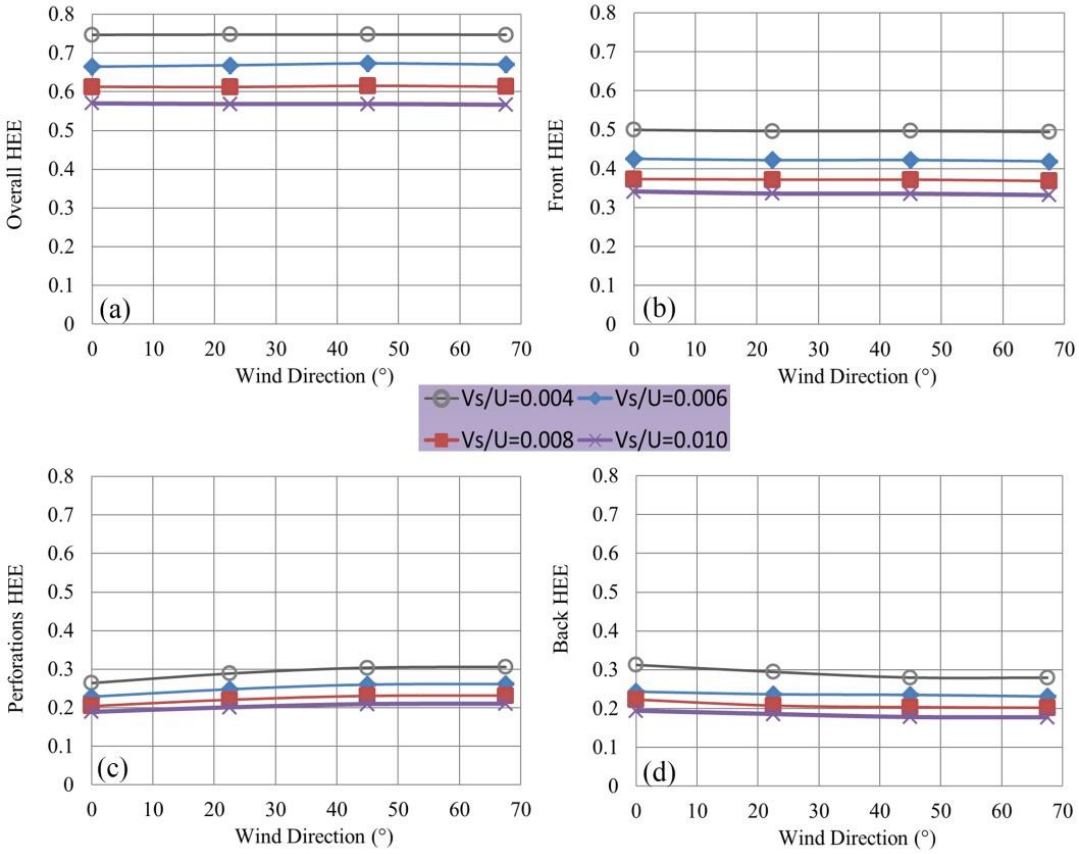

Figure 4-9. Impact of wind angle on heat exchange effectiveness performed by (a) the whole system, (b) the front surface, (c) the perforations, and (d) the back surface at different suction ratios.

Figure 4-9 also shows that the magnitude of HEE for the back surface and perforations is very similar. The average contributions to the overall HEE are calculated as 62.3% from front surface, 21.9% from perforations, and 15.8% from back surface.

This is in contrast to the work of Van Decker et al. (2001), which reports that the perforations contribution to the overall HEE is almost three times larger than the contribution of back surface (28% vs 10%, respectively).

Figure. 4-10 shows the thermal efficiency for the operating conditions examined in this section, as a function of wind direction, at four different levels of suction ratio. Wind direction affects thermal efficiency more visibly when compared to HEE, however, the largest calculated variation of thermal efficiency was only 11%. The maximum reduction in thermal efficiency is found to take place at the lowest suction ratio of 0.004, whereas this drop reduces to about 7.6% at 0.010 suction ratio.

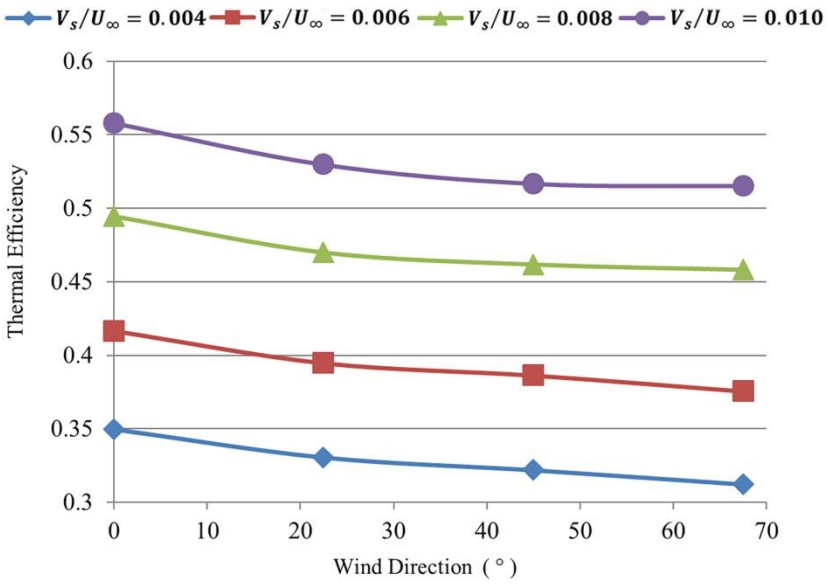

Figure. 4-10. Impact of wind angle on thermal efficiency for the studied suction ratios at constant wind speed of $U_\infty = 3\ m/s$.

Thermal efficiency at low suction ratio also tends to be smaller than at high suction ratio. On average, it changes from 0.33 to 0.53 as suction ratio increases between 0.004 and 0.010. This is because the gained heat is a function of mass flow rate, and higher suction is able to capture more of the heated air adjacent to the plate. Whilst Figure. 4-8 and Figure 4-9 suggest that higher suction ratios result in lower grade heat, the analysis also indicates that higher suction ratios are beneficial in at least two ways: Damping the negative impact of wind direction and delivering larger amount of heat, regardless of the wind direction.

To better understand how the interaction between wind direction and suction ratio causes variation in thermal performance, the pressure drop across the system is calculated. Figure 4-11 presents the pressure drop of the system as a function of wind direction, having suction ratio as the parametric variable. Pressure drop is negative for all cases, which implies that suction pressure at the outlet is higher than at the inlet, as expected. Increasing pressure difference at the fixed suction ratios implies that angled wind creates reverse flow and reduces the suction power by creating negative pressure in opposite direction relative to the normal flow streaming through the perforations. This may explain why thermal efficiency falls down as wind direction grows.

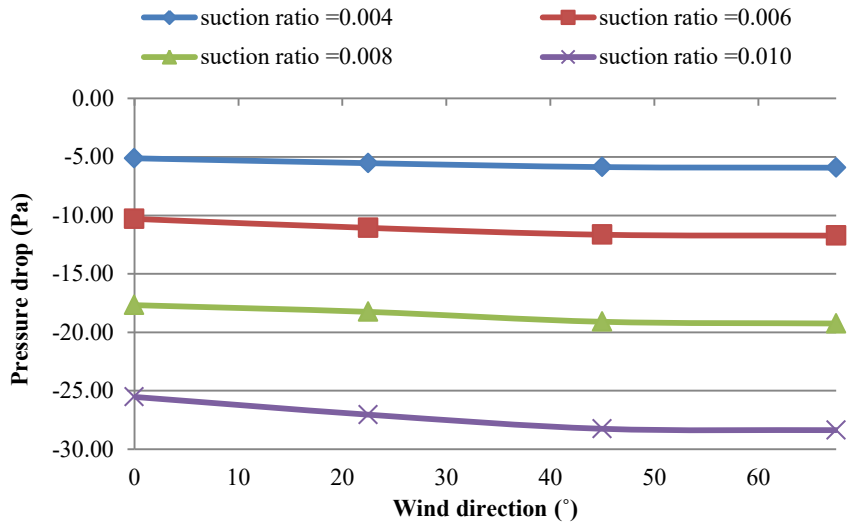

Figure 4-11. Mean values of pressure drop versus the studied wind direction for different suction ratios.

As shown in Figure 4-11, the pressure drop is also intensified by larger suction ratios. In fact, the variation of pressure drop due to suction ratio is much more significant than that of wind direction. This is perceived to be the reason why suction ratio shows a greater impact on the thermal performance of the TSC system compared to the wind direction (Figures 4-8 to 4-11).

The pressure drop due to the increasing suction ratio from 0.004 to 0.010 ($p_{0.010} - p_{0.004}$) is shown in Figure 4-12. The pressure drop is presented against the increasing wind direction. The averaged pressure drop over the perforations and the outlet hole of the system provide a comparative understanding of 'temperature rise' and 'surface temperature' variations whilst the wind direction varies. Although the pressure drop doesn't show a significant variation against the wind direction growth, it is notable that the level of pressure drop at the system outlet is considerably higher than that at the perforations entrance. This implies that, as wind angle changes, the system holds a more consistent suction power at the perforations entrance. This is perceived to be the reason why surface temperature experiences less variation than the outlet temperature, causing lower effectiveness at higher suction ratios (Figure 4-9).

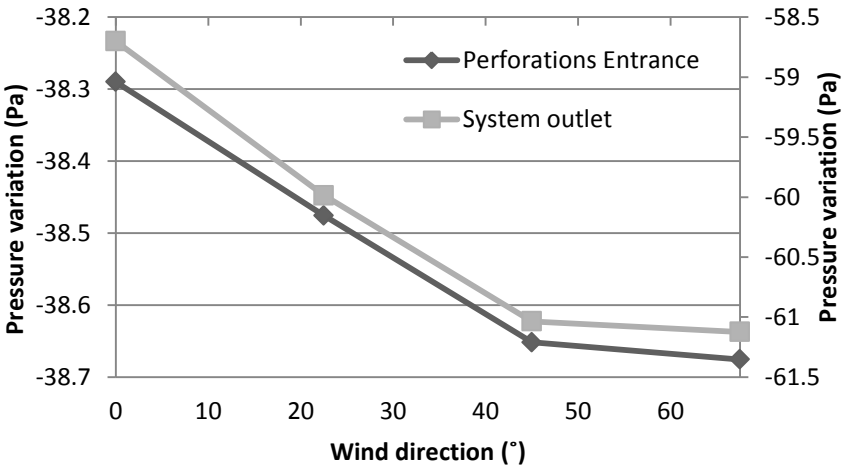

Figure 4-12. Pressure drop at the regions of perforations entrance and system outlet due to suction ratio variation from 0.004 to 0.010.

4.4 Effects of Wind Speed

CFD simulations were also carried out to investigate the parametric influence of wind speed on temperature rise, absorber surface temperature, effectiveness, and thermal efficiency. The details of the 40 cases studied in this section are listed in Table 4-2.

Figure. 4-13 shows the effects of wind speed on system operating temperatures at four different levels of suction ratio. As clear, both operating temperature tend to drastically reduce as wind speed increases. Increasing wind speed from 1 to 10 m/s leads to an average reduction in air 'temperature rise' and surface temperature of 81.6% and 45.6%, respectively. Surface temperature demonstrates an average decrease of about 1.55°C per 1 m/s increase in wind speed. This indicates that the rise in the wind speed increases the level of total heat taken away from the collector to the surrounding ambient air. Similarly, the air 'temperature rise' drops by an average of 1.65°C per 1 m/s increase in wind speed.

Likewise, over the full range of variation of wind speed, the average 'temperature rise' reduction goes from 17.6°C to 15°C as suction ratio increases from 0.004 to 0.010.This suggests that greater suction ratio may help to partially negating the significant effect of wind speed on temperature drop. While a lower suction ratio may be applied to the system to reach specific levels of temperature rise as wind speed grows, this increases the risk of reverse flow over the absorber plate.

Table 4-2. Details of the case studied for Wind speed and Suction ratio effect

Case number	Wind Direction (°)	Suction ratio V_s/U_∞	Ambient Air Temperature (°C)	Wind speed (m/s) U_∞	Solar Radiation (w/m2)
1	0	0.004	10	1	600
2				2	
3				3	
4				4	
5				5	
6				6	
7				7	
8				8	
9				9	
10				10	
11		0.006		1	
12				2	
13				3	
14				4	
15				5	
16				6	
17				7	
18				8	
19				9	
20				10	
21		0.008		1	
22				2	
23				3	
24				4	
25				5	
26				6	
27				7	
28				8	
29				9	
30				10	
31		0.01		1	
32				2	
33				3	
34				4	
35				5	
36				6	
37				7	
38				8	
39				9	
40				10	

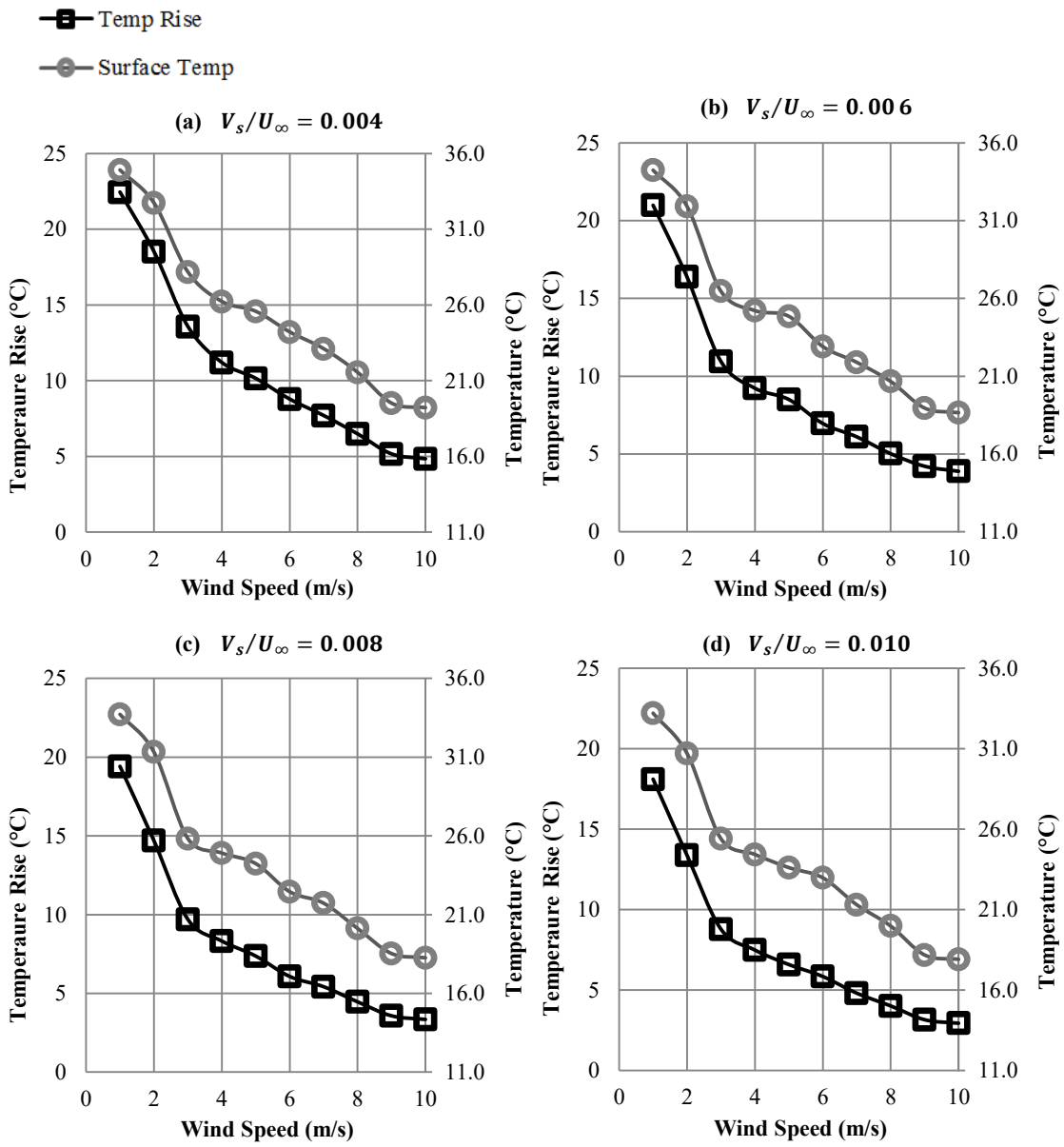

Figure. 4-13. Impact of wind speed on temperature rise and absorber surface temperature for: (a) $V_s/U_\infty = 0.004$, (b). $V_s/U_\infty = 0.006$, (c) $V_s/U_\infty = 0.008$, (d) $V_s/U_\infty = 0.010$.

Reverse flow mainly removes heat by taking the collected energy away from the absorber through the perforations (Gunnewiek, 2002). It is recommended to maintain the minimum pressure drop of 25 Pa across the absorber plate to avoid reverse flow in TSCs (Dymond and Kutscher, 1997).

The predicted levels pressure drop across the whole system for the 40 cases investigated in this section, are illustrated in Figure 4-14 to support an improved understanding of the thermal performance of the system. The corresponding levels of the averaged pressure at the perforations entrance (averaged over the perforations) is also reported in Figure 4-14.

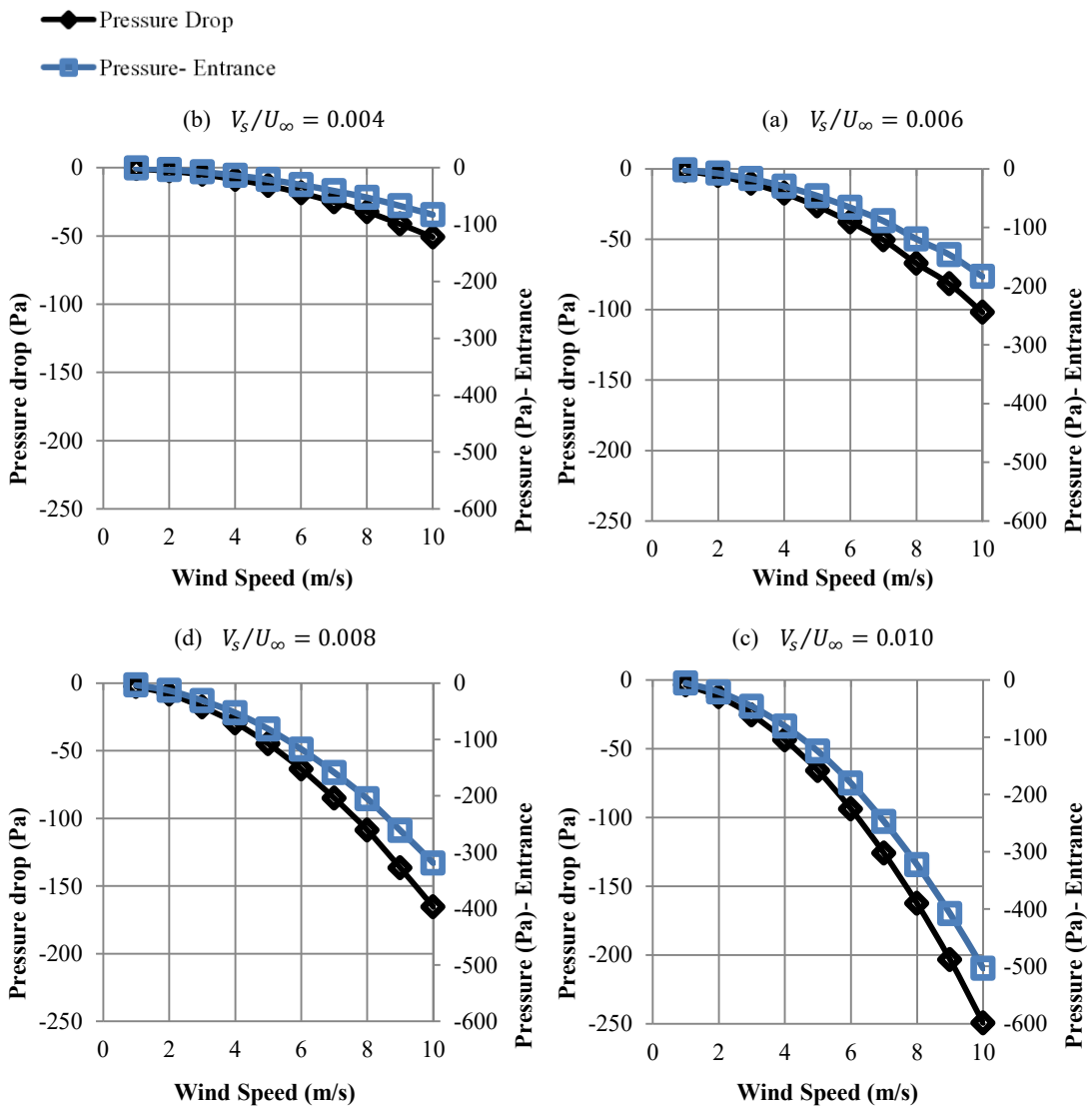

Figure 4-14. Impact of wind pseed on pressure drop across the system $(p_{out}-p_{in})$ and pressure at the entrance of perforations temperature for: (a) $V_s/U_\infty = 0.004$, (b). $V_s/U_\infty = 0.006$, (c) $V_s/U_\infty = 0.008$, (d) $V_s/U_\infty = 0.010$.

As can be seen in Figure 4-14, the pressure varies from strongly negative values towards zero as both wind speed and suction ratio decrease. Negative pressure values refer to the suction pressure taking place at the entrance of the perforations, which is counted as the inlet region of the TSC system. Positive pressure indicates that the system does not provide enough suction power to draw air into the plenum; thereby heated air is taken away by the external flow streaming over the plate. This implies that low suction ratio effectively leads to higher temperature rise, until reverse flow takes place. On the other hand, higher suction ratios support forced convection in the inner part, which may help delivering a higher amount of heat into the system, but at the same time provide relatively cooler air compared to the lower suction rates.

It's notable that the generated pressure drop increases more rapidly at lower wind speeds and suction ratios. The pressure drop shown in Figure 4-14 increases negatively showing a parabolic behaviour as a function of wind speed. This growth is more profound at higher suction ratios. The pressure drop variation is 5 Pa per 1 m/s increase in wind speed at the suction ratio of 0.004, whereas this value increases to about 24.6 at the suction ratio of 0.010. This explains why the largest temperature drop occurs at lower wind speeds (between 1 to 3 m/s, Figure. 4-13) indicating that the thermal performance of the TSC system encounters a greater level of resistance at higher wind speed, for each fixed value of suction ratio.

Growing pressure drop as expected correlates to the reducing operating temperatures. This is demonstrated in Figure 4-15, where air 'temperature rise' for the cases investigated in this section is plotted as a function of pressure drop at different values of suction ratio. It can be seen that the air 'temperature rise' gradient is higher at the lower pressure drop values associating with the lower levels of wind speed. Same scenario is referable for the suction ratio where higher suction ratios result in lower temperature gradients. It can be perceived from the results how the developed pressure drop increases the thermal resistance of the system.

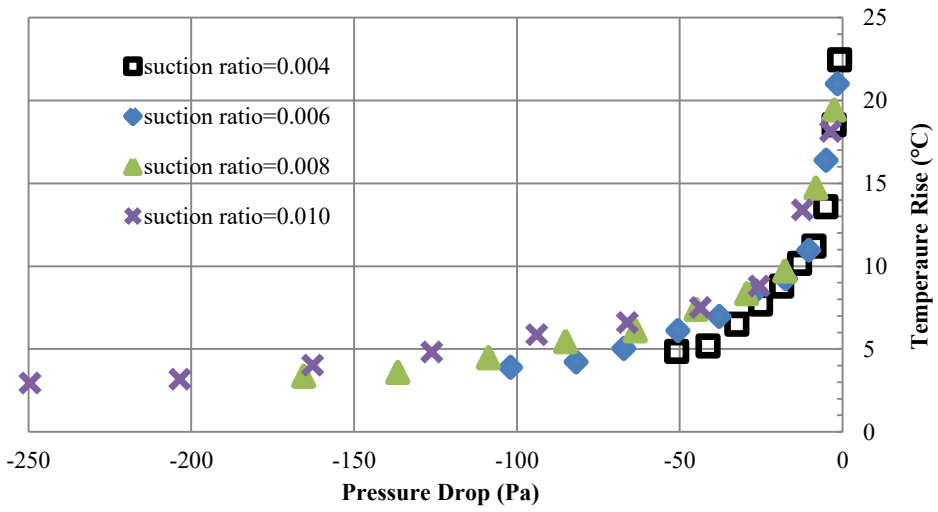

Figure 4-15. Temperature rise versus pressure drop at different suction ratios

Having established the role of pressure drop on the temperature levels, it is also worth noting the effect of the corresponding variation of suction velocity on pressure drop levels as was also discussed by Gunnewiek et al. (2002). The combination of suction ratio and wind speed levels determines the magnitude of suction velocity in this study. Therefore there are cases with different wind speeds and suction ratios which can have identical suction velocity; for instance: (I) U_∞=10 m/s, $V_s/U_\infty = 0.004$ and

(Π) U_∞=5 m/s, $V_s/U_\infty = 0.008$ which both have the suction velocity of 0.04 m/s. Similar to the pressure at the perforations entrance under equal suction velocities (Figure 4-14), the predicted pressure drop across the system ($p_{out} - p_{in}$), for case (I) with larger wind speed is greater (-50.9 Pa) than that of case (Π) (-44.9 Pa) which has the same suction velocity (0.04 m/s) but lower wind speed (Figure 4-14). This is due to the fact that whilst the suction velocity is held constant, the system has to generate a higher suction pressure in order to maintain the suction velocity against the increasing wind speeds. And this result is valid across the investigated cases (Table 4-3). The general relation between the suction velocity and the pressure drop for all the studied cases is demonstrated in Figure 4-16.

Table 4-3. Comparison of pressure drop magnitude across the system for the cases with similar suction velocities.

Suction velocity (m/s)	Corresponding combinations	Pressure drop (Pa)
0.080	U_∞=10, $V_s/U_\infty = 0.008$ U_∞=8, $V_s/U_\infty = 0.010$	-165.3 -163.6
0.060	U_∞=10, $V_s/U_\infty = 0.006$ U_∞=6, $V_s/U_\infty = 0.010$	-101.9 -93.8
0.048	U_∞=8, $V_s/U_\infty = 0.006$ U_∞=6, $V_s/U_\infty = 0.008$	-67.1 -63.5
0.040	U_∞=10, $V_s/U_\infty = 0.004$ U_∞=5, $V_s/U_\infty = 0.008$ U_∞=4, $V_s/U_\infty = 0.010$	-50.9 -44.9 -43.6
0.036	U_∞=9, $V_s/U_\infty = 0.004$ U_∞=6, $V_s/U_\infty = 0.006$	-41.2 -37.8
0.032	U_∞=8, $V_s/U_\infty = 0.004$ U_∞=4, $V_s/U_\infty = 0.008$	-32.3 -29.3
0.030	U_∞=5, $V_s/U_\infty = 0.006$ U_∞=3, $V_s/U_\infty = 0.010$	-26.6 -25.5
0.024	U_∞=6, $V_s/U_\infty = 0.004$ U_∞=4, $V_s/U_\infty = 0.006$ U_∞=3, $V_s/U_\infty = 0.008$	-18.6 -17.5 -17.4
0.020	U_∞=5, $V_s/U_\infty = 0.004$ U_∞=2, $V_s/U_\infty = 0.010$	-13.11 -12.22
0.016	U_∞=4, $V_s/U_\infty = 0.004$ U_∞=2, $V_s/U_\infty = 0.008$	-8.7 -8.1
0.012	U_∞=3, $V_s/U_\infty = 0.004$ U_∞=2, $V_s/U_\infty = 0.006$	-5.1 -5.0
0.008	U_∞=2, $V_s/U_\infty = 0.004$ U_∞=1, $V_s/U_\infty = 0.008$	-2.5 -1.6

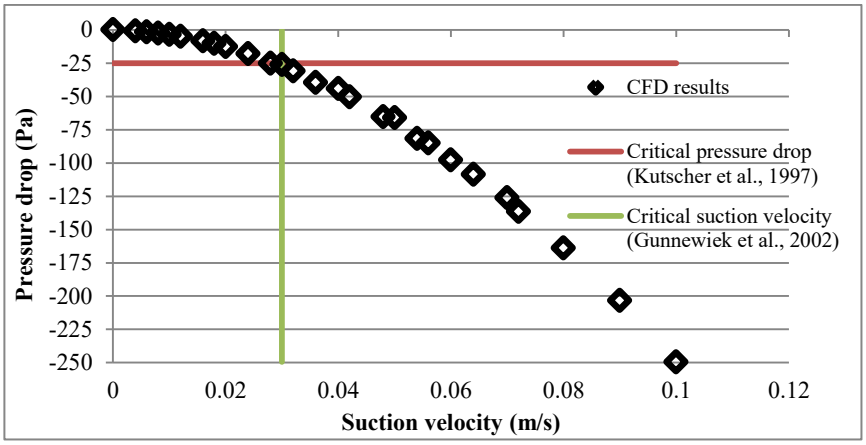

Figure 4-16. Pressure drop as a function of suction velocity presented with the recommended values of suction velocity and pressure drop to avoid reverse flow.

It can be found from Table 4-3 that the impact of wind speed on 'pressure drop' is slightly different than that of suction ratio, hence the presented pressure drop in Figure 4-16, are the averaged values.

Having plotted the combined impact of suction ratio and wind speed, it can also be deduced from the table and the graph that the suction velocity of 0.030 m/s associates with the 25 Pa critical pressure drop (Dymond and Kutscher 1997). This is exactly the minimum suction velocity recommended by Gunnewiek et al. (2002) to avoid reverse flow (averaged over) depending on the buildings shape.

The contribution of each of the three different system parts to the final air 'temperature rise' is demonstrated in Figure 4-17. The proportion of the temperature rise delivered by each region is equivalent to the ratio of their effectiveness contribution to the overall system effectiveness:

$$\frac{\Delta T_{zone}}{T_{out} - T_{amb}} = \frac{\frac{\Delta T_{zone}}{T_s - T_{amb}}}{\frac{T_{out} - T_{amb}}{T_s - T_{amb}}} = \frac{HEE_{zone}}{\mathrm{HEE}} \qquad (4\text{-}1)$$

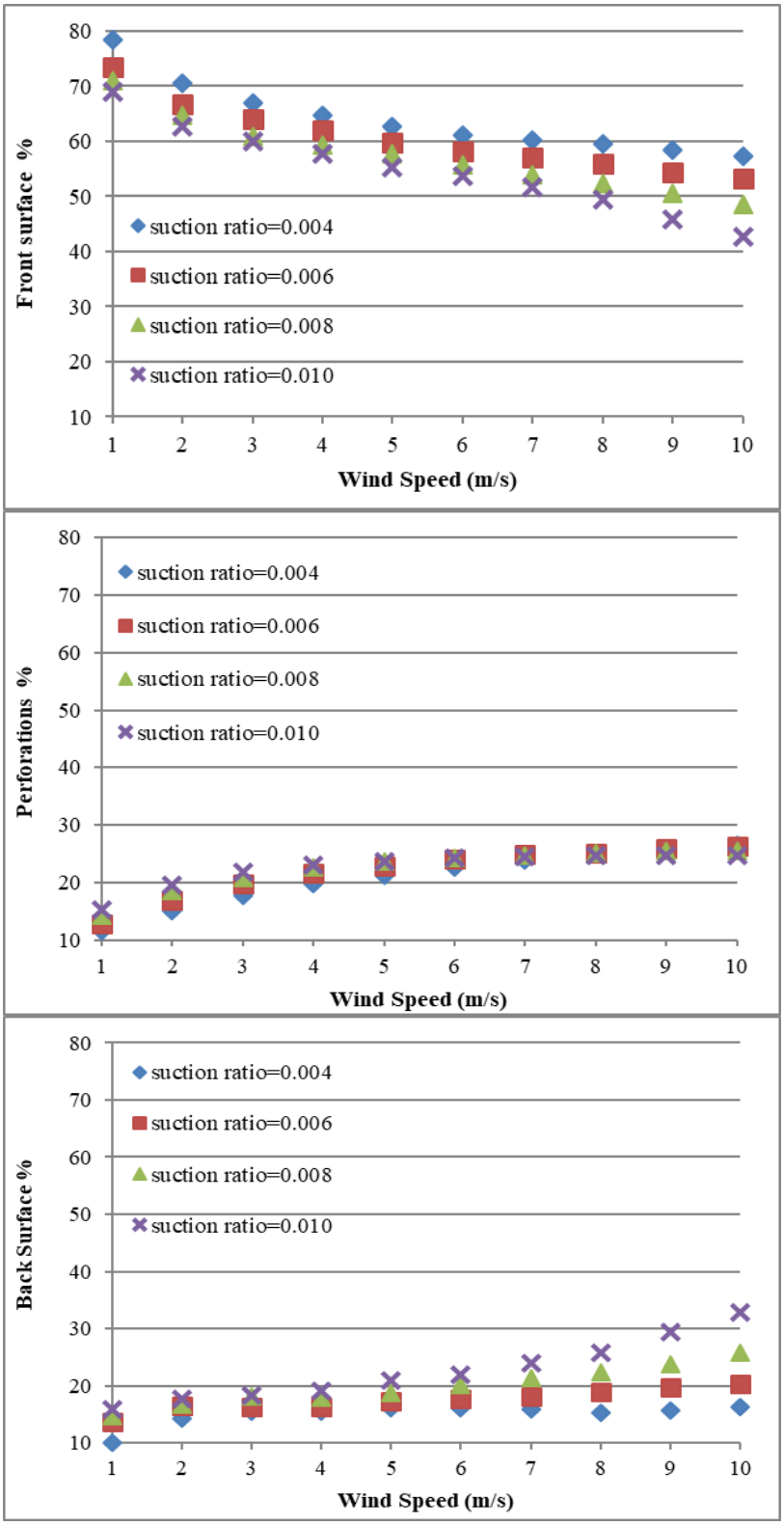

Figure 4-17. Contribution of each part of the system to the final HEE.

It's demonstrated that the front surface has the greatest contribution to the final temperature rise but the contribution lessens as the wind speed increases. Back surface and perforations regions , however, have depicted smaller contributions compared to the front surface yet gain more crucial role as wind speed increases. The same trend is noticable in suction ratio variation where the fornt surface and back

surface demonstrate compeltely contarary reaction against suction ratio. Proportions of heat trasnfer from the front surface diminishes as suction ratio increases whereas the back surface shows greater contribution against the increasing suction ratio. This trend is in agreement with the study carried out by Badache et al. (2013). Thus, the contribution of the front surface decreases as the pressure drop rises, whereas this effect is shown to be opposite for the back surface region. Pressure drop develeopes its negative effect towards the perforations region as both wind speed and suction ratio increase . Proportion of the heat exchange from the perforations increases with suction ratios until wind speed reaches around 7 m/s at which a tail-off can be observed for the suction ratios of 0.008 and 0.010. The tail-off coinsides with the significant raise in the proportion of the exchanged heat by the back surface (Figure 4-17).

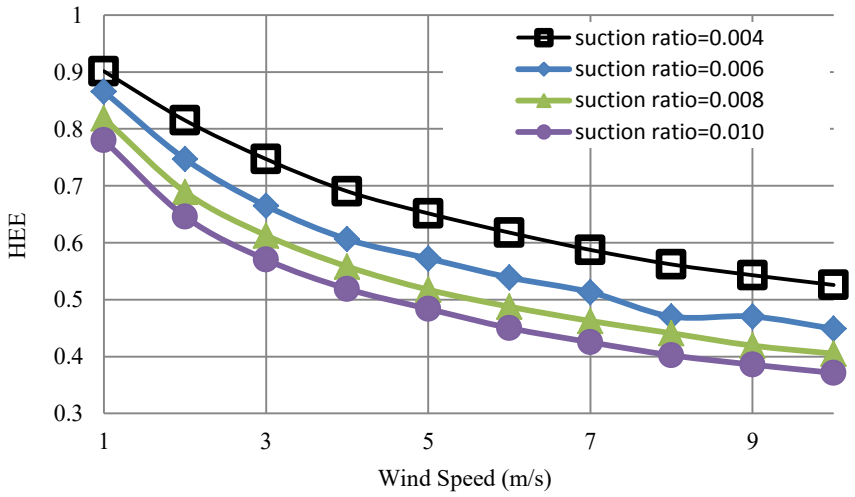

Figure 4-18 . Impact of wind speed on heat exchange effectiveness for: $V_s/U_\infty = 0.004$, $V_s/U_\infty = 0.006$, $V_s/U_\infty = 0.008$, and $V_s/U_\infty = 0.010$.

The overall variation of HEE as a function of wind speed, for different levels of suction ratio is presented in Figure 4-18 . HEE decreases considerably with both wind speed and suction ratio, over a wide range between 0.9 and 0.37. Changing suction ratio from 0.004 to 0.01 causes HEE to reduce by about 29.3% at the wind speed of 10 m/s and 13.7% at the wind speed of 1 m/s. This could be due to the greater pressure drop occurring at larger wind speeds.

HEE reduction is shown to be proportional to wind speed (Figure. 4-19). The rapid change in the operating temperatures and pressure drop at the lower wind speed values is also noticeable in HEE drop which is found to be due to the significant drop in the 'temperature rise' originating from the front surface at the very low wind speeds (Figure 4-17). Increasing wind speed between 1 and 10 m/s changes HEE by about 52.3% at suction ratio of 0.01 and once the suction ratio decreases to 0.004, the same variation in wind speed causes a 41.8% reduction in HEE. Effect of pressure drop again can be seen here. Hence the

highest value of HEE is predicted to take place at the lowest levels of wind speed and suction ratio being associated with the lowest pressure drop.

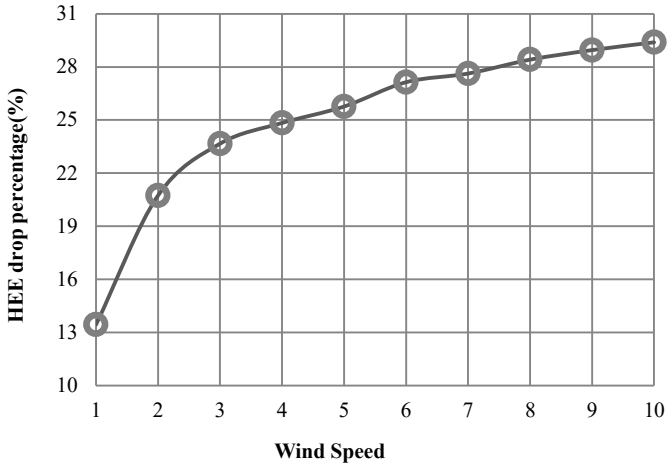

Figure. 4-19. HEE drop due to the increasing suction ratio from 0.004 to 0.01 at different wind speeds.

Low suction ratio not only may cause reverse flow to happen along the external surface of the collector but also delivers low mass flow rate and subsequently less amount of heat to the building. Thermal efficiency of TSCs at different suction ratios along with various wind speeds is illustrated in Figure. 4-20. Whilst the intensity of the solar radiation falling on the external side of the collector is fixed for all the studied cases, the rise and drop of the predicted thermal efficiency is merely due to mass flow rate and the corresponding temperature rise (Eq. 2-44). Since mass flow rate is proportional to the suction velocity[4], the value increases both with increasing suction ratio and wind speed. The graph implies that regardless of the reducing 'temperature rise', along with increasing wind speed and suction ratio, the amount of heat captured by the collector increases and is dominated by mass flow rate (Figure. 4-20). However, the captured heat would be a low grade one as the outlet temperature decreases with increasing suction flow rate.

A general trend of thermal efficiency against wind speed can be perceived from the graphs. It can be seen that the thermal efficiency increases as wind speed ascents towards a noticeable turning point at which thermal efficiency drops down. In other words, the effect of mass flow rate is dominant until wind speed approaches 7 m/s where the system's heat loss becomes more pronounced. Alternatively stated, the growth in mass flow rate is less than the drop in temperature rise as wind speed grows. However, this phenomenon hasn't been witnessed for suction ratio and increasing suction ratio at a fixed wind speed has

[4] $\dot{m} = \rho A V_s$

consistently enhanced the thermal efficiency. This implies that the trend gets complicated once both suction velocity and wind speed increases. Thereby, as mentioned in the current section earlier, suction ratio is a term representing both external and internal characteristics. Although pressure drop due to suction power keeps rising with increasing suction ratio, wind speed dictates its negative effect on thermal efficiency at higher levels. In other words, higher suction velocity and corresponding pressure drop do not always indicate the increasing thermal efficiency of TSCs.

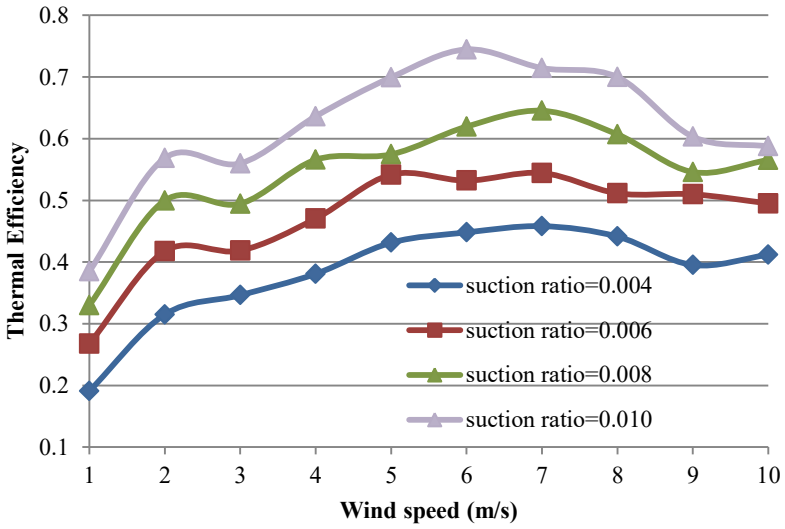

Figure. 4-20. Impact of wind speed on thermal efficiency for different suction ratios.

Figure. 4-21 shows the wind speed-averaged values of thermal efficiency and temperature rise at different suction ratios. In spite of downgrading effect of suction ratio ,and subsequently mass flow rate, on the temperature rise, it generally shows a positive impact on thermal efficiency (Figure. 4-21). It is shown that 0.006 suction ratio could be the optimum point for the studied cases in terms of both temperature rise and thermal efficiency. It means that the highest thermal efficiency achievable at the highest temperature rise occurs at 0.006 suction ratio.

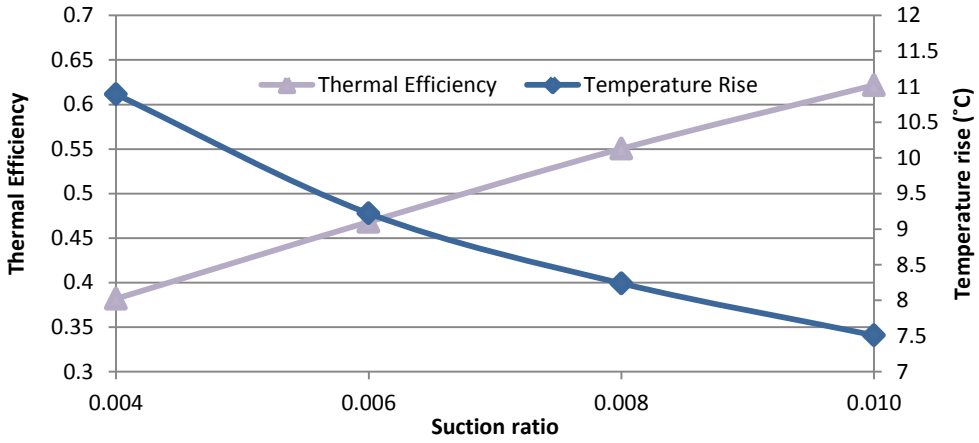

Figure 4-21. Impact of wind speed-averaged suction ratio on thermal efficiency and temperature rise.

4.5 Effect of Solar Radiation

Solar radiation drives the heating process of the absorber plate thus exploring its influence using CFD simulations is particularly useful for practical applications of TSC systems. In this section, three realistic values of solar radiation intensity have been adopted from the available recorded data (Hall et al., 2014) to predict the thermal response of the system at fixed wind speed of 3 m/s, wind angle of $\beta = 0^{\circ}$, suction ratio of 0.008 and ambient air temperature of 10° C. The results of this parametric study are presented in Figure 4-22.

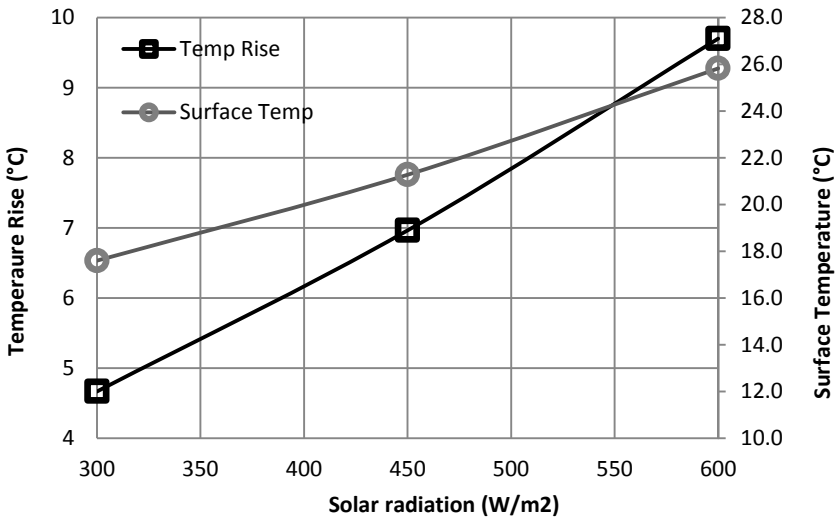

Figure 4-22. Impact of solar radiation on temperature rise and absorber surface temperature.

As expected (Chan et al., 2013), both 'surface temperature' and air 'temperature rise' increase with the increasing solar radiation. The variation is linear in both cases – a change in solar radiation from 300 to 600 W/m^2 raises the system surface temperature from 17.6 to 25.8 °C, or by about 47%; the effect is greater on air temperature rise, which is increased from 4.67 to 9.7 °C, i.e. by 107%.

The predicted levels of effectiveness (see Figure 4-23) show negligible variation with increasing solar radiation; the average HEE value is predicted to be 0.614. This suggests that the ability of the system to exchange the absorbed thermal energy is virtually independent of the input solar energy. This is in agreement with the literature defining effectiveness only as a function of flow and material properties (Kutscher, 1992; Van Decker, 2001).

Solar radiation intensity demonstrates also a negligible impact on system thermal efficiency (Figure 4-23). This suggests that, not only the system transfers heat from the absorber plate to the outlet at a constant rate regardless of the solar radiation input, but also the rate of heat loss at the front surface of the absorber is approximately constant. This behaviour is in agreement with the study of Leon and Kumar (2007).

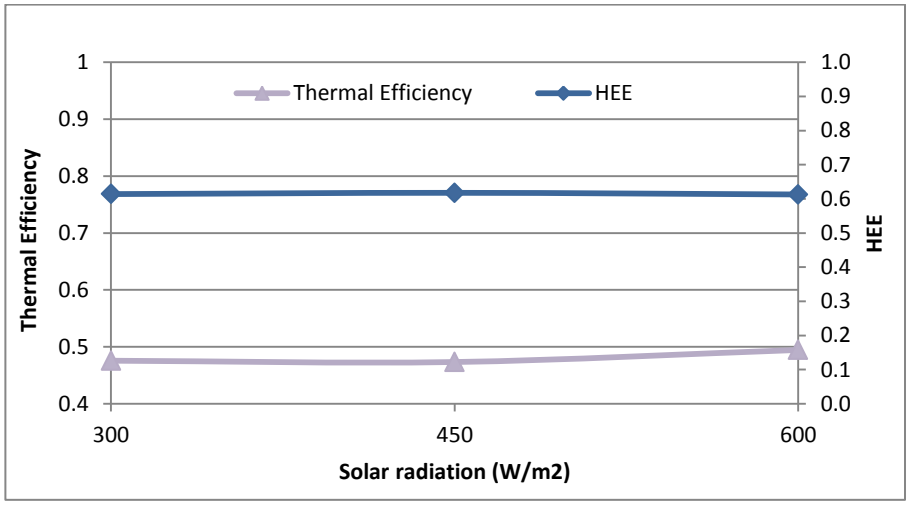

Figure 4-23.Impact of solar radiation on temperature rise and absorber surface temperature for $\beta = 0^{\circ}$.

4.6 Effect of 'Time of The Day'

The absorber plate receives solar radiation at different angles depending on 'time of the day', and hence sun angle. The Star-CCM+ CFD package features a 'Solar Load' sub-model, which provides the ability to investigate system performance at prescribed times and locations. The simulations for this

specific investigation refer to the 22nd of December, and use the location of the measurement site indicated in the 'Background' Section. 22nd of December is chosen as the representative day amongst the days that the weather data was monitored and also were available from the tests conducted at Oxford Brookes University (Hall et al., 2014).

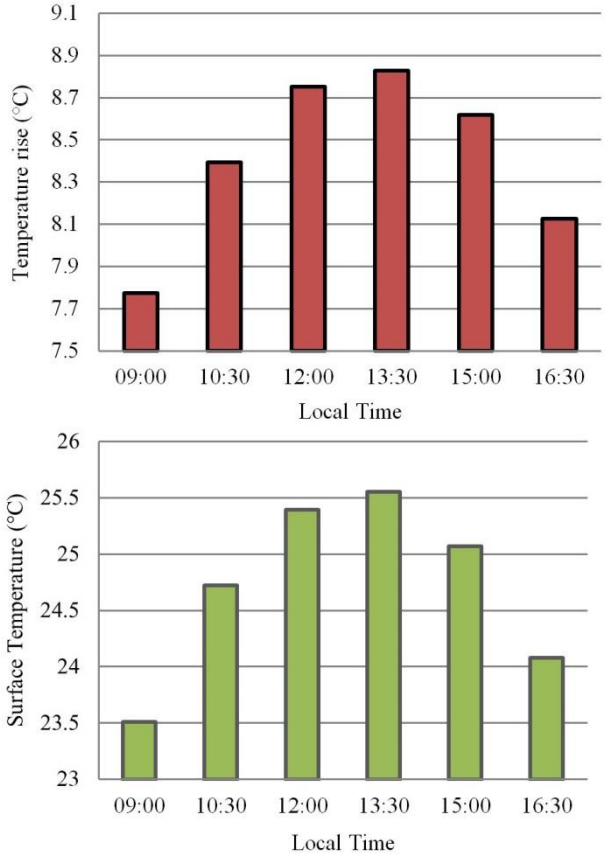

Figure 4-24. Impact of day time on temperature rise and absorber surface temperature.

Six different times were considered, whilst other variables were kept constant as follows: solar radiation, 600 W/m^2 with clear sky; wind angle $\beta = 0°$; wind speed, 3 m/s; suction ratio, 0.010. The results are displayed in Figure 4-24. Both temperature rise and surface temperature increase from the morning until early afternoon, before reducing later in the afternoon when the sun drops. The temperature variations are merely due to solar angularity as the simulations have been performed at constant solar radiation intensity. Therefore the trend would be different for the early morning and late afternoon intervals, when the solar intensity is significantly less than mid-day time. The results imply that TSCs are able to deliver a reasonable air temperature into buildings around noon although heat is mostly required in the early morning and late afternoon/evening. Heat storage systems are likely to be highly beneficial if TSCs are to be fully optimised against the heating demands of common building types and normal occupancy patterns. This result then can be employed to predict the deliverable temperature levels based

on the actual ambient air temperature (Figure 4-25). The ambient air temperature data is taken from Hall et al., (2014) for 22nd December.

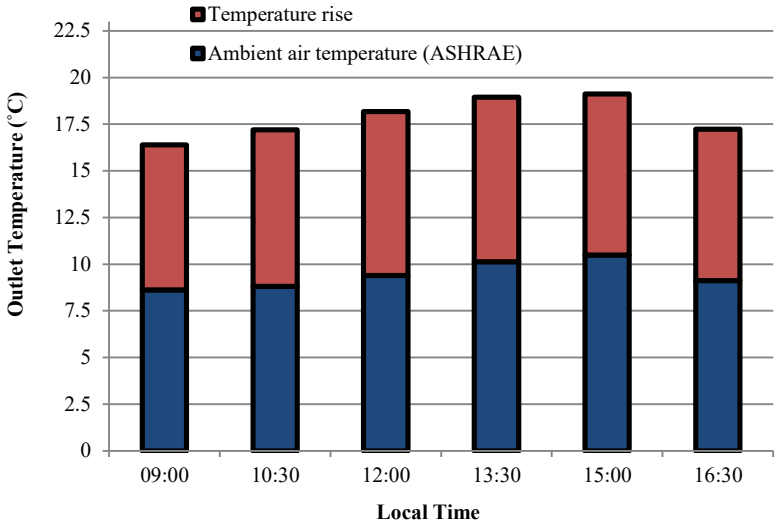

Figure 4-25. Deliverable temperature of the TSC predicted for 22nd December based on the modelled temperature rise.

It can be seen that only solar angularity can cause a 3˚C difference between the deliverable temperatures at 15:00 and 9:00 which is perfectly captured using this CFD model. There seems to be a potential for a time-dependent study of the system to demonstrate the build-up temperature during a day. This can be part of a future study.

Variation of thermal efficiency and HEE are shown in Figure 4-26. Since the solar radiation is fixed, thermal efficiency changes proportionally with the temperature rise where similar behaviour can be seen in Figure 4-26. Effectiveness however is a function of both air 'temperature rise' and absorber 'surface temperature' where both have demonstrated a similar behaviour resulting in almost a constant effectiveness during the day. Hence hitherto, it can be perceived that the effectiveness of the system is almost independent of both solar radiation and angularity but is affected by the cross flow and internal flow.

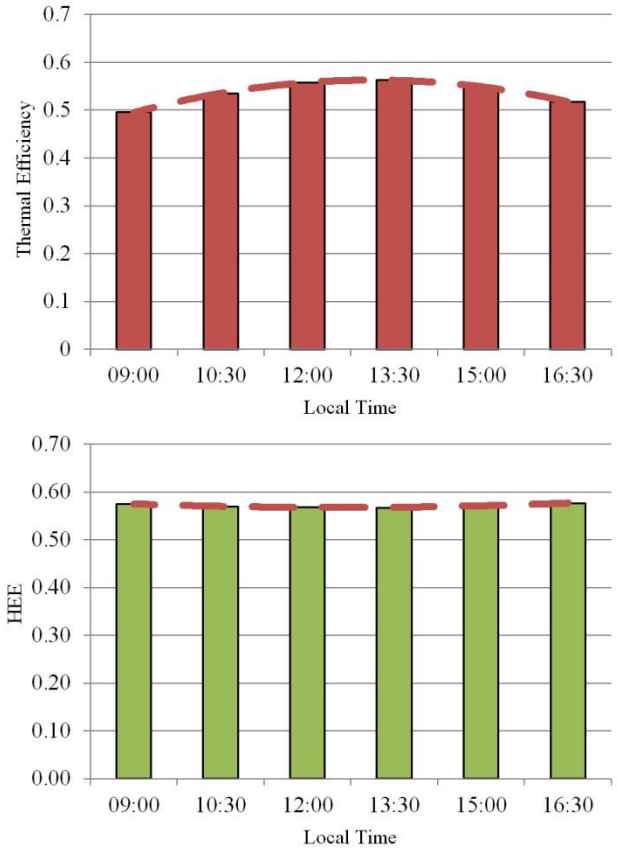

Figure 4-26. Impact of day time (sun position) on thermal efficiency and HEE

4.7 Effect of Plenum Depth

TSCs with four different plenum depths have been modelled to investigate the effect of plenum depth on system thermal performance. The details of the studied cases are listed in Table 4-4. The absorber plate temperature and air temperature rise versus plenum depth, at three different of wind speeds are presented in Figure 4-27. Since the size of the plenum is expected to affect mostly the internal flow, wind speed as the only flow characteristics of the external flow variable was chosen to vary in order to explore the effects of the interaction between internal and external variables on system thermal performance.

Table 4-4. Details of the case studied for plenum depth effect

Ambient air temperature (°C)	Wind Direction (°) β	Suction ratio V_s/U_∞	Solar radiation (w/m2)	Wind speed (m/s) U_∞	Plenum depth (mm)
10	0	0.008	600	3	60
					80
					100
					120
				5	60
					80
					100
					120
				7	60
					80
					100
					120

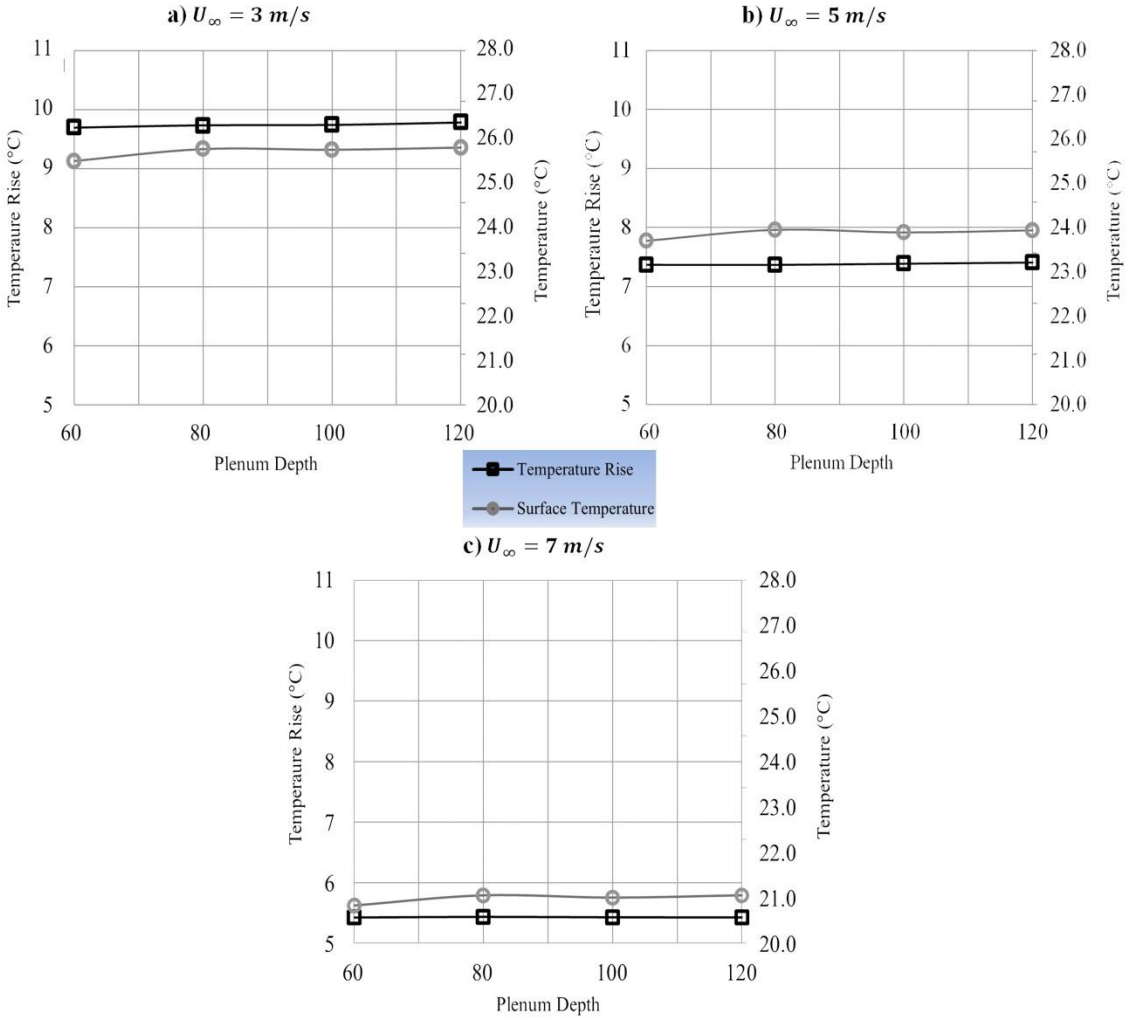

Figure 4-27. Impact of plenum depth on temperature rise and absorber surface temperature for a) $U_\infty = 3\ m/s$, b) $U_\infty = 5\ m/s$, c) $U_\infty = 7\ m/s$.

The results suggest that plenum depth doesn't affect the thermal performance of TSCs significantly. At a wind speed of 3 m/s, as plenum depth increases from 60 mm to 120 mm, the air temperature rise varies only between 9.7℃ and 9.78℃, i.e. in the range of possible numerical errors. Similarly, surface temperature demonstrates a negligible overall variation, and an oscillating trend around an average of 27.5℃. The predicted air 'temperature rise' at 5 and 7 m/s wind speed is again approximately constant, i.e. independent of plenum depth. The average values are 7.5 and 6.1℃ at 5 and 7 m/s, respectively. Similar considerations can be drawn on the variation of surface temperature, which demonstrates very mild and inconsistent influence from plenum depth, again well within possible simulation numerical error.

The corresponding overall pressure drop across the system is presented in Figure 4-28. Similarly, to system temperatures, the variation of plenum depth exerts negligible influence on the pressure drop. The system experiences a 6.6% increase in pressure drop along the plenum depth variation, at the wind speed of 3 m/s. This is reduced to about 2.8% and 2.44%, for the wind speeds of 5 and 7 m/s, respectively. As expected, the effect of internal parameters reduces as external variable wind speed increases.

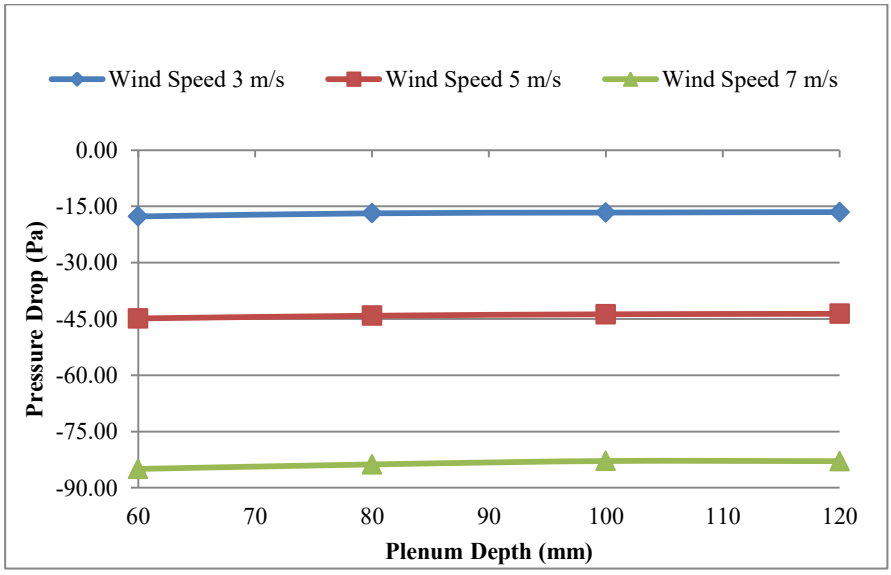

Figure 4-28. Pressure drop across the system $(p_{in}-p_{out})$.

Figure. 4-29 shows overall system HEE for all cases investigated in this section. Generally, HEE and thermal efficiency are not expected to be affected by increasing plenum depth (Badache et al., 2013).

HEE stays almost constant; plenum thickness however changes the heat transfer pattern associated with each region, i.e. front surface, perforations and back surface of the plate. Whilst Badache et al. (2013) reported that different suction velocity affects the contribution of each region's contribution to the overall heat transfer with various plenum widths, similar results can be drawn from the CFD simulations (Figure 4-30). This relationship however has not been found consistent across the plenum depth variation. Although this study has considered a wider range of plenum depth variation compared to Badache et al. (2013), a more statistical approach seems compelling on this subject for future research.

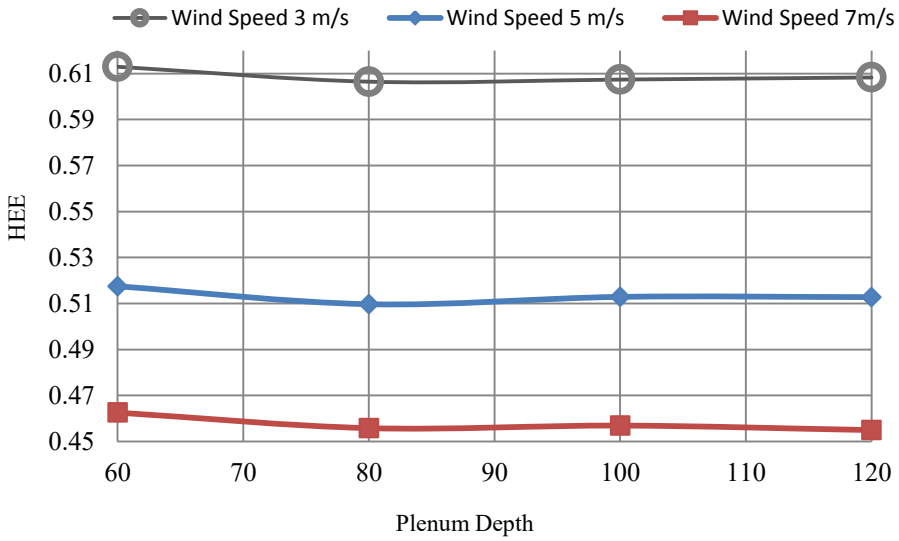

Figure. 4-29. Impact of plenum depth on Heat Exchange Effectiveness (HEE) for $U_\infty = 3\ m/s$, $U_\infty = 5\ m/s$, and $U_\infty = 7\ m/s$.

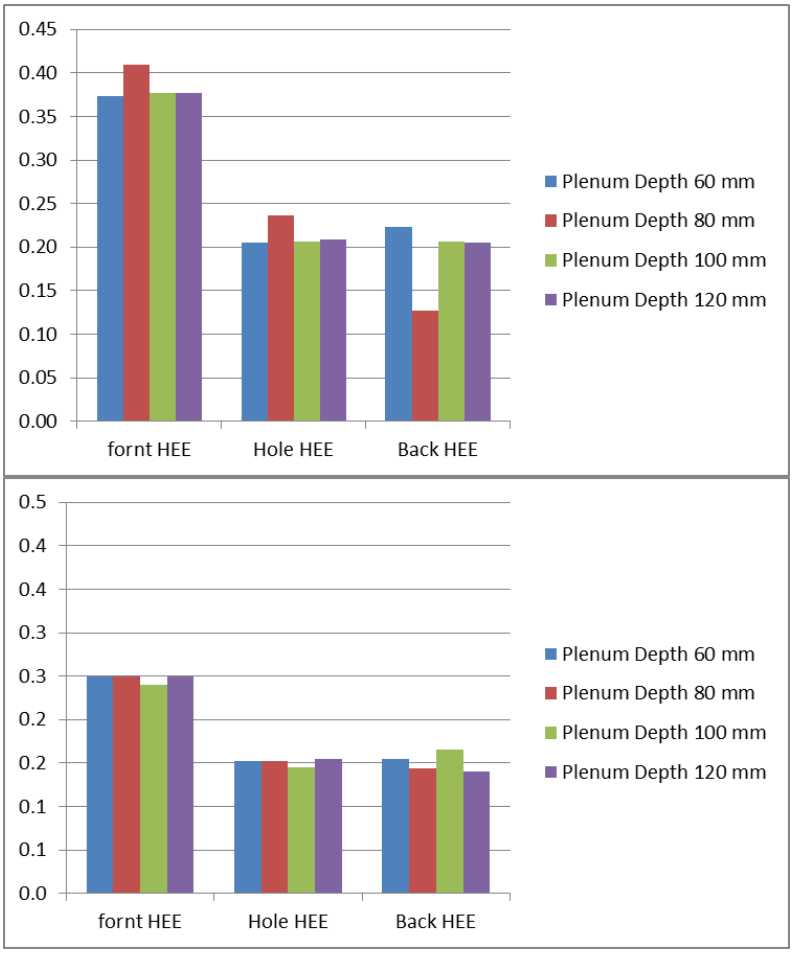

Figure 4-30. Impact of plenum depth on Heat Exchange Effectiveness contributed by front, perforations and back of the plate region against the wind speed of (a) 3 m/s and (b) 7 m/s.

Since mass flow rate has a constant value in all cases, the thermal efficiency is proportional to, and expected to follow similar trend as, air temperature. As shown in Figure. 4-31, thermal efficiency is only slightly influenced by the increasing plenum depth, showing an average value of 0.5 at 3 m/s, and increasing to 0.63 and 0.65 at 5 and 7 m/s, respectively.

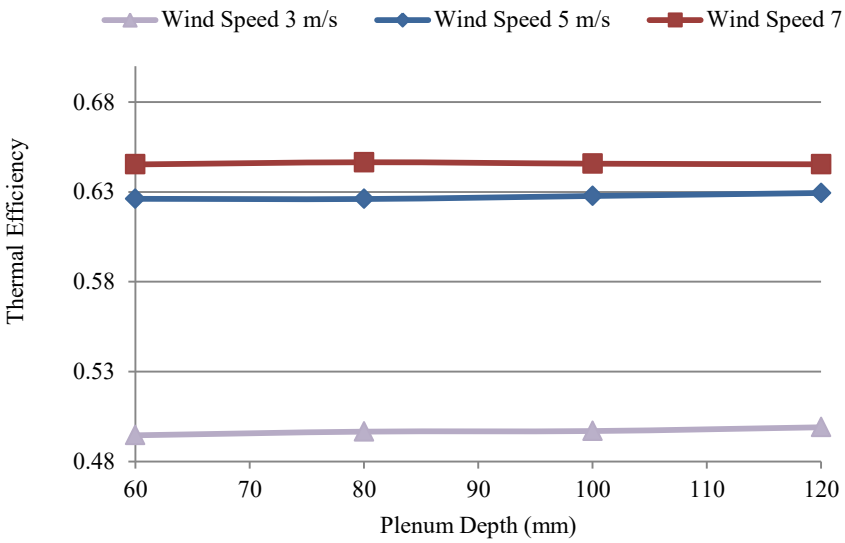

Figure. 4-31. Impact of plenum depth on the thermal efficiency for: a) $U_\infty = 3\ m/s$, b) $U_\infty = 5\ m/s$, c) $U_\infty = 7\ m/s$.

4.8 Effect of Absorber Plate's Thermal Conductivity

Heat transfer rate is a crucial characteristic for all heat exchangers, including TSCs. The amount of captured heat is highly dependent on how fast the heat exchange takes place in different parts of the system. Low rates of heat exchange can lead to high levels of heat loss. Thermal conductivity is a measure of the ability of a material to conduct heat. Heat transfer occurs at a higher rate across materials with high thermal conductivity. A greater thermal conductivity for the absorber plate may lead to: a) faster heat conduction to the back of the plate, enabling stronger heat exchange with the airflow inside the plenum; and b) larger heat collection capacity, as it enhances the 'absorption and release' rate of thermal energy in the absorber plate.

A limited set of steady-state simulations have been performed to demonstrate the parametric influence of absorber plate's thermal conductivity, on system performance. As shown in Table 4-5, five levels of conductivity were investigated, while all other geometry and operating parameters were kept constant. For this study, the solar radiation was given a level of 705.8 W/m2, which corresponds to one of the experimental test points (Hall et al., 2014). This level of solar radiation intensity was chosen to better highlight the impact of thermal conductivity.

Table 4-5. Details of the case studied for the effect of absorber plate's thermal conductivity

Material	Thermal Conductivity $(W/m\,K)$ k	Specific Heat Capacity $(J/kg\,K)$ c_p	Thermal Diffusivity (m^2/s)	Plenum depth (mm)	Ambient Air Temperature (°C)	Wind speed (m/s) U_∞	Wind Direction (°) β	Suction ratio V_s/U_∞	Solar Radiation (w/m2)
Stainless Steel	16	480	4.1E-06	60	10	5	0	0.008	705.8
Ordinary Steel	57	490	1.5E-05						
Aluminium	205	910	8.3E-05						
Copper	398	386	1.1E-4						
Silver	429	230	1.7E-4						

The parametric variation of air 'temperature rise' and absorber surface temperature as a function of thermal conductivity is presented in Figure. 4-32; It is clear that both temperatures increase quite steeply with increasing thermal conductivity, with the variation highly biased towards the lower conductivity ranges. Over its entire range of variation of thermal conductivity, from 16 to 429 W/m K, surface temperature increases from 25.28℃ to 27.68℃, which is about 9.5%. The growth is predicted to be about 21.2% for the air temperature rise. The effect of thermal conductivity is much more pronounced over its lower range, up to about 205 W/mK, while no significant effect on system temperatures is recorded for thermal conductivity in excess of this value. The reason could be hidden in the fact that high conductive materials possess low specific heat capacity. Specific heat capacity is the amount of heat required to change an object's temperature by one degree.

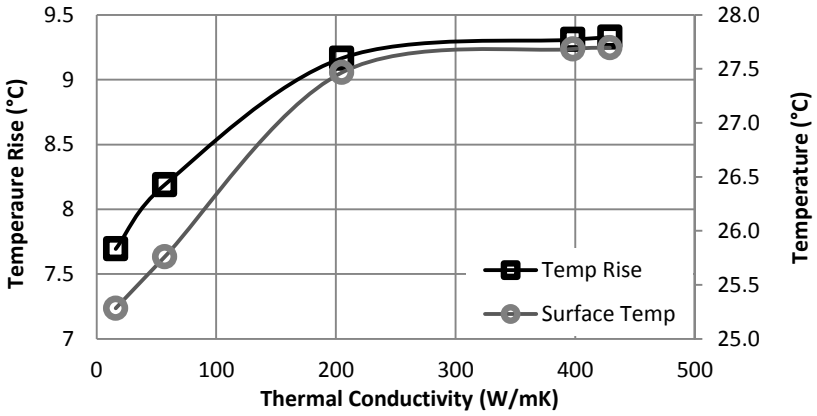

Figure. 4-32. Impact of thermal conductivity of absorber plate on temperature rise and absorber surface temperature.

The combined effect of thermal conductivity and specific heat capacity is embedded in thermal diffusivity of each material defined as: $\alpha = k/\rho c_p$. Thermal diffusivity is a measure of the ability of a material to conduct thermal energy relative to its ability to store thermal energy. Logarithm scale is useful to present the results in a relative manner. Figure 4-33 shows how the 'temperature rise' and absorber 'surface temperature' change regarding the relative increment of thermal diffusivity and conductivity. It can be seen in Figure 4-33 that small growth of temperature beyond aluminium is more dominated by the thermal diffusivity rather than the thermal conductivity and a larger variation of thermal conductivity has not increased the temperature proportionally. In fact, it can be seen that logarithmic values of copper and silver thermal conductivity are almost equal but due to lower heat capacity of silver it has been able to deliver a slightly higher operating temperatures.

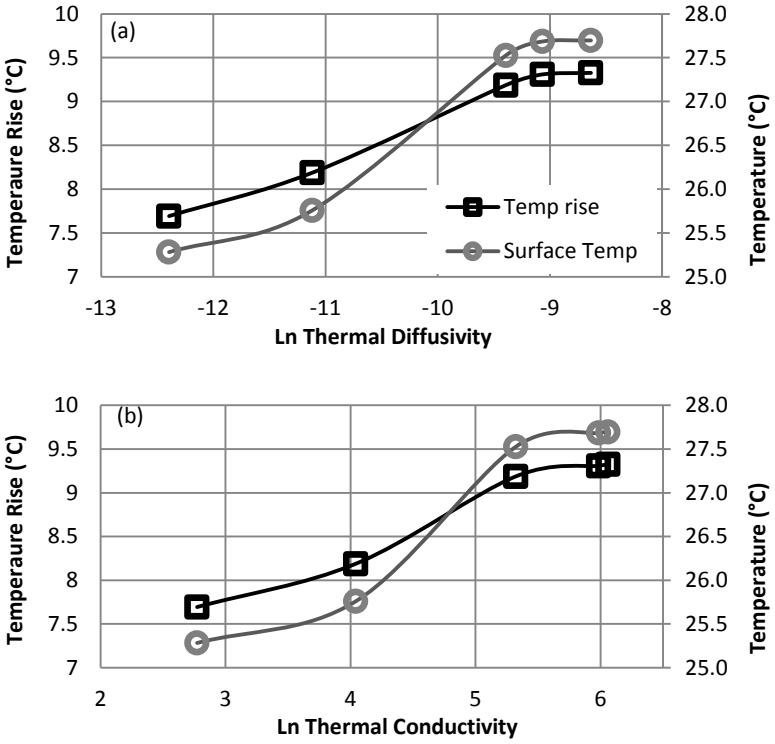

Figure 4-33. Variation of operating temperatures versus relative variation growth of (a) thermal diffusivity and (b) thermal conductivity in the form of natural logarithm.

The heat exchange effectiveness follows a similar trend as the operating temperatures (Figure. 4-34). Increasing thermal conductivity from 16 to 429 W/mK improves the effectiveness by about 4.7%.

As shown in Figure 4-35, the impact of thermal conductivity on thermal efficiency is estimated to be more significant than that on HEE. Increasing thermal conductivity from 16 to 429 W/mK raises the thermal efficiency by about 21.2%, between 0.56 and 0.675. It should be noted that, although silver is not an appropriate material for TSC applications, it has been considered here for research purposes, as an example of highly conductive material. Importantly, all materials with thermal conductivity of 205 W/mk and above (including aluminum and copper), show similar thermal behaviour, and their use would lead to similar improvements as silver. In fact, all performance parameters considered here demonstrate reduced gains for thermal conductivity above the 205 W/mk mark. The analysis suggests this is due to the lower heat capacity of highly conductive materials such as copper and silver. Lower heat capacity of copper and silver negates their high conduction capability to some extent which leads to the excessive heat being taken away by the external streaming flow easier compared to the materials with higher heat capacity. This study implies that aluminium would be an optimum material for TSC applications.

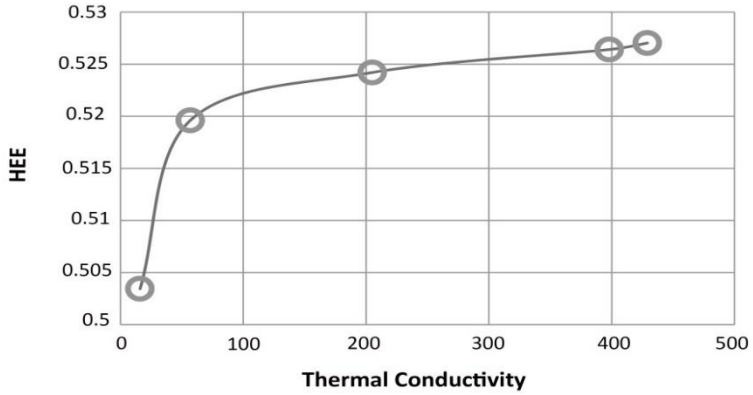

Figure 4-34. Impact of thermal conductivity of absorber plate on heat exchange effectiveness.

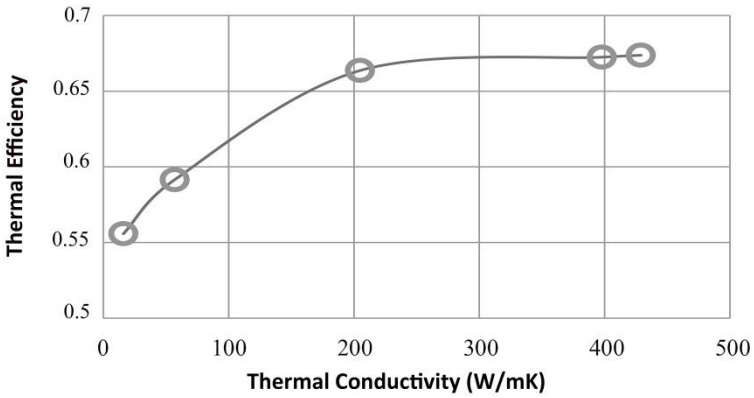

Figure 4-35. Impact of thermal conductivity of absorber plate on heat exchange effectiveness

4.9 Statistical Analysis and Optimisation

As discussed in Chapter 3, statistical and optimisation techniques have been applied to optimise the geometry of the absorber plate, considering the combined effects of three factor variables: plate thickness, diameter of perforations and the pitch distance between perforations. A large number of computer simulations were carried out based on a DoE which had been built using the Halton Sequence space filling approach. The results were then to create a statistical model for the response variable (HEE); this enables identifying an optimal geometry specification for the absorber plate, as well as developing a correlation to calculate its effectiveness for arbitrary combinations of the factor variables. The use of different regression models with increasing level of complication was investigated.

The geometry optimisation exercise was carried out in stages, increasing the sample population where necessary, to increase the accuracy of the model in specific problematic areas, and to enhance the model ability to describe the expected physical behaviour. The original DoE database, including the added corner points, incorporated 30 different geometrical configurations (Figure 4-36). The optimisation operated using this initial set showed that the optimal solution would lie around one corner – indicated as point A in Figure 4-36, irrespective of the regression model used. This result is in agreement with Van Decker et al. (2001) and Leon et al. (2007) which shows how highest values of HEE correspond to the lowest levels of pitch and hole diameter. The effect of plate thickness however opposes the presence of a proportional correlation between the effectiveness and the plate thickness (Van Decker et al., 2001; Arulananadam et al., 2000). However, to the Author's best knowledge, no geometrical optimisation studies have been carried out using a 3-D CFD model considering all effective parameters on the combined effect of diameter, pitch and thickness.

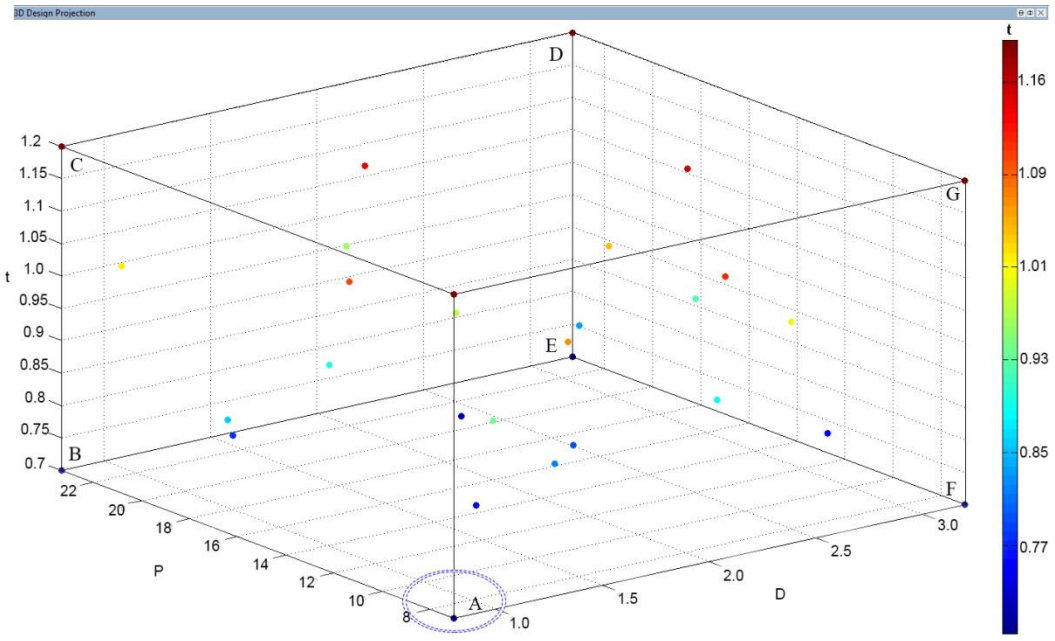

Figure 4-36. 3-D view of the DoE

In order to obtain increased accuracy around the initial solution, six extra points/geometrical configurations were added around A (see Table 4-6) and the corresponding simulations carried out. Figure 4-37 shows the HEE response lines obtained for the three regression models, respectively quadratic, cubic, and quartic. Each response line is obtained by fixing two factor variables at their optimal level, and allowing the remaining one to vary within the interval of interest.

Table 4-6. Details of the added points about the projected optimised region.

Points	D (mm)	P (mm)	t (mm)
31	0.8	8.63	0.7
32	0.8	8.63	0.75
33	1.04	8.63	0.75
34	1.04	7	0.75
35	1.04	7	0.7
36	1.04	8.63	0.7

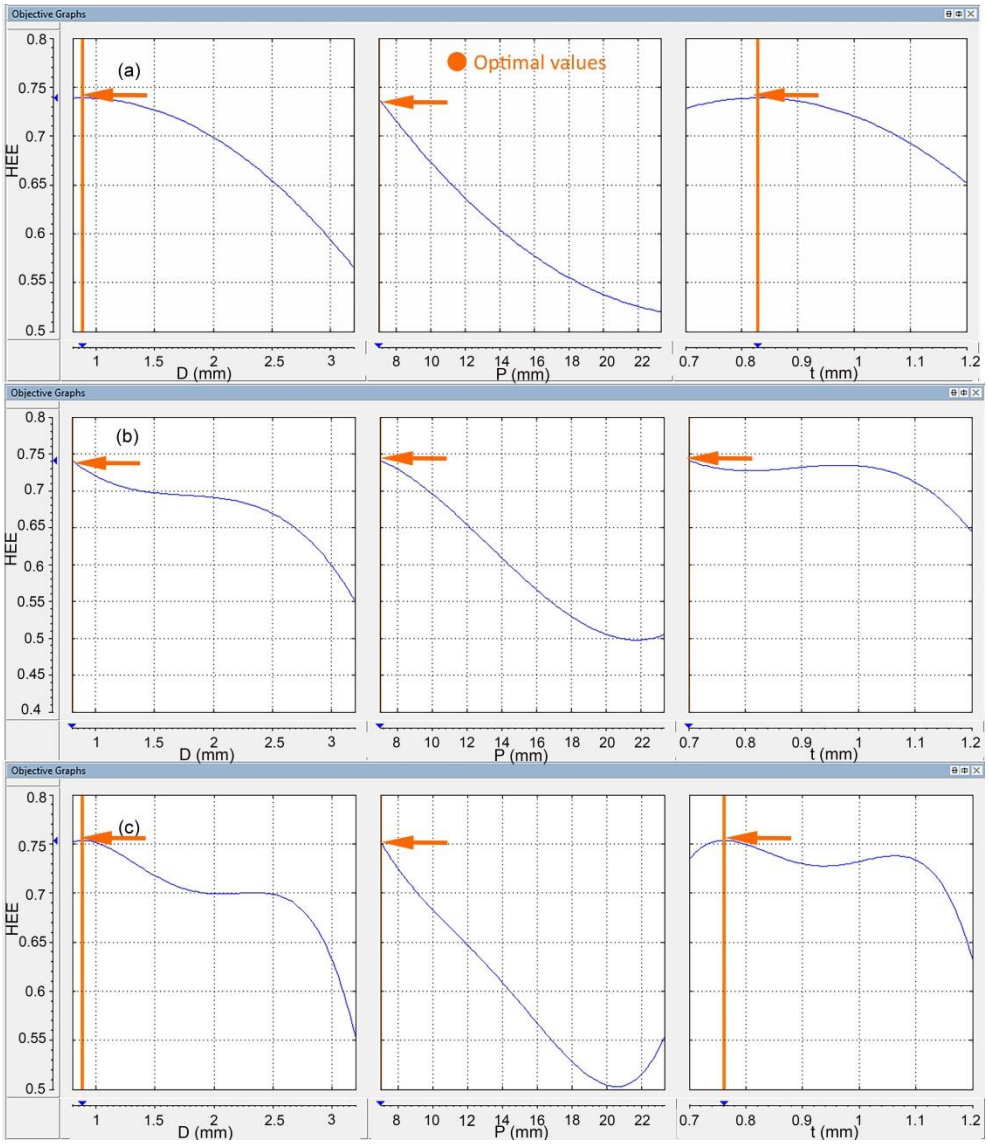

Figure 4-37. Distribution of optimised HEE versus individual design parameters for: (a) Quadratic model, (b) Cubic model, (c) Quartic model, for a sample population size of 36.

As shown in Figure 4-37, the results of the new optimisation exercise, based on a population of 36, showed some inconsistencies in terms of the HEE response with variations of pitch and thickness. Contrary to main-stream understanding (Shukla et al., 2012), the application of cubic and 4th order

regression models return curves of HEE vs pitch that reach a point of minimum for pitch distance of about 21 mm. No evidence was found to confirm whether these fluctuations were in fact realistic, due to over-fitting, or to the lack of knowledge (insufficient population density) around the turning points. Moreover, for all regression models, no consistent correlation could be identified between HEE and plate thickness.

As reported in Table 4-7 an extra set of six samples built around the turning points around P minima and D and t fluctuations was added to the general population, and the CFD simulations performed. The final database used for optimisation incorporated 42 geometrical configurations.

Table 4-7. Details of sample points for further study on the fluctuations.

Points	D (mm)	P (mm)	t (mm)
37	0.885	7	0.762
38	1.1	7	0.7
39	2.4	7	0.7
40	0.8	21.6	0.7
41	0.8	7	0.8
42	0.8	7	1.06

Figure 4-38 shows the optimal HEE response lines obtained, as explained above, by fixing two factor variables at their optimal level, and allowing the remaining ones to vary. In contrast to the previous optimisation, due to the increased sample population, all regression models show consistent results for optimal pitch size and optimal hole diameter. The absorber plate thickness, however, hasn't resolved into a single solution, with optimal level comprised between 0.76 and 0.93 mm depending on the regression model. The optimal solutions for the three regression models are summarised in Table 4-8.

Table 4-8. Optimal solution for geometrical factors returned by different regression models.

Regression Model	HEE	D (mm)	P (mm)	t (mm)
Quadratic	0.739	0.8	7.0	0.866
Cubic	0.741	0.8	7.0	0.927
Quartic	0.754	0.8	7.0	0.761

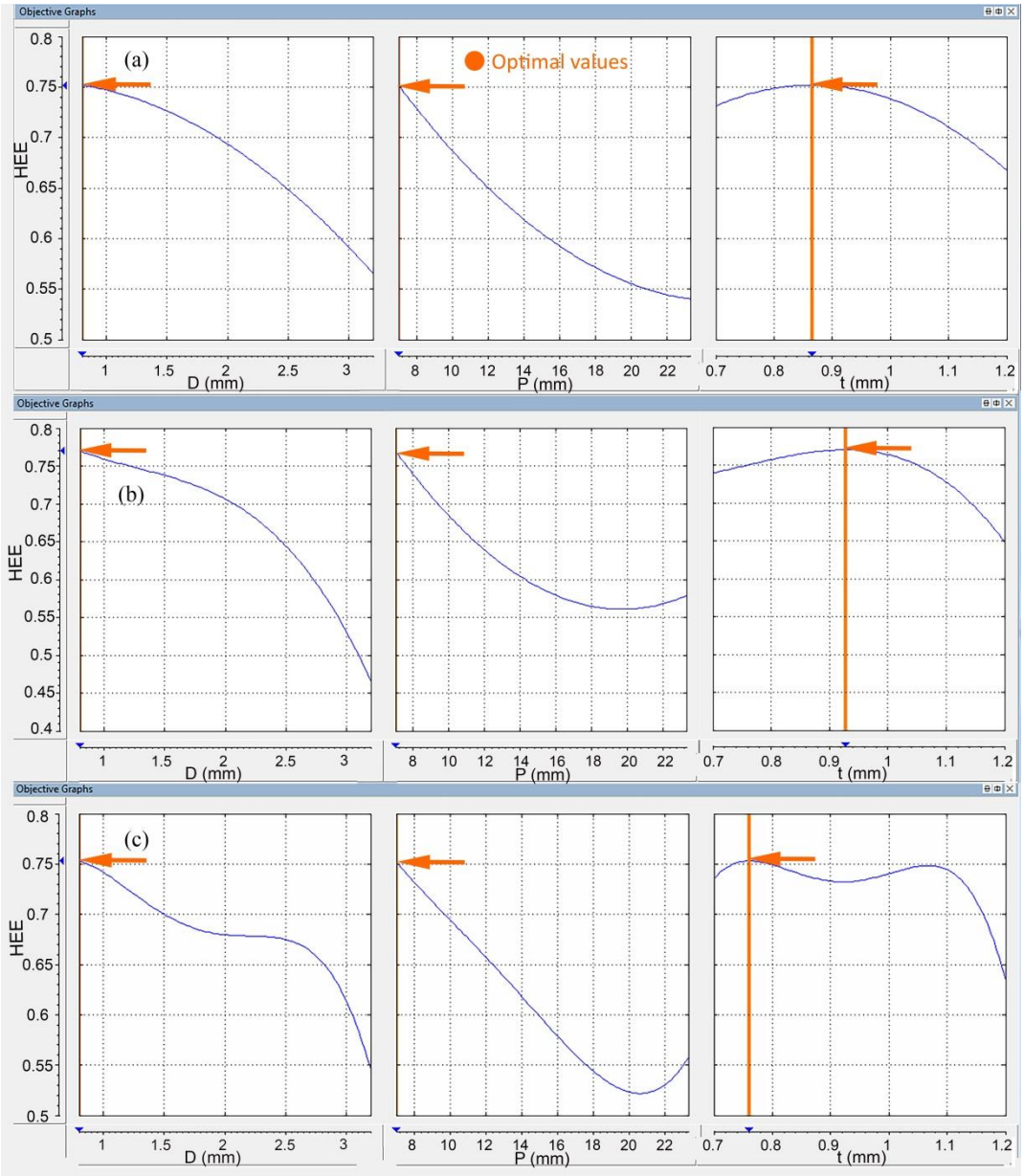

Figure 4-38. Distribution of optimised HEE versus individual design parameters: (a) Quadratic model, (b) Cubic model, (c) Quartic model, for a sample population size of 42.

As explained in Chapter 3, the quality of curve fitting for each regression model is measured through a range of statistical indicators. These factors, based on the 42 point strong population described above, assume the values reported in Table 4-9.

Table 4-9. Quality indicators of the regression models

Regression Model	RMSE	PRESS	R^2	R^2_{adj}
Quadratic	0.038	0.06	0.875	0.86
Cubic	0.032	0.0054	0.92	0.91
Quartic	0.029	0.0051	0.94	0.94

All regression models are deemed as acceptable, but higher order polynomials show inherently greater ability to follow the source data, returning more precise regression lines. Figure 4-39 shows predicted (regression) against observed (CFD simulated) values of HEE for the three different regression models.

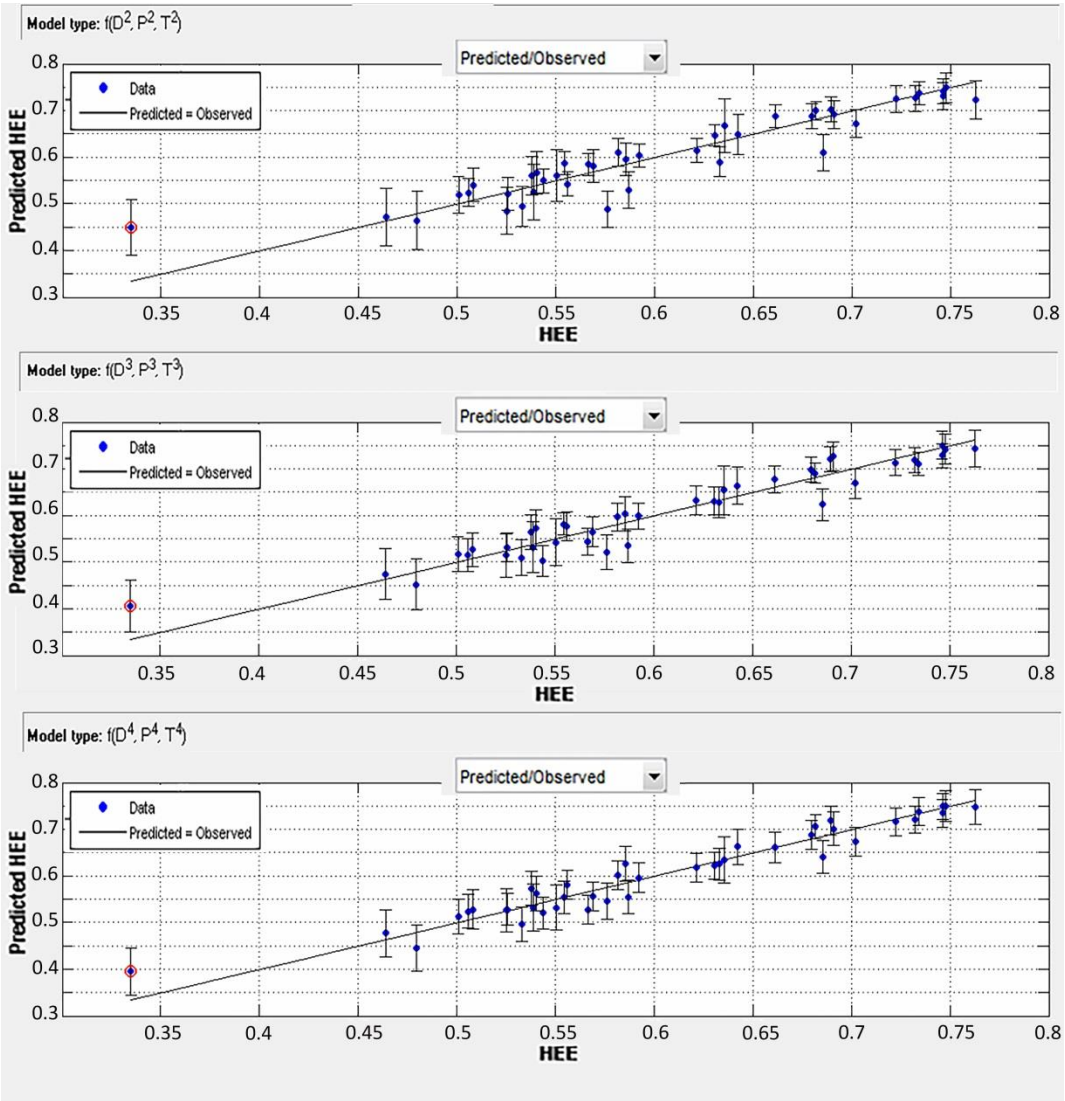

Figure 4-39. Plots of predicted (regression) against observed (CFD simulated) values for (a) Quadratic model, (b) Cubic model and, (c) Quartic model.

The analysis of the residuals is another classic measure of the predictive ability of a model; plots of residuals versus fitted values are presented in Figure 4-40. In all cases, the regression models are meaningful as the residuals do not show a correlation with the predicted response, with a structure-less distribution scattering in a horizontal band around zero (Onlinecourses.science.psu.edu, 2018). Both Figure 4-39 and Figure 4-40 show the presence of an outlier, which relates to the combination: D=3.2 mm, P=7 mm, t=1.2 mm, i.e. the plate with the highest porosity and thickness of all studied

plates. The available simulation results are insufficient to determine whether this is a true outlier caused by simulation error (as the CFD model was validated using a very different absorber plate geometry), or whether the resulting significant drop in HEE is a realistic response to an unlikely geometrical configuration. Since a healthy regression is not affected by an outlier, the outlier has been dismissed from the analysis; the resulting optimal solutions and HEE correlations were subject to negligible modification as a result of this dismissal.

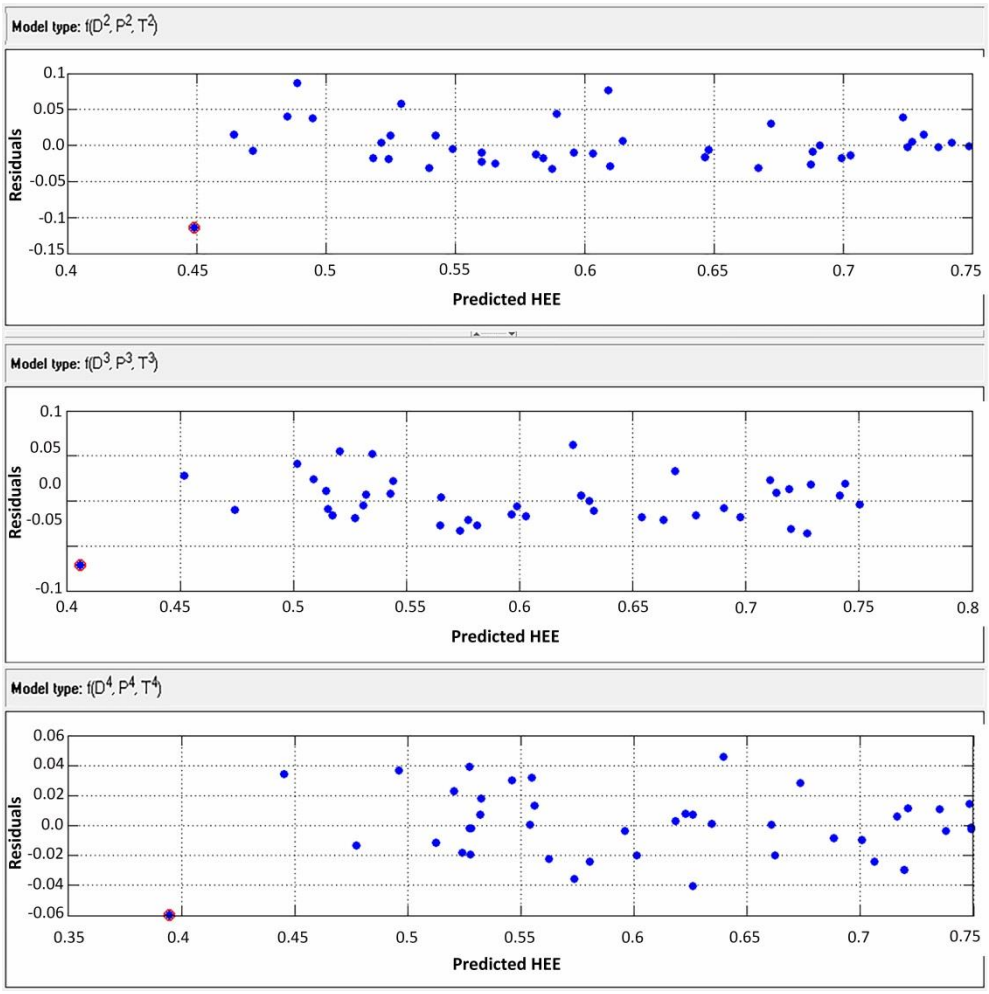

Figure 4-40. Plots of residuals versus predicted HEE for (a) Quadratic model, (b) Cubic model and, (c) Quartic model – 42 sample size population.

Referring back to the optimal HEE response lines presented in Figure 4-38, it is evident that increasing the sample population size to 42 points has not cured the presence of fluctuations and turning points mostly relating pitch distance and plate thickness which as expected remain most evident when using a higher order regression model. Montgomery (2012) generally recommends fitting the lowest order polynomial that sufficiently describes the system. High order polynomials often do not improve the data fitting but only enhance the complexity of the model. The HEE function obtained through quadratic regression is simpler and shows compliance with mainstream literature (Arulanandam et al., 2000; Van

Decker et al., 2001; Leon et al., 2007) except for the thickness variation. Whilst increasing pitch distance tend to decrease porosity and increase the heat absorbing surface area, it tends to create hot spots far from the perforations which increases the heat loss (Arulanandam, 2000). Moreover, by the very nature of TSCs, decreasing the porosity of the absorber plate can reduce the heat exchange to the system's outlet. The reason why thickness is not in agreement with mainstream literature is that both thick and thin absorber plates can cause interruption in heat exchange process. If the absorber is too thin then the heated air can be drawn out of the plenum. Thick plates can also cause a significant pressure drop which reduce the ability of the TSC to transfer heat from the front surface to the system's outlet. A simple regression between the plate thickness and the pressure drop across the system for the 42-point population explains why HEE experiences a peak as the thickness increasing. Figure 4-41 shows how pressure drop varies with plate thickness at the optimum diameter and pitch values ($D = 0.8$ mm, $P = 7$ mm). As discussed before (Section 4.4), pressure drop and effectiveness have an inverse relationship where the lowest value of pressure drop returns the highest HEE. However, this theory is negated where the pressure drop across the system is too low to deliver the heated air into the plenum outlet. In other words, each optimum HEE curve is associated with an optimum pressure drop curve. Optimum pressure curves can be investigated in the future study. The optimum pressure drop associated with the highest HEE under the current operating condition is about 16.5 (Pa).

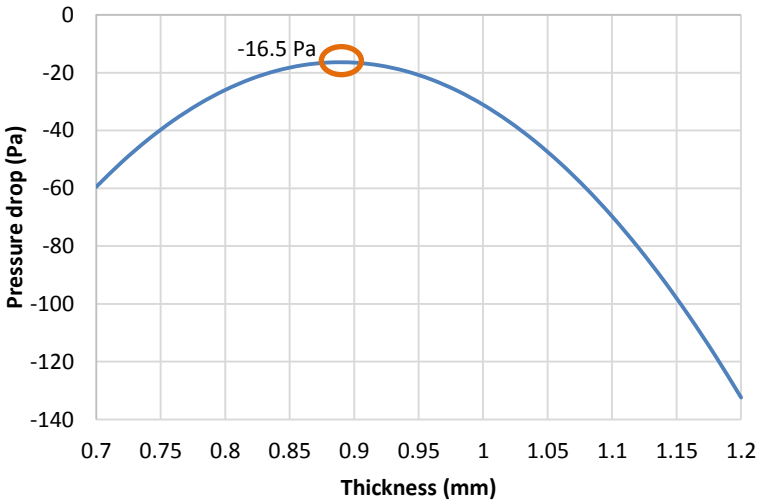

Figure 4-41. Variation of pressure drop versus plate thickness at D=0.8 mm and P= 7mm.

The quadratic model is then taken forward as the most illustrative, and the higher order models are dismissed due to potential over-fitting, which may lead to misrepresentation of the physical response of the system.

The quadratic regression fit for HEE as a function of the three factor variables is given by the following correlation:

$$\varepsilon = 0.45386 + 0.024778D - 0.04673P + 1.25253t - 0.02419D^2 + 0.004024DP - 0.03931Dt + 0.000644P^2 + 0.012705Pt - 0.75648t^2 \quad (4\text{-}2)$$

When evaluated within the following factor variables ranges:

0.8 mm $\leq D <$ 3.2 mm ,

7 mm $\leq P <$ 23.33 mm , and

0.7 mm $\leq D <$ 1.2 mm ,

the model shows a Root Mean Squared Error of 3.8%, which is lower than that calculated by Van Decker et al. (2001). However, the correlation has been generated for one single operating condition; its applicability to different climatic conditions is investigated in the next section. Development of a correlation incorporating different operating condition together with geometrical design will be the subject of future study.

The optimal absorber plate geometry design obtained through the application of the second order regression model, features hole diameter of 0.8 mm, pitch of 7 mm and plate thickness of 0.86 mm. At the operating conditions for which the correlation was developed, this geometry ensures a HEE of about 74%, which corresponds to an increase of about 43% compared to the original geometry. By referring back to Figure 4-18, it is evident that this variation of HEE, obtained solely by means of geometrical modification, compares well with the changes associated with realistic variation of wind speed, suction ratio, and solar radiation. Through optimised absorber plate geometry, the system can potentially counteract the adverse effects generated by uncontrollable variation of climatic conditions. From the results shown in Figure 4-22, it is calculated that the potential temperature rise associated to the optimised geometry is equivalent to increasing solar radiation intensity by about 122 w/m^2.

4.9.1 Validation

The geometry optimisation exercise presented in Section 4.9 was carried out using a single set of operating conditions. The present section investigates the applicability of the results to a wider range of

operating conditions, assessing the effects of potential inter-dependences between optimal geometrical design and environmental variables.

A range of simulations have been carried out based around the factors comprising wind speed, suction ratio and solar radiation which have demonstrated the most significant thermal performance in this study. The details of the new simulations are presented in Table 4-10. The operating conditions considered in Section 4.9 are addressed as the reference condition in the table. Two new cases were created per each relevant factor, with their range of variation chosen consistently with previously presented results. One extra simulation was also performed under reference operating conditions to validate the consistency between HEE calculated from the CFD model featuring optimal geometry, and HEE predicted using the statistical correlation.

Table 4-10. Details of the operating conditions applied to the optimised geometry

Case No.	Comment	Wind speed	Suction ratio	Solar radiation
1	Reference Condition	5	0.008	600
2	Solar radiation variation 01			450
3	Solar radiation variation 02			705
4	Suction ratio variation 01		0.006	600
5	Suction ratio variation 02		0.010	
6	Wind speed variation 01	3	0.008	
7	Wind speed variation 02	7		

All the results are summarised in Figure 4-42. The ‘Reference Condition’ simulation shows a level of HEE which is roughly 46% higher than that calculated upon the standard geometry. This is 3% greater than the level predicted using the statistical correlation; such magnitude of variation is acceptable. The results for different environmental variables indicate significant improvements in HEE levels calculated using the optimised geometry, with an average growth of about 44%. In other words, irrespective of the combination of external conditions, the optimised absorber plate geometry would enhance the ability of the system to deliver an outlet temperature as high as the absorber surface temperature, by about 44%. The results are also approximately consistent under the various operating conditions, with maximum and minimum HEE growth between 48% and 36%, respectively.

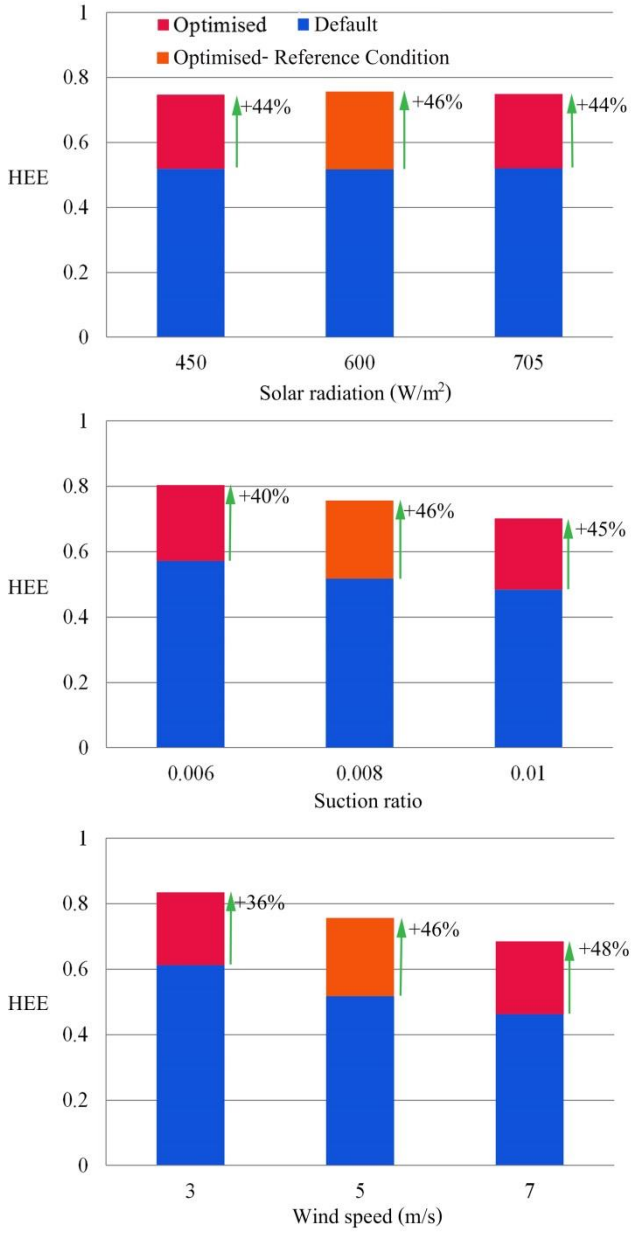

Figure 4-42. Effectiveness comparison of the optimised and conventional TSC geometry

Figure 4-43 shows a comparison has also been made between the temperature and pressure distribution of the airflow for the optimised and the default geometry (Figure. 4-2). Since the system is relatively long, it has been presented in two splits as top and bottom configuration for better clarity. The optimised geometry delivers a higher level of air temperature which supports the higher thermal performance that is predicted by the optimisation study. A significant lower pressure distribution generated in the plenum of the optimised TSC compared to the default one explains the higher level of air temperature and HEE .

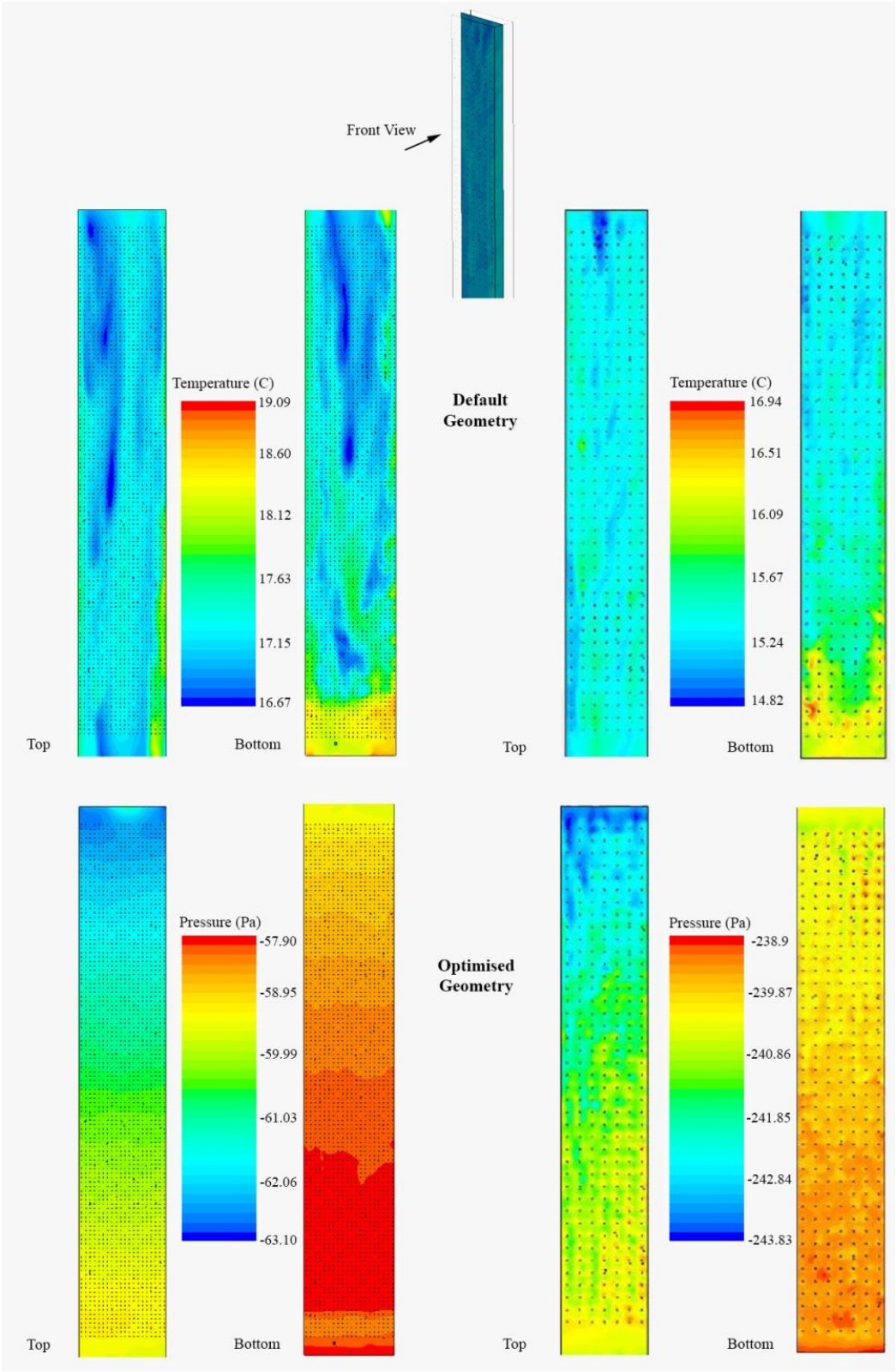

Figure 4-43.Front view of air temperature and pressure distribution taken place within the plenum

Chapter 5 Conclusion and recommendations for further research

5.1 Conclusions

TSCs have significant and quantifiable potential to reduce the present reliance on fossil fuels for heating buildings, and therefore to play an important role in meeting the UK and international carbon reduction targets. The relative technical simplicity of systems is highly desirable as many other zero and low emission technologies have the capital and in-service costs that are prohibitive to their wider use. The present research has attempted to develop a CFD model and optimisation analysis that provide the most accurate performance representation of TSCs hitherto available which is able to account for the key variables including airflow (notably wind speed and wind angle), solar radiation intensity (based sun position), turbulent flow across the system, non-uniform flow suction through perforated plates, the thermophysical and geometrical properties of the absorber plate. Experimental data from tests conducted at Oxford Brookes University have been used to validate the accuracy of the CFD model. The model provides a basis for optimising the performance of TSCs, developing commercial products, and designing systems based on commercial products in relation to local conditions. The key findings of the performed parametric studies and optimisation analysis are:

- Wind speed, suction ratio, and solar radiation have respectively shown the most significant impact on the temperatures rise amongst the studied variables. On average, increasing wind speed, suction ratio, and solar radiation can affect temperature rise by about 81.6%, 47%, and 44%, respectively. Wind direction, thermal conductivity, and sun position have shown less significant but worth considering the effect on temperature rise. Plenum depth, however, has shown the least significant effect on the temperature rise.

- HEE decreases with the increasing wind speed and suction ratio on average by about 47% and 21% respectively. Solar radiation, wind direction, plenum depth, and thermal conductivity, however, have shown a negligible impact on HEE. Detailed investigation of the three main regions of heat transfer has quantified the average contribution of each

region to the overall HEE to be: 62.3% for front surface, 21.9% for perforations and 15.8% for the back surface of the plate.

- Increasing wind speed, suction ratio, and thermal conductivity have been predicted to raise the thermal efficiency by about 84%, 65%, and 21%, respectively. Increasing wind angle has also lead to a reduction in thermal efficiency by about 7.5%. Plenum depth, however, has shown a negligible effect on the thermal efficiency of the system.

- The sun position has been investigated at five different times of the day. The model has predicted that both temperature rise and surface temperature increase from the morning until early afternoon when they reach peak value and then start decreasing during the afternoon as the sun descending. The results show that the system can deliver air with a temperature of 8.8°C higher than the ambient on a clear day in winter. Considering the solar radiation intensity is kept constant in this parametric study, the temperature variation is only due to the sun orientation.

- Optimisation study has been carried out using the Design of Experiments (DoE) technique which defines the appropriate set of variables to be experimented based on the validate CFD model. Simulations have been performed incorporating a different combination of variable factors (diameter, pitch and plate thickness), referred to as points, and the responses (the resulting HEE) have been fed into the optimiser. The optimal point for this particular TSC design has been reached through a multi-stage analysis.

- The optimised geometry is predicted to increase HEE by about 43%. This level of increase is highly comparable with the variation of wind speed, suction ratio, and solar radiation. From the parametric study it is deduced that the effectiveness decreases on average by 10% per 1m/s of wind speed and 6.5% per 0.002 suction ratio, respectively. In other words, just by optimising the geometry, the system can potentially benefit from resisting against such phenomena. The temperature rise that the system could provide with the optimised geometry is equivalent to increasing solar radiation intensity by about 122 W/m^2.

- As a consequence of the optimisation study, the system is able to perform 43% better using 28% less material used in volume which is a significant impact for the TSC manufacturers and users, in particular in countries with less available solar radiation such as the UK. Such optimisation analysis can be morphed to other applications with careful consideration of corresponding limitations.

- Based on the DoE, a quadratic correlation with high levels of accuracy, predictability, and simplicity has been generated for HEE. The correlation as a function of diameter, pitch and thickness is defined as:

$$\varepsilon = 0.45386 + 0.024778D - 0.04673P + 1.25253t - 0.02419D^2 + 0.004024DP - 0.03931Dt + 0.000644P^2 + 0.012705Pt - 0.75648t^2 \quad (5\text{-}1)$$

- This correlation (Eq. 5-1) fits all of the data within the range of $0.8 \leq D \leq 3.2$, $7 \leq P \leq 23.33$, and $0.7 \leq t \leq 1.2$ with a root mean squared error of 3.8%. The optimal case which could potentially deliver the highest effectiveness has been predicted to be: $\mathrm{HEE} = 0.739$ at the point with $\mathrm{D} = 0.8$ mm, $\mathrm{P} = 7$ mm, $\mathrm{t} = 0.866$ mm.

- Whilst the HEE correlation has been generated for one single operating condition its applicability to variant climatic conditions has been verified against different solar radiation, suction ratio, and wind speed levels. Irrespective of the combination of different conditions, the optimised absorber plate geometry has been able to show an average enhancement of about 43% across the tested conditions. The impact of porosity together with the thickness of the absorber plate on the airflow pressure distribution and subsequently the thermal performance of TSCs has been illustrated in this work.

5.2 Recommendations for Future Study

This study has shed light on new aspects of factors that could be potentially part of this research and provide opportunities for further research on how these factors can develop our knowledge about TSCs. A series of recommendations for further research are proposed, as derived from the outcome of the present study.

5.2.1 Edge effect evaluation together with 3-D wind flow

The study has been carried out for a section of the absorber plate whilst imposing a 2-D wind flow. Having applied a 3-D wind flow together with locating the absorber section at the side of the full-size TSC system can be studied further to improve the understanding of the local edge effect towards the thermal performance of the TSCs.

5.2.2 Optimisation incorporated with climatic and thermal variables

The optimisation study has been undertaken at a fixed climatic and operating condition for a single material. A more comprehensive optimisation analysis including different operating and climatic conditions together with materials with the various associated thermal features could deliver a more practical and holistic optimised TSC system considering all the important limitations and design inputs.

5.2.3 Heat transfer enhancement based on the main heat exchanging zones

The zones at which the absorber exchanges heat with air are namely the front surface, perforations and back surface of the absorber plate. They all have been recognised to contribute considerably to the overall heat output. The sensitivity of each zone to the effective variables can be different which introduces an opportunity to maintain or increase thermal performance under various conditions. Wind speed, for instance, has been shown to have a negligible impact on the front surface whereas the impact is considerable on the other two zones. Further research may be suitable to account for the individual role of these regions in order to increase HEE in TSCs for different scenarios.

5.2.4 Contribution of each material to the final heat transfer

Having studied a number of materials with different thermal conductivities, the results indicate that thermal conductivity is not the only factor influencing the efficient heat exchange but also the amount of the conducted heat actually captured by the system. Hence, if the system is not able to capture the exchanged heat with the air, heat loss increases. If the heat capacity of the material is high, it means that the absorber doesn’t give the heat away as fast as a low heat capacity material. This is where depending on what the balance between the conducted and stored heat would be, different scenarios can take place. Hence further research can specify the contribution of each material to the final heat transferred to the outlet.

5.2.5 An unsteady state study of temperature built up

Whilst the solar angularity is shown to affect the thermal performance and increase the outlet temperature, the model has not accounted for the temperature built up in the system in a transient way. There seems to be a potential for a time-dependent study of the system to demonstrate the build-up temperature during a day.

5.2.6 Enhanced TSCs

It has been the primary aim of this research to discover key design variables which can be improved to enhance TSCs performance. Enhancement may include modification, optimisation or coupling the system with other technologies. Further research based on what is available in the state-of-the-art TSCs together with the outlined conclusions of this research could be conducted to enhance the performance of the system.

A project called Enhanced TSC has been started on this basis incorporating TSCs and optical science technology. The aim of the project is to produce a prototype to Enhance TSC which is able to generate high-grade heat. Generation of heat with high-level temperature magnitudes facilitates TSCs to be coupled with thermal storage systems storing the available heat during sunny days to be consumed at nights or cold occasions. It is predicted that the system can provide 50% of the residential buildings' space heating demand annually.

References

Abulkhair, H., Collins, M., (2010). Investigation of wind heat loss from unglazed transpired solar collectors with corrugation. In: 5th Annual International Green Energy Conference, Waterloo, Ontario, June 1–3.

Arulanandam, S.J., Hollands, K.G.T., Brundrett, E., (2000). A CFD heat transfer analysis of the transpired solar collector under no-wind conditions. Solar Energy, 67 (1), 93–100.

ASHRAE 45.3 (2015), ASHRAE Handbook, American Society of Heating, Refrigerating, and Air-Conditioning Engineers. HVAC Applications, Atlanta, GA,.

Athienitis, A.K., Bambara, J., O'Neill, B., Faille, J., (2011). A prototype photovoltaic/thermal system integrated with transpired collector. Solar Energy, 85, pp.139–153.

Badache, M., Rousse, D., Halle´, S., Quesada, G. (2013). Experimental and numerical simulation of a two-dimensional unglazed transpired solar air collector. Solar Energy, 93, pp. 209-219.

BEIS (2017). 2015 UK greenhouse gas emissions, final figures. London : Crown copyright.

Biona, M., Culaba, A., Serafica, E., Mundo DR., (2005). Performance curve generation of an unglazed transpired collector for solar drying applications. In: Proceedings of World Renewable Energy Regional Conference.

Brown, C., Persioglou, E., Hall, R., Stevenson, V. (2014). In: SHC 2013, International Conference on Solar Heating and Cooling for Buildings and Industry, Freiburg, Germany September 23-25, pp. 18-27.

Burnett, D., Barbour, E., Harrison, G.P. (2014). The UK solar energy resource and the impact of climate change. Renewable Energy, 71, pp. 333-343.

Cao, S., Hollands, K., Brundrett, E. (1993). Heat exchange effectiveness of unglazed transpired-plate solar collector in 2D flow. In: Proceedings of ISES Solar World Congress 1993, Budapest, Hungary, 5, pp. 351–366.

Chan, H.Y., Zhu, J. and Riffat, S. (2013). Heat transfer analysis of the transpired solar facade. *Energy Procedia*, *42*, pp.123-132.

Climate Change: Vital Signs of the Planet. (2018). Scientific consensus: Earth's climate is warming. [online] Available at: https://climate.nasa.gov/scientific-consensus.

Collins, M., Abulkhair, H., (2014). An evaluation of heat transfer and effectiveness for unglazed transpired solar air heaters. Solar Energy, 99, pp. 231-245.

Commission of the European Communities, (2014). A policy framework for climate and energy in the period from 2020 to 2030, COM (2014) 15 final. Brussels.

Committee on Climate Change, (2014). Meeting Carbon Budgets – 2014 Progress Report to Parliament. https://www.theccc.org.uk/wp-content/uploads/2014/07/CCC-Progress-Report-2014_web_2.pdf.

Cordeau, S., Barrington, S. (2011). Performance of unglazed solar ventilation air pre-heaters for broiler barns. Solar Energy, 85, pp. 1418-1429.

Davis, P & Rinehimer, Aron & Uddin, Mesbah. (2012). A Comparison of RANS-Based Turbulence Modeling for Flow over a Wall-Mounted Square Cylinder.

DECC (2016), UK Energy Statistics, Q1 2016. London : Crown copyright

Dutton, R.A., (1958). The effects of distributed suction on the development of turbulent boundary layers. Aeronautical Research Council Technical Report, R&M No. 3155, London, England.

Dymond, C., Kutscher, C. (1997). Development of a flow distribution and design model for transpired solar collectors. Solar Energy, 60(5), pp. 291-300.

Fan, J., Shah, L. and Furbo, S. (2007). Flow distribution in a solar collector panel with horizontally inclined absorber strips. Solar Energy, 81(12), pp. 1501-1511.

Fleck, B., Meier, R., Matovic, M. (2002). A field study of the wind effects on the performance of an unglazed transpired solar collector. Solar Energy, 2002, 73(3), pp. 209–16.

Garud, S., Karimi, I. and Kraft, M. (2017). Design of computer experiments: A review. Computers & Chemical Engineering, 106, pp.71-95.

Gawlik, K.M., Christensen C, Kutscher C. (2002). Wind Heat Loss From Corrugated, Transpired Solar Collectors. Journal of Solar Energy Engineering, 124 (3), pp.256-261.

Gawlik, K.M., Christensen C, Kutscher C. (2005). A Numerical and Experimental Investigation of Low-conductivity Unglazed, Transpired Solar Air Heaters. Journal of Solar Energy Engineering, 127 (1), pp.153-155.

Golneshan, A., (1994). Forced convection heat transfer from low porosity slotted transpired plates. Ph. D. Thesis, Department of Mechanical Engineering, University of Waterloo.

Golneshan, A., Hollands, K. (2000) Forced convection experimentson slotted transpired plates.Transactions of the Candaian Society for Mechanical engineering, 24, pp. 335-347.

Gunnewiek, L., Brundrett, E., Hollands, K., (1996). Flow distribution in unglazed transpired plate solar air heaters of large area. Solar Energy, 58, pp.227-237.

Gunnewiek, L., Hollands, K., Brundrett E., (2002). Effect of wind on flow distribution in unglazed transpired plate collectors. Solar Energy, 72, pp.317-325.

Hall, R., Kendrick, C. and Lawson, R. (2014). Development of a cassette-panel transpired solar collector. Proceedings of the Institution of Civil Engineers - Energy, 167(1), pp.32-41.

Hall, R. and Blower, J. (2016). Low-emissivity Transpired solar collectors. Energy Procedia, 91, pp. 56-63.

Hollick. J.C., (1994). Unglazed solar wall air heaters. Renewable Energy, 5(1-4), pp145-421.

Incropera, F., DeWitt, D., Bergman, and T., Lavine, A. (2011). Fundamentals of Heat and Mass Transfer. New York: Wiley.

Kutscher, C.F., 1992. An investigation of heat transfer for air flow through low porosity perforated plates. Ph.D. Thesis, Department of Mechanical Engineering, University of Colorado at Boulder, Colorado, USA.

Li, S., Karava, P., Currie, S., Lin, W., Savory, E. (2014). Energy modeling of photovoltaic thermal systems with corrugated unglazed transpired solar collectors – Part 1: Model development and validation. Solar Energy 102, pp. 282-296.

Mavriplis, D. (1996). ‘Mesh generation and adaptivity for complex geometries and flows’, in Peyret, R. (ed.) Handbook of Computational Fluid Mechanics. San Diego, California: Academic Press.

MHCLG (2014), Approved Document L1A: conservation of fuel and power in new dwellings, 2013 edition with 2016 amendments. Crown copyright.

MHCLG (2014), Approved Document L2A: conservation of fuel and power in new buildings other than dwellings, 2013 edition with 2016 amendments. Crown copyright.

Montgomery, D. C. (2012). Design and analysis of experiments. New York: Wiley.

Mu, D., Gao, N., & Zhu, T. (2016). Wind tunnel tests of inter-flat pollutant transmission characteristics in a rectangular multi-storey residential building, part A: effect of wind direction. Building and Environment, 108, pp. 159-170.

Najafi Khaboshan, H. and Nazif, H. (2018). The effect of multi-longitudinal vortex generation on turbulent convective heat transfer within alternating elliptical axis tubes with various alternative angles. Case Studies in Thermal Engineering, 12, pp.237-247.

Onlinecourses.science.psu.edu. (2018). 4.3 - Residuals vs. Predictor Plot | STAT 501. [online] Available at: https://onlinecourses.science.psu.edu/stat501/node/278/.

Pointwise.com. (2018). Quality and Control - Two Reasons Why Structured Grids Aren't Going Away | The Connector. [online] Available at: http://www.pointwise.com/theconnector/2013-March/Quality-Control-Two-Reasons-Structured-Grids-Arent-Going-Away.html.

Santner, T., Williams, B. and Notz, W. (2003). The Design and Analysis of Computer Experiments. New York, NY: Springer New York.

Schlichting, H. (1979) Boundary-layer theory. New York: McGraw-Hill.

Shih, T., Liou, W., Shabbir, A., Yang, Z., Zhu, J. (1995). A new k-ϵ eddy viscosity model for high reynolds number turbulent flows. Comouters & Fluids, 24 (3), pp.227-238.

Shukla, A., Nkwetta, D., Cho, Y., Stevenson, V., Jones, P. (2012). A state of art review on the performance of transpired solar collector. Renewable and Sustainable Energy Reviews, 16, pp. 3975-3985.

Sieder, E., Tate, E. (1936). Heat Transfer and Pressure Drop of Liquids in Tubes. Industrial & Engineering Chemistry Research, 28, pp. 1429-1435.

Sparrow, E., Ortiz, M. (1982). Heat transfer coefficients for the upstream face of a perforated plate positioned normal to an oncoming flow. Journal of Heat and Mass Transfer, 25 (1), pp. 127-135.

STAR-CCM+® CD-adapco, (2014). STAR-CCM+ 9.04.009 USER GUIDE.

Tajdaran, S., Bonatesta, F., Ogden, R. and Kendrick, C. (2016). CFD modelling of transpired solar collectors and characterisation of multi-scale airflow and heat transfer mechanisms. Solar Energy, 131, pp.149-164.

The Stationary Office (2008). Climate Change Act 2008. London: Crown Copyright.

Van Decker, G.W.E., Hollands, K.G.T., Brunger, A.P., (2001). Heat-exchange relations for unglazed transpired solar collectors with circular holes on a square or triangular pitch. Solar Energy 71, pp.33–45.

Verrolet, E., et al. (1972). Turbulent Boundary Layer with Suction and Heating to the wall. Heat and mass transfer in boundary layer, 1, Pergamon Press, Oxford and New York, 1972, pp. 157-168.

Versteeg, Henk & Malalasekera, W. (2018). An introduction to computational fluid dynamics : the finite volume method / H.

Wang, Y., Shukla, A., Liu, S. (2017). A state of art review on methodologies for heat transfer and energy flow characteristics of the active building envelopes. Renewable and Sustainable Energy Reviews, 78, pp. 1102-1116.

Warming, R. F., Beam, Richard M. (1976). Upwind Second-Order Difference Schemes and Applications in Aerodynamic Flows. AIAA Journal, 14 (9), pp.1241-1249.

R. F. Warming and Richard M. Beam. (1976). Upwind Second-Order Difference Schemes and Applications in Aerodynamic Flows. AIAA Journal, 14 (9), pp.1241-1249.

World Energy Council. (2013). World Energy Resourses, 2013 Survey: Solar. [online] Available at: https://www.worldenergy.org/publications/2013/world-energy-resources-2013-survey/.